


November 2017

COMPUTATIONAL STUDIES OF STRUCTURE–FUNCTION RELATIONSHIPS OF SUPPORTED AND UNSUPPORTED METAL NANOCLUSTERS

Hongbo Shi
university of massachusetts amherst

Follow this and additional works at: https://scholarworks.umass.edu/dissertations_2

 Part of the [Catalysis and Reaction Engineering Commons](#), [Materials Chemistry Commons](#), [Other Engineering Science and Materials Commons](#), [Other Materials Science and Engineering Commons](#), and the [Structural Materials Commons](#)

Recommended Citation

Shi, Hongbo, "COMPUTATIONAL STUDIES OF STRUCTURE–FUNCTION RELATIONSHIPS OF SUPPORTED AND UNSUPPORTED METAL NANOCLUSTERS" (2017). *Doctoral Dissertations*. 1123.
https://scholarworks.umass.edu/dissertations_2/1123

This Open Access Dissertation is brought to you for free and open access by the Dissertations and Theses at ScholarWorks@UMass Amherst. It has been accepted for inclusion in Doctoral Dissertations by an authorized administrator of ScholarWorks@UMass Amherst. For more information, please contact scholarworks@library.umass.edu.

**COMPUTATIONAL STUDIES OF STRUCTURE–FUNCTION
RELATIONSHIPS OF SUPPORTED AND UNSUPPORTED METAL
NANOCCLUSERS**

A Dissertation Presented

by

Hongbo Shi

Submitted to the Graduate School of the
University of Massachusetts Amherst in partial fulfillment
of the requirements for the degree of

DOCTOR OF PHILOSOPHY

September 2017

Chemical Engineering

© Copyright by Hongbo Shi

All Rights Reserved

**COMPUTATIONAL STUDIES OF STRUCTURE–FUNCTION
RELATIONSHIPS OF SUPPORTED AND UNSUPPORTED METAL
NANOCLUSTERS**

A Dissertation Presented

by

Hongbo Shi

Approved as to style and content by:

Ashwin Ramasubramaniam, Co-Chair

Scott M. Auerbach, Co-Chair

Friederike Jentoft, Member

Bret Jackson, Member

John Klier, Department Head
Chemical Engineering

DEDICATION

To my beloved family

ACKNOWLEDGMENTS

First of all, I would like to thank my supervisors Professor Ashwin Ramasubramaniam and Professor Scott M. Auerbach for their insightful guidance and support throughout my graduate program. I especially thank them for the many opportunities they provided for training and developing my skill sets as a computational scientist. I am also deeply grateful to my committee members Professor Bret Jackson and Professor Friederike Jentoft for their useful comments and for serving on my committee.

It would have been impossible for me to finish this thesis work without the fruitful discussions I have had with my present and past lab mates, including Dr. Ioanna Famipou, Dr. Lin Jin, Dr. Vishal Agarwal, Dr. Jacob Harvey, Dr. Angela Miguez, Dr. Szu-Chia Chien, Dr. Mohammad Navaid Khan, Raymond Gasper and Qinfang Sun.

I would also like to thank my wife and family for their support over the entire course of my graduate studies.

This work was supported by U.S Department of Energy under Award Number (DE-SC0010610). Computational resources were provided by National Energy Research Scientific Computing Center (NERSC) and Massachusetts Green High Performance Computing Center (MGHPCC).

ABSTRACT
COMPUTATIONAL STUDIES OF STRUCTURE–FUNCTION
RELATIONSHIPS OF SUPPORTED AND UNSUPPORTED METAL
NANOCCLUSERS

September 2017

Hongbo Shi, B.S., BEIJING INSTITUTE OF TECHNOLOGY

M.S., TSINGHUA UNIVERSITY

Ph.D., UNIVERSITY OF MASSACHUSETTS AMHERST

Directed by: Professor Ashwin Ramasubramaniam and Professor Scott M. Auerbach

Fuel cells have been demonstrated to be promising power generation devices to address the current global energy and environmental challenges. One of the many barriers to commercialization is the cost of precious catalysts needed to achieve sufficient power output. Platinum-based materials play an important role as electrocatalysts in energy conversion technologies. In order to improve catalytic efficiency and facilitate rational design and development of new catalysts, structure–function relationships that underpin catalytic activity must be understood at a fundamental level.

First, we present a systematic analysis of CO adsorption on Pt nanoclusters in the 0.2–1.5 nm size range with the aim of unraveling size-dependent trends and developing predictive models for site-specific adsorption behavior. Using an empirical-potential-based Genetic Algorithm (GA) and DFT modeling, we show that there exists a size window (40–70 atoms) over which Pt nanoclusters bind CO weakly, the binding energies being comparable to those on (111) or (100) facets. The size-dependent adsorption energy trends are, however, distinctly non-monotonic and are not readily captured using traditional descriptors such as *d*-band energies or (generalized) coordination numbers of the Pt binding

sites. Instead, by applying machine-learning algorithms, we show that multiple descriptors, broadly categorized as structural and electronic descriptors, are essential for qualitatively capturing the CO adsorption trends. Nevertheless, attaining quantitative accuracy requires further refinement and we propose the use of an additional descriptor – the fully-frozen adsorption energy – that is a computationally inexpensive probe of CO–Pt bond formation. With these three categories of descriptors, we achieve an absolute mean error in CO adsorption energy prediction of 0.12 eV, which is similar to the underlying error of DFT adsorption calculations. Our approach allows for building quantitatively predictive models of site-specific adsorbate binding on realistic, low-symmetry nanostructures, which is an important step in modeling reaction networks as well as for rational catalyst design in general.

Thereafter, to understand support effects on the activity of Pt nanoclusters, we employ a combination of empirical potential simulations and DFT calculations to investigate structure–function relationships of small Pt_N ($N = 2\text{-}80$) clusters on model carbon (graphene) supports. A bond-order empirical potential is employed within a GA to go beyond local optimizations in obtaining minimum-energy structures of Pt_N clusters on pristine as well as defective graphene supports. Point defects in graphene strongly anchor Pt clusters and also appreciably affect the morphologies of small clusters, which are characterized via various structural metrics such as the radius of gyration, average bond length, and average coordination number. A key finding from the structural analysis is that the fraction of potentially active surface sites in supported clusters is maximized for stable Pt clusters in the size range of 20-30 atoms, which provides a useful design criterion for optimal utilization of the precious metal. Through selected *ab initio* studies, we find a

consistent trend for charge transfer from small Pt clusters to defective graphene supports resulting in the lowering of the cluster d-band center, which has implications for the overall activity and poisoning of the catalyst. The combination of a robust empirical potential-based GA for structural optimization with ab initio calculations opens up avenues for systematic studies of supported catalyst clusters at much larger system sizes than are accessible to purely ab initio approaches.

Finally, we present a self-consistent charge density-functional tight-binding (SCC-DFTB) parameterization for PtRu alloys, which is developed by employing a training set of alloy cluster energies and forces obtained from Kohn-Sham DFT calculations. Extensive simulations of a testing set of PtRu alloy nanoclusters show that this SCC-DFTB scheme is capable of capturing cluster formation energies with high accuracy relative to DFT calculations. The new SCC-DFTB parameterization is employed within a GA to search for global minima of PtRu clusters in the range of 13-81 atoms and the emergence of Ru-core/Pt-shell structures at intermediate alloy compositions is systematically demonstrated. Our new SCC-DFTB parameterization enables computationally inexpensive modeling and exploration of structure–function relationships for Pt-Ru clusters that are among the best-performing catalysts in numerous energy applications.

TABLE OF CONTENTS

	Page
ACKNOWLEDGMENTS	v
ABSTRACT.....	vi
TABLE OF CONTENTS.....	ix
LIST OF TABLES	xi
LIST OF FIGURES	xii
CHAPTER	
1. INTRODUCTION	1
1.1 What Are Fuel Cells?.....	1
1.2 Challenges.....	2
1.3 Catalyst Development.....	4
1.3.1 Size and Shape Effect	4
1.3.2 Support Effect.....	6
1.3.3 Pt-based Alloys as Catalysts	7
1.4 Thesis Objectives	8
2. STABILITY, ENERGTICS, AND CATALYTIC PROPERTIES OF UNSUPPORTED PT NANOCLUSTERS.....	12
2.1 Introduction.....	12
2.2 Methodology	14
2.2.1 GA for Optimization of Unsupported and Supported Clusters.....	14
2.2.2 Empirical Potential Models for Pt-Pt Interaction.....	17
2.2.3 DFT Calculations.....	18
2.2.4 Simulation Procedure.....	18
2.3 Result and Discussion.....	19
2.3.1 Structure and Energetics of Unsupported Pt Clusters.....	19
2.3.2 Electronic Structure of Unsupported Pt Clusters	23
2.3.3 Cluster-Size-Dependent CO Adsorption Energies and Their Correlation with d-band Center Energies	28
2.3.4 Prediction of CO Adsorption Energies via Machine Learning	29
2.4 Conclusions.....	36

3. STABILITY, ENERGETICS, AND CATALYTIC PROPERTIES OF GRAPHENE-SUPPORTED PT CLUSTERS	38
3.1 Introduction.....	38
3.2 Computational Methods.....	40
3.2.1 GA for Supported Clusters	40
3.2.2 Empirical Potential Models for Graphene Supported Pt clusters	41
3.2.3 Global Optimization for Supported Clusters	41
3.2.4 DFT Calculations.....	42
3.3 Result and Discussion.....	43
3.3.1 Structure and Energetics of Supported Pt Clusters	43
3.3.2 Support Effect on Electronic Structure of Pt ₁₃ isomers	51
3.3.3 Charge Transfer Between Pt clusters and Graphene Support.....	57
3.4 Conclusions.....	58
4. STABILITY AND ENERGETICS OF PtRu ALLOY CLUSTERS	60
4.1 Introduction.....	60
4.2 Computational Methods.....	61
4.2.1 SCC-DFTB Method.....	61
4.2.2 Calculation Procedures	62
4.3 Parameterization and Testing of SCC-DFTB Potentials.....	63
4.4 DFTB-Based GA Optimization of PtRu Clusters	70
4.5 Conclusions.....	73
5. CONCLUSIONS AND FUTURE WORK	75
5.1 Conclusions.....	75
5.2 Future Directions	77
APPENDICES	80
A. FIRST-PRINCIPLES PREDICATIONS OF STRUCTURE FUNCTION RELATIONSHIPS OF GRAPHENE-SUPPORTED PLATINUM NANOCCLUSERS	80
B. MD AND CLASSICAL SIMULATIONS OF THE TEMPERATURE DEPENDENCE OF ZEOLITE PORE SIZES	91
BIBLIOGRAPHY	102

LIST OF TABLES

Table	Page
Table 2.1. Total energy (eV) of Pt ₇ clusters.....	19
Table 2.2. Relative total energies (in eV) of Pt ₇ isomers from Kumar et al.'s ¹³⁷ and our DFT calculations (PBE functional; PW91 results in parentheses), as well as Albe et al.'s empirical potential (EP). Energies are relative to the lowest energy isomer for each level of theory.	20
Table 2.3. Relative total energies (in eV) of high-symmetry (cuboctahedral – Oh; icosahedral – Ih) Pt clusters and GA-optimized, low-energy clusters calculated using DFT and Albe et al.'s empirical potential (EP). Energies are relative to the lowest energy isomer for each size and level of theory.....	22
Table 2.4. Average <i>d</i> -band center energy of surface atoms, ε_d^{sur} and standard deviations, σ , as a function of cluster size, <i>N</i>	27
Table 3.1. Formation energies (eV) of minimum-energy Pt clusters on pristine and defective (vacancy, divacancy) graphene supports identified using the GA and by molecular-dynamics-based annealing (Ref. ⁶⁰).....	44
Table 3.2. Formation energies (eV) of minimum-energy Pt clusters on pristine and defective (vacancy, divacancy) graphene supports identified using GA.....	44
Table 3.3. Covalent NBOs for Pt ₁₃ on vacancy graphene.....	56
Table 3.4. Covalent NBOs for Pt ₁₃ on divacancy graphene.....	56
Table 4.1. Lowest energy (in eV) found by GA and simulated-annealing (SA) method.....	64
Table 4.2. Electronic configurations and confinement potential parameters for Pt and Ru.....	65
Table 4.3. Calculated structural and energetic properties of Pt and Ru in the bulk phase. Listed below are lattice constants <i>a</i> and <i>c</i> , cohesive energy per atom E_{cov} , formation energy E_f , and surface energies.....	69

LIST OF FIGURES

Figure	Page
Figure 2.1. Flow chart and schematic representation of optimization process for unsupported clusters with GA.	17
Figure 2.2. Minimum-energy structures of unsupported Pt clusters as predicted by our GA implementation using Albe et al.'s bond-order potential.	21
Figure 2.3. Geometries of low-energy “magic-number” Pt isomers in vacuum. The first two rows display high symmetry clusters cuboctahedral (Oh) and icosahedral (Ih) clusters. The third row displays minimum-energy structures found by the GA with an empirical potential.	23
Figure 2.4. Average d-band center energy of the surface atoms, $\overline{\epsilon}_d^{\text{surf}}$, as a function of cluster size, N. The solid curve passing through data for GA-optimized structures is merely a guide to the eye. Error bars are standard deviations; representative error bars are shown only for certain sizes to maintain legibility. The exact values of d-band center energy with confidence intervals for every data point can be found in Table 2.4. Horizontal dashed lines indicate the reference d-band center energies on bulk-terminated, FCC Pt (111) and (100) surfaces.	26
Figure 2.5. Distribution of coordination numbers (blue bars) as well as d-band center energies of atoms on the surface (black “+” symbols) and in the bulk (red “+” symbols) for the cuboctahedral Pt309 cluster. Surface d-band centers of FCC Pt (111) and Pt (100) surfaces are shown for reference.	28
Figure 2.6. DFT-calculated CO adsorption energies on the surface sites of Pt clusters versus the prediction from GBR model with different sets of descriptors: (a) Generalized d-band center, (b) Type 2 descriptors, (c) $E_{\text{ads}}^{\text{AF}}$ alone, (d) Generalized d-band center and Type 2 descriptors (e) all three descriptor types (5 descriptors total). Reported AME (absolute mean error) of the model predictions are the average over six-fold cross validation to avoiding splitting bias. The displayed data points are from one such randomly split dataset. Insets in (b), (d) and (e) show the relative importances of the descriptors in the models.	34
Figure 2.7: DFT-calculated CO adsorption energies on the surface sites of Pt clusters versus the prediction from GBR model with all descriptors. Below is a list of the descriptors used for this figure:	35
Figure 3.1. Defect-free and defective graphene substrates employed in this study	42
Figure 3.2. Minimum-energy structures of Pt_N ($N = 2, 3, 4, 13$) on pristine graphene (upper row), and graphene with single vacancy (middle row) and divacancy defects (bottom row).	46

Figure 3.3. Evolution of structural and energetic properties of global minima of Pt_N /graphene calculated using the GA as a function of particle number N : (a) radius of gyration; (b) average coordination number of Pt atoms (excluding Pt-C bonds); (c) average Pt-Pt bond length (dashed line is for bulk FCC Pt); (d) fraction of active surface atoms, defined in equation 3.3; (e) adsorption energy (E_{ad}) of Pt clusters on graphene; (f) average contribution of Pt atoms at the Pt-C interface to E_{ad} .	48
Figure 3.4. Position of d-band center (ϵ_d , Pt) relative to the Fermi level (a) and net charge transferred (b) to Pt_{13} isomers in vacuum and on graphene support. Data for Pt_{13} clusters in vacuum and on support are plotted with respect to the formation energy (E_f) per atom and the adsorption energy (E_{ad}), respectively. The horizontal dashed line represents ϵ_d , Pt for Pt(111) surface. Other dash lines are guides to the eyes. Points inside dashed square correspond to structures with Pt atoms occupying the center of the defect.	53
Figure 3.5. Pt_{13} clusters on vacancy (a) and divacancy (b) graphene support. Red labels are the index of atoms forming valence bond at the interface.	55
Figure 3.6. DFT adsorption energies for selected Pt_N clusters in the size range $N = 20-80$ on defective and defect-free graphene supports.	57
Figure 3.7. Charge (Δq in electrons) transferred from Pt_N clusters to defective and defect-free graphene supports for selected clusters in the size range $N = 20-80$.	57
Figure 4.1. Fitting the derivatives of repulsive potential: (a): Pt-Pt interaction; (b): Ru-Ru interaction; (c): Pt-Ru interaction. Family of points are from various structures. Here $r_{cu} = 3.3 \text{ \AA}$.	67
Figure 4.2. Comparison of DFT and DFTB formation energies of Pt, Ru and PtRu clusters. Dashed lines indicate the least-squares fit to the data. The slopes of the lines (ideally unity) and the R2 values indicate an accurate DFTB representation of the target DFT data.	70
Figure 4.3. Morphologies of minimum-energy PtRu clusters of various sizes (N – number of atoms) and compositions (x – Pt fraction) as predicted by our DFTB-based GA implementation. Gold and pink spheres represent Pt and Ru atoms, respectively.	72
Figure 4.4. Formation energies of GA-optimized PtRu clusters (displayed in Figure 4.3) as a function of Pt concentration, calculated with (a) DFT and (b) DFTB. Cluster sizes (number of atoms) are indicated in the legends.	73

CHAPTER 1

INTRODUCTION

1.1 What Are Fuel Cells?

Fuel cells are devices that convert chemical energy, stored in a variety of chemicals (H_2 , methanol, methane, etc.) into electrical energy through electrochemical reactions. Fuel cells are classified by either the type of fuel employed or by the mobile charged species. The PEMFC (Proton Exchange Membrane Fuel Cell) and the closely related direct methanol fuel cell (DMFC) are more suited to terrestrial activities and are believed to be the future replacements of batteries and combustion engines. Typically, a fuel cell will oxidize the fuel at its anode and reduce oxygen at its cathode. Electrons from fuel molecules (e.g. H_2) can be released by the oxidation reaction at the anode, pass through an external circuit to do electrical work, and finally reduced oxygen at the cathode. Charged species (e.g. H^+) diffuse through the fuel cell and react with reduced oxygen.

Since William Robert Grove built the first fuel cell in 1839, extensive research has been conducted on catalysts, stacks and systems to achieve high efficiency and reliability towards commercialization. Compared with traditional combustion technology, which depends primarily on fossil fuels, fuel cells are promising candidates for next-generation energy production due to their *high efficiency* and *environment friendliness*. Energy cost, which depends primarily on the conversion efficiency, is the most important aspect of any energy-conversion technology. Fuel cells are electrochemical engines, not heat engines, and thus not subjected to Carnot Cycle limitations.¹ High conversion efficiency up to 80% can be achieved under certain conditions and, consequently, it is expected that in the present century fuel cells will replace heat engines (internal combustion engines, steam or

gas turbines) as fuel prices increase. Moreover, global carbon emissions from fossil fuels have raised public and political awareness. CO₂ emissions have increased by about 90% since 1970, and about 78% of the total greenhouse gas emissions are from fossil fuel combustion and industrial processes.² Considering that energy is a major contributor to the greenhouse gas emissions, fuel cells with high efficiency and high potential to use low or zero-carbon fuel resources (H₂, for example) can help alleviate global warming, especially if the fuels are derived from renewable and clean processes. For example, hydrogen can be produced from a diverse portfolio of energy sources, including nuclear, coal, natural gas, geothermal, wind, hydroelectric, solar, and biomass. Thus, fuel cells offer an environmentally clean and energy-secure pathway. In addition, unlike combustion processes that use fossil fuels and produce harmful pollutants such as SO₂ and NO_x, fuel cells release almost zero harmful gases and have the potential to improve air quality in many big cities. Also, unlike other renewable energy resources such as wind, solar, hydropower, and geothermal energies that are diffuse and intermittent, fuel cells can generate energy stably and reliably as long as fuels are provided.

1.2 Challenges

For fuel cells to operate at high power density and high efficiency, catalysts are required at both electrodes to lower reaction barriers and accelerate reaction rates. Platinum (Pt) has been found to be the best pure metal in terms of activity, selectivity, and stability for the hydrogen oxidation reaction (HOR) and oxygen reduction reaction (ORR) in a fuel cell.³⁻⁵ A recent review provides an insight into why platinum performs so well in fuel cell electrochemistry and explains the different failure mechanisms which

thus far have prevented other materials from being used.⁶ In brief, for the preferred two-step ORR pathway that requires the catalyst to first bind O and then OH, Pt displays nearly optimal binding energy for both steps and thus shows the highest activity. Nevertheless, there are still several challenges that must be overcome to improve Pt-based fuel cells:

i. *Cost.* Despite of the outstanding catalytic performance in fuel cells, Pt is an extremely rare element (at the level of 0.003 ppb) and the high price of Pt (\$987/oz at the time of writing) hurts the economics of fuel cell technology. The slow kinetics at the cathode is one of the largest sources of inefficiency in fuel cells, requiring high platinum catalyst loading. According to the most recent DOE analysis,² Pt contributes to 43% of the total cost of the 80 kW PEM systems, when manufactured at a volume of 500,000 units/year. Therefore, there is a significant need for reducing Pt usage in fuel cells while maintaining high efficiency of energy conversion.

ii. *Durability.* Catalyst durability is another major technical barrier to fuel cell commercialization. In practice, Pt is used in its nanoparticle form to achieve high surface-to-volume ratio and maximally utilize the precious metal for surface reactions. However, at the same time, smaller particles tend to show lower stability. Thermodynamically, nanoparticles are metastable and inherently show a strong tendency to agglomerate due to high specific surface energy. When nanoparticles agglomerate to form bigger particles, the electrochemical surface area (ECSA) of the catalyst decreases and degrades fuel-cell performance. For example, Pt-based ORR catalysts are known to degrade quickly under typical fuel-cell operating conditions, such as frequent load cycling.

iii. *CO Poisoning.* CO is a notorious catalyst poison and deactivates catalysts,⁷⁻⁸ by binding strongly with surface atoms and blocking the active sites. CO is a common

impurity in the fuels for fuel cells. For example, 95% of the hydrogen produced in the United States today is made by natural gas reforming in large central plants⁹ and the reformed feed gas may contain up to 5 % CO by volume, which can be reduced to 100 ppm using a selective oxidizer.¹⁰⁻¹¹ Nevertheless, even such small traces of CO can cause significant reduction in fuel cell performance. Alternatively, CO may be produced as a reaction intermediate in indirect reaction pathways (e.g., methanol oxidation in DMFCs) and hinder the electrocatalytic reaction by blocking the Pt surface.¹²

1.3 Catalyst Development

To address the above challenges, it is necessary to understand the key factors that determine the performance of Pt catalysts. In recent years, increasing efforts have been made towards rational design and engineering of Pt catalysts to achieve higher efficiency, stability and resistance to CO poisoning. Below, we discuss a few key factors towards optimizing Pt catalysts including the effects of catalyst size and shape, support interactions and alloying.

1.3.1 Size and Shape Effect

It is generally desirable to prepare small Pt nanoparticles to attain high ECSA while optimally utilizing the precious metal. As cluster size decreases, the coordination of surface atoms decreases and the local environment becomes drastically different from bulk-terminated surfaces, which in turn alters the binding strength of adsorbates and thus, the catalytic performance. As an example, ultra-small (~1 nm) nanoparticles begin to present significant deviations in properties relative to their larger, bulk-like counterparts and examples of such behavior have been shown in many cases experimentally and

computationally,¹³⁻¹⁵ a particularly well-known example is gold, which is normally inert but turns into an effective catalyst when synthesized in nanocluster form.¹⁶⁻¹⁸

Despite intensive work in the last two decades, there still remains a debate on the effect of Pt particle size on the catalytic activity and CO resistance.¹⁹⁻²⁸ This is to a large extent due to the fact that nanoparticles synthesized in experiments have a wide size distribution (approximately ± 2 nm) and their morphology too can differ greatly under different experimental preparation conditions. Shao et al.²³ investigated the activity of Pt particles with sizes between 1–5 nm, and found that the specific activity (the reaction rate normalized to the surface area of the catalyst) of Pt nanoparticles decreases sharply when particles are smaller. While they found that the electroactive surface area increases with smaller size, a maximum mass activity (the reaction rate normalized to the mass of the catalyst) being achieved at ~ 2 nm, they attributed the lower specific activity at smaller sizes to the predominance of edges and kinks that bind strongly to oxygen. However, A Nesselberger et al.²² reported a consistent increase in mass activity as they reduced the size of their Pt particles from 30 nm to 1 nm with rather small variations of specific activity. The activity of ultra-small Pt nanoparticle (<1 nm) is even more interesting as the shape of cluster starts to play a more important role than size. For example, by using a dendrimer ligand as the macromolecular template, Imaoka et al.²⁹ successfully synthesized atomically-precise clusters and showed that the ORR activity of C_{2v} Pt₁₂ clusters is twofold lower than that of icosahedral Pt₁₃. They concluded that no simple relationships between size and activity exist in the sub-nanometer regime.

Similarly, there are only a few investigations on understanding shape and size effects on the CO tolerance of Pt. It has been observed that for CO oxidation reaction,

catalytic properties of Pt nanoparticles at the nanometer size range can also become exquisitely sensitive to the particle structure, adding more complexity and difficulty into understanding the size and shape effect.^{17, 30-32} Theoretical work in this thesis aims to unravel some of these issues.

1.3.2 Support Effect

Another popular method to improve the activity of Pt is to deposit particles on porous supports. The primary function of supports is to immobilize small particles through steric hindrance or strong binding, thereby enabling higher particle dispersion and preventing particle sintering and catalyst dissolution.³³⁻³⁴ Moreover, supports also provide an extra degree of freedom in tuning the electronic properties of clusters and altering their catalytic performance. Several studies have revealed that the physical properties of supports can greatly affect the structural and electrochemical properties of the fuel cell catalyst.³⁵⁻³⁹

Carbon is one of the most common supports for polymer electrolyte membranes due to its abundance, good electrical conductivity (for certain carbon materials such as carbon black or graphene), and stability against corrosion in both acidic and basic environments. High-surface-area activated carbon and carbon blacks (i.e. commercial Vulcan XC-72 or Black pearl 2000) have been extensively used as supports in low temperature fuel cells due to their low cost and ready availability. However, the presence of a large number of micropores hinders reactant flow. Moreover, these materials present low stability at elevated temperatures ($>100\text{ }^{\circ}\text{C}$).⁴⁰⁻⁴¹ Recent developments in nanotechnology have enabled better control of the morphology and structure of carbon

supports and have provided a variety of new types of carbon-based nanostructured materials such as graphene and carbon nanotubes (CNTs). A high degree of crystallinity enables these advanced materials to exhibit several promising features such as high conductivity, high surface area, and faster mass diffusion of reactants.

Several experiments have demonstrated the superior performance of Pt/graphene nanocatalysts in direct-methanol fuel cells,⁴²⁻⁴⁴ proton-exchange membrane fuel cells (for ORR),⁴⁵ and hydrogen fuel cells.⁴⁶ The improved performance has been quantified via metrics such as electrocatalytic activity, tolerance to CO poisoning, and long-term stability towards catalyst sintering. Investigators typically attribute such improvements in catalytic performance to the synergistic interactions between the Pt catalyst and the graphene support, mediated by defects and functional groups in the graphene support that act as strong binding sites for catalyst nanoparticles.^{44-45, 47-51} Computational studies corroborate this interpretation and show strong binding of Pt clusters at support defects in graphene, accompanied by a significant modification of the morphology and electronic structure of the clusters.⁵²⁻⁶¹ In particular, *ab initio* studies indicate a noteworthy correlation between the binding energy of a Pt cluster at a support defect and the *d*-band center of the cluster, which suggests an additional pathway for optimizing catalytic activity through defect engineering of supports.⁵⁸⁻⁶⁰

1.3.3 Pt-based Alloys as Catalysts

By alloying Pt with other transition metals (either as bimetallic or ternary systems) or non-noble metals, usage of Pt as well as the cost of catalyst can be significantly reduced. The catalytic properties of Pt are strongly affected by the alloying metals through strain

effects (change of Pt-Pt distance)⁶²⁻⁶⁵ and electronic effects (change of Pt *d*-orbital occupancy or *d*-band center energy).⁶⁶⁻⁶⁷ It is well known that by partially alloying Pt with another metal, both CO tolerance and electrocatalytic activity can be improved. For example, PtRu,^{3, 68-69} PtCo,⁷⁰⁻⁷¹ , PtMo,⁷²⁻⁷³ PtNi,⁷⁴⁻⁷⁷ PtFe,⁷⁸⁻⁸³ PtAg,⁸⁴⁻⁸⁵ PtCu,⁸⁶⁻⁹¹ PtAu⁹²⁻⁹⁸ alloys have been synthesized and investigated as anode materials for fuel cells and, currently, PtRu alloy clusters are known to show the highest resistance to CO poisoning and best catalytic activity in PEMFCs.⁹⁹ The superior performance of PtRu over Pt clusters has been explained by invoking the ligand effect,¹⁰⁰⁻¹⁰¹ which reduces the binding strength of CO at active sites, as well as a bifunctional mechanism,¹⁰² which accesses alternate pathways with reduced energy barriers for the oxidation and elimination of CO. A continuing challenge for the application of Pt–transition metal alloys in phosphoric acid (PAFC) and polymer electrolyte membrane (PEMFC) fuel cells is the poor stability of these binary catalysts. Dissolution of the non-precious metal in the acid environment can reduce the activity of these catalysts and degrade cell performance.

1.4 Thesis Objectives

Today, fuel cells are attractive power-conversion devices with higher energy conversion efficiency and lower environmental impact than traditional combustion engines. One of the most challenging tasks in fuel-cell commercialization is to reduce precious metal usage through rational design and optimization of catalysts. Towards this end, this thesis focuses on establishing a fundamental theoretical understanding of the relationships between the catalytic performance of Pt nanoclusters and various essential design factors, including catalyst size and structure, support effects, and alloying. Our computational

studies combine first-principles density functional theory (DFT) modeling with robust empirical-potential-based structure-optimization techniques. Empirical potentials provide an inexpensive route to mapping the potential-energy surface of material systems, enabling extensive investigation of thermodynamic stability of competing metastable structures. DFT calculations, on the other hand, enable accurate exploration of the electronic properties that are relevant to Pt–adsorbate binding and ultimately determine the catalytic properties.

In Chapter 1, the interplay between structure, size, and electronic properties of Pt nanoclusters, and their ultimate impact on adsorbate binding is presented. The thermodynamic stability of pure Pt nanoclusters is investigated using a Genetic Algorithm (GA) that allows for extensive exploration of the potential energy hypersurface. The evolution of electronic properties and CO-adsorption thermodynamics with Pt cluster size are reported. Structural effects are elucidated by comparing computational results for high-symmetry clusters, which are commonly used in literature, with those for true low-energy isomers found by global optimization. Finally, machine-learning algorithms are applied to the DFT data to identify reliable structural and electronic descriptors for CO adsorption energies. The results in this chapter have appeared in the following publications:

- Shi, H., Auerbach, S. M.; Ramasubramaniam, A., *First-Principles Predictions of Structure Function Relationships of Graphene-Supported Platinum Nanoclusters*. J. Phys. Chem. C. **2016**, 120, 11899-11909.
- Gasper, R.,* Shi, H.,* Ramasubramaniam, A. “*Adsorption of CO on Low-Energy, Low-Symmetry Pt Nanoparticles: Energy Decomposition Analysis and Prediction via Machine-Learning Models*”, J. Phys. Chem. C, **2017**, 121, 5612-5619 (* Equal

contribution: Hongbo Shi performed GA optimization of Pt nanoclusters and applied machine-learning algorithms to CO adsorption data.)

In Chapter 2, a detailed study of the support effect on the structure and electronic properties of Pt nanoclusters is presented. We examine the influence of point defects in graphene supports on the electronic structure of supported Pt nanoparticles by studying and contrasting graphene monolayer supports that are either defect free (pristine) or contain vacancy and divacancy defects. We first investigate the stability of Pt nanoclusters using a GA for global optimization. Thereafter, the role of graphene supports as well as their point defects in modifying cluster morphologies is analyzed with respect to various structural properties of the supported clusters. The binding strength between supports and Pt clusters is probed to provide essential information towards understanding experimental observations of improved stability of Pt catalysts on graphene supports. Finally, DFT calculations are employed to further probe the modification of electronic structures of Pt nanoclusters by the support and provide a qualitative understanding of experimental observations of improved CO tolerance.

The results in this chapter have appeared in the following publication:

- Shi, H., Auerbach, S. M., Ramasubramaniam, A., *First-Principles Predictions of Structure Function Relationships of Graphene-Supported Platinum Nanoclusters*. J. Phys. Chem. C. **2016**, 120, 11899-11909.

In Chapter 3, we investigate the thermodynamic properties of PtRu alloy clusters as a function of cluster size and composition. To the best of our knowledge, no viable empirical potential has been developed for PtRu clusters. Thus, the first focus of this

chapter is then to develop an accurate and computationally inexpensive semi-empirical model for PtRu alloys. We present in detail the parameterization of a Self-Consistent Charge Density-Functional Tight-Binding (SCC-DFTB) model for Pt-Pt, Ru-Ru and Pt-Ru interactions. The accuracy of this model as well as the developed parameter sets are demonstrated by comparison with DFT calculations. Finally, we apply our GA to search for low-energy structures of PtRu and demonstrate the emergence of core-shell structures at intermediate alloy compositions in accord with experiments.

Chapter 5 summarizes the most important results and conclusions of this thesis, and also provides suggestions for further research in the field of catalyst design and optimization.

In addition to the main topics in Chapter 1-5, we also present in Appendices A and B my journal publications on Pt nanocluster catalysts and on understanding the thermal and mechanical behavior of zeolites, which are important catalysts used for biomass conversion process. The findings of Appendix B have appeared in the following publication:

- Shi, H., Migués, N. A., Auerbach, S. M. "*Ab initio and classical simulations of the temperature dependence of zeolite pore sizes*". *Green Chemistry*, **2014**, 16, 875

CHAPTER 2

STABILITY, ENERGISTICS, AND CATALYTIC PROPERTIES OF UNSUPPORTED PT NANOCLUSTERS

2.1 Introduction

Ultra-small (<1 nm) nanoparticles begin to present significant deviations in properties relative to their larger, bulk-like counterparts. Examples of such behavior have been shown in many cases experimentally and computationally,¹³⁻¹⁵ with the particularly well-known example of gold, which is normally inert, turning into an effective nanoclusters catalyst.¹⁶⁻¹⁸ In addition, it has been observed that, at the sub-nanometer size range, catalytic properties of nanoparticles can become exquisitely sensitive to the particle structure, adding more complexity to the issue.^{17, 30-32} Hence, in this chapter we seek to understand the properties of sub-nanometer Pt clusters, as they correlate with changing particle size, and attempt to find suitable predictors for adsorbate binding energies that can help circumvent expensive DFT calculations. Multiple computational groups have also addressed this topic but with a key limitation, namely, focusing only on high-symmetry cluster morphologies.^{14, 103-105} Experimental evidence and computational modeling have shown that real nanoparticles do not adopt high-symmetry structures, and instead adopt somewhat disordered low-symmetry structures.¹⁰⁶⁻¹⁰⁸ The effects of such morphological variations on the electronic structure are particularly noticeable at small size clusters, as shown in our previous work on supported and unsupported Pt₁₃ nanoclusters.^{59, 109} In the present work, we present a systematic analysis of the influence of cluster size and morphology on adsorbate binding using the well-known catalyst poison, carbon monoxide, as an example.

The first key feature of our current work – at variance with previous studies^{14, 103, 105} – is that we conduct CO adsorption calculations on low-symmetry, low-energy nanoclusters. These cluster morphologies are obtained by the application of an empirical bond-order potential driven Genetic Algorithm (GA), described in our previous work.¹⁰⁹ As shown in that work, the empirical-potential-based GA reliably predicts low-energy, low-symmetry cluster morphologies as confirmed via DFT calculations across a range of cluster sizes. Hence, this approach both allows us to examine realistic minimum-energy structures for a range of nanoparticle sizes, and eliminates having to decide between the fitness of various arbitrary, high-symmetry geometries. Once low-energy cluster morphologies are obtained from the GA at relatively low computational cost, the remainder of the computational effort can be expended in higher-level DFT calculations of adsorbate binding on these clusters. One of the main challenges of investigating adsorbate binding on these low-symmetry structures is that they generally do not possess symmetry-equivalent sites unlike bulk-terminated crystal facets and high-symmetry clusters. Because of this, some form of statistical sampling must be undertaken for calculating even simple adsorption properties, requiring a compromise between accuracy and computational effort spent on repeatedly sampling the same cluster. Thus, it becomes extremely useful to be able to predict both average as well as site-specific adsorption energies on these disordered structures using relatively simple structural metrics and/or limited electronic structure information without having to undertake full-blown DFT adsorption calculations on every available surface site. In order to approach this challenging problem, the second key feature of our work is the application of a machine-learning tool¹¹⁰⁻¹¹¹ to the prediction of CO adsorption energies on sub-nanometer Pt clusters. The use of machine learning techniques

in materials science is in its infancy and growing,¹¹²⁻¹¹³ and a few groups have recently explored using machine learning for predictions of adsorbate binding on transition-metal surfaces, reporting modest errors (~ 0.1 eV) with respect to DFT.¹¹⁴⁻¹¹⁵ The so called gradient-boosting algorithm was used recently by Takigawa *et al.*¹¹⁶ to accurately predict the *d*-band center of bulk alloys and alloy surfaces based only on mechanical and structural properties, demonstrating the potential usefulness of machine learning approaches for computational catalysis research. To the best of our knowledge, machine-learning algorithms have yet to be applied to predict adsorbate binding on clusters and our work represents an early example of the promise of this approach to this class of problems.

2.2 Methodology

2.2.1 GA for Optimization of Unsupported and Supported Clusters

Structural optimization of nanoparticles/clusters entails the nontrivial task of efficiently identifying the global minimum on a complex PES by performing unbiased sampling. Several global optimization techniques have been developed to address this challenge, including basin-hopping,^{107, 117-120} particle-swarm optimization,¹²¹⁻¹²² and GAs.¹²³⁻¹²⁴ In this work, we chose to implement a GA¹²⁵ to determine low-energy structures of unsupported Pt clusters. Local energy optimization was implemented using the LAMMPS package.¹²⁶ In general, the GA produces child clusters from parent clusters by splitting parents in half and cross-mating to form children. At each new generation, local optimization is performed to drain high energies that arise from mating. Promising child clusters then become the parents for the next iteration of the GA, continued until the energies of promising clusters converge within a given tolerance. The specific approach

followed here, in particular for optimization of supported clusters, follows the spirit of the pioneering work of Chuang and coworkers;¹²⁷ the individual steps of the GA are illustrated in Figure 2.1 and discussed in detail below.

Initial Population: For a given cluster Pt_N, initial configurations for the starting generations are randomly generated with a minimum Pt-Pt distance of 1.7 Å to avoid biased searching. The quality of the i^{th} cluster with energy E_i is determined by its fitness f_i , which is calculated by a linear function¹²⁵

$$f_i = 1 - 0.7\rho_i, \quad (2.1)$$

where the scaled energy ρ_i is normalized as

$$\rho_i = (E_i - E_{\min})/(E_{\max} - E_{\min}), \quad (2.2)$$

where E_{\min} and E_{\max} are the lowest and highest energies of the initial configurations. The scaled energy ρ_i for each configuration is thus always between 0 and 1; as such, the fitness values corresponding to the lowest and highest energies are 1.0 and 0.3, respectively.

Selection: A selection operator is used to choose candidates from the current generation for mating. Here, we use the roulette wheel method of selection:¹²⁵ a configuration is chosen at random and selected for mating if its fitness value ρ_i is greater than a randomly-generated number between 0 and 1. Otherwise, another configuration is chosen at random and tested for mating. This process is continued until two configurations are chosen for mating.

Crossover: Crossover refers to the process by which “genetic” information (coordinates) from two parent clusters is combined to generate offspring. For unsupported (vacuum) clusters, the centroids of the two parent clusters are shifted to the origin, after

which the parents are subjected to random rotations. The plane at $z = 0$ is used to cut each parent cluster into two parts; the top half of Parent 1 and bottom half of Parent 2 are then “glued” together to form a new child. (To conserve particle number between parents and offspring, the cutting plane might require a slight offset from the $z = 0$ position.) A minimum separation of 1 Å is maintained between the glued cluster halves to avoid artificially high energies and/or forces on atoms.

Natural Selection: In natural evolution, individuals with higher fitness are more likely to survive and pass on their genes. In our GA, clusters with lower energies have higher fitness and are chosen with higher probability for reproduction. The energy evaluation is performed using the LAMMPS package. To facilitate rapid initial relaxation of randomly generated offspring, we employ low-temperature molecular dynamics at 100 K for 0.1 ps using a 1 fs time step. Thereafter, conjugate-gradient minimization is performed for a minimum of 100 iterations or until the norm of the energy gradient on each atom is less than 10^{-3} eV/Å. The new offspring is accepted if its energy falls below an acceptance threshold

$$E_{accept} = E_{min} + N_{Pt} \times \Delta E, \quad (2.3)$$

where E_{min} is the lower energy of the two parents, N_{Pt} is the number of Pt atoms in the cluster, and ΔE is a numerical parameter. The smaller the value of ΔE the more stringent is the acceptance criterion; from numerical testing, $\Delta E = 0.1$ eV was found to be a reasonable choice. We note that this parameter (ΔE) is system-specific and can be ascertained through a small initial set of calibration runs.

Elite species: The population size is maintained at 30 individuals throughout the optimization process. To avoid loss of high quality species, within any generation we always maintain 20% of fittest individuals from the previous generation.

Convergence: The GA was deemed to have converged if the lowest energy clusters in each generation remained unchanged for 20 generations or if the total number of generations exceeded 1000.

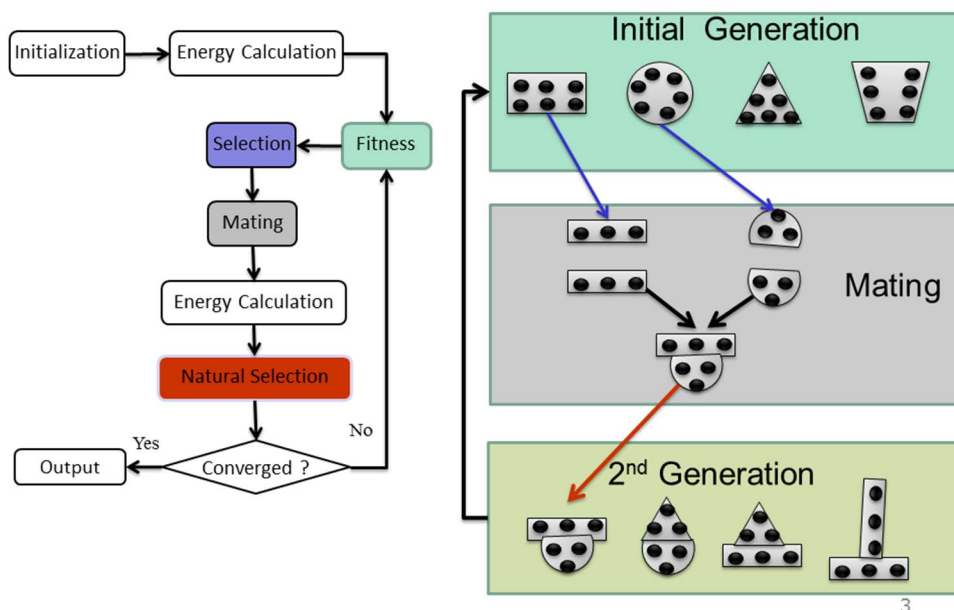


Figure 2.1. Flow chart and schematic representation of optimization process for unsupported clusters with GA.

2.2.2 Empirical Potential Models for Pt-Pt Interaction

In this chapter, we employ a Pt interatomic potential developed by Albe et al.¹²⁸ based on the reactive bond-order Tersoff-Brenner form¹²⁹ for Pt-Pt interactions. Here, we carry out a more extensive investigation of the fidelity of this potential for unsupported clusters, and show that this potential is generally in very good agreement with DFT structural models. We also perform careful tests of Albe et al.'s potential for supported

clusters (See Chapter 3) and demonstrate that the potential is indeed capable of delivering accurate low-energy structures for further electronic structure analyses. All empirical potential simulations are performed using the LAMMPS simulation package.

2.2.3 DFT Calculations

DFT calculations are performed to study the thermodynamic and electronic properties of selected low-energy structures using the Vienna Ab initio Simulation Package (VASP).¹³⁰⁻¹³¹ Core and valence electrons are described using the Projected Augmented Wave method.¹³²⁻¹³³ The Perdew-Burke-Ernzerhof (PBE)¹³⁴⁻¹³⁶ form of the generalized-gradient approximation is employed to describe electron exchange and correlation. A kinetic energy cutoff of 400 eV is used for the plane-wave basis set and the conjugate gradient algorithm is used to relax ions into their ground state until the force on any atom is smaller than 0.01 eV/Å. Brillouin zone sampling is performed using a single Gamma point for unsupported clusters. From convergence tests (Table 2.1), at least 10 Å of vacuum is used to eliminate spurious interactions between periodic images of Pt clusters.

2.2.4 Simulation Procedure

Realistic structures for Pt_N ($N = 4-309$) clusters were obtained by sampling the hyper-dimensional energy surface using a GA. To ensure better sampling, we run three GA simulations for each particle size, and the geometry with the lowest energy from all simulations is chosen as the candidate representing the global minimum. In almost all cases, the geometries obtained at the end of these three simulations are identical, indicating the robustness of GA. For larger sizes (147 and 309), the lowest-energy structures found by three independent optimization processes are different, due to the significant increase in

complexity of the potential energy surface and thus the computational demanding. By extensive exploration with the GA, we establish an ensemble of minimum and near-minimum energy Pt_N isomers. From the converged GA results, various structural properties of clusters such as the radius of gyration, coordination numbers, and average bond lengths are calculated.

Table 2.1. Total energy (eV) of Pt_7 clusters

Image distance(\AA)	Energy(eV)
3.0	-28.22
5.7	-26.57
7.1	-26.57
8.6	-26.64
10.0	-26.64
11.4	-26.64

2.3 Result and Discussion

2.3.1 Structure and Energetics of Unsupported Pt Clusters

Several DFT-based studies have focused on the structure and energetics of unsupported Pt clusters,¹³⁷⁻¹⁴⁰ thereby providing a basis for evaluating both the quality of the empirical potential used in this work as well as the robustness of the GA. Thus, we focus first on unsupported clusters and present a critical evaluation of our simulation methods. A common shortcoming in studies of clusters is that the methods for generating low-energy structures do not use global search algorithms, relying instead on less robust techniques such as simulated annealing. Adopting high-symmetry shapes based on geometric shell models is usually incorrect for small transition-metal clusters as has been well documented in the literature.¹³⁷⁻¹³⁹ As we shown in this work, combining global search

algorithms, such as GAs, with inexpensive yet reliable empirical potentials thus offers a significant advantage for reliable and efficient sampling of the PES.

Table 2.2. Relative total energies (in eV) of Pt_7 isomers from Kumar et al.’s¹³⁷ and our DFT calculations (PBE functional; PW91 results in parentheses), as well as Albe et al.’s empirical potential (EP). Energies are relative to the lowest energy isomer for each level of theory.



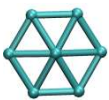
geometry	DFT (Ref. ¹³⁷)	DFT (this work)	EP
	0.00	0.00 (0.00)	unstable
	0.08	0.07 (0.06)	0.59
	0.12	0.38 (0.07)	0.00

Figure 2.2 displays the lowest energy structures of Pt_N ($N = 2-80$) found by our GA implementation using Albe et al.’s bond-order potential. Figure 2.2 shows that Pt clusters are planar up to $N = 8$ atoms, which is consistent with the DFT study reported by Kumar et al.¹³⁷ Furthermore, none of the minimum-energy structures exhibits high-symmetry, calling into question common assumptions about enforcing symmetry made in cluster catalysis studies. To examine the accuracy of the empirical potential in greater detail, we focus on $N = 7$ clusters as a specific example. For Pt_7 clusters, the GA predicts a centered six-member ring as the lowest energy structure (see Table 2.2). However, both Kumar et al.’s and our DFT results show that side-capped isomers turn out to be lower in energy than the centered ring. Of these side-capped structures, only one is even stable as per the empirical potential (see Table 2.2) and the energy is appreciably higher (~ 0.6 eV) than that of the centered-ring structure. Of course, the GA prediction can only be as good as the underlying model and, to this extent, the discrepancy between the empirical potential and

DFT points to shortcomings of the former. It should be noted, though, that the centered-ring structure is fairly close in energy to the side-capped ground state at the DFT level (within 0.06 – 0.08 eV).

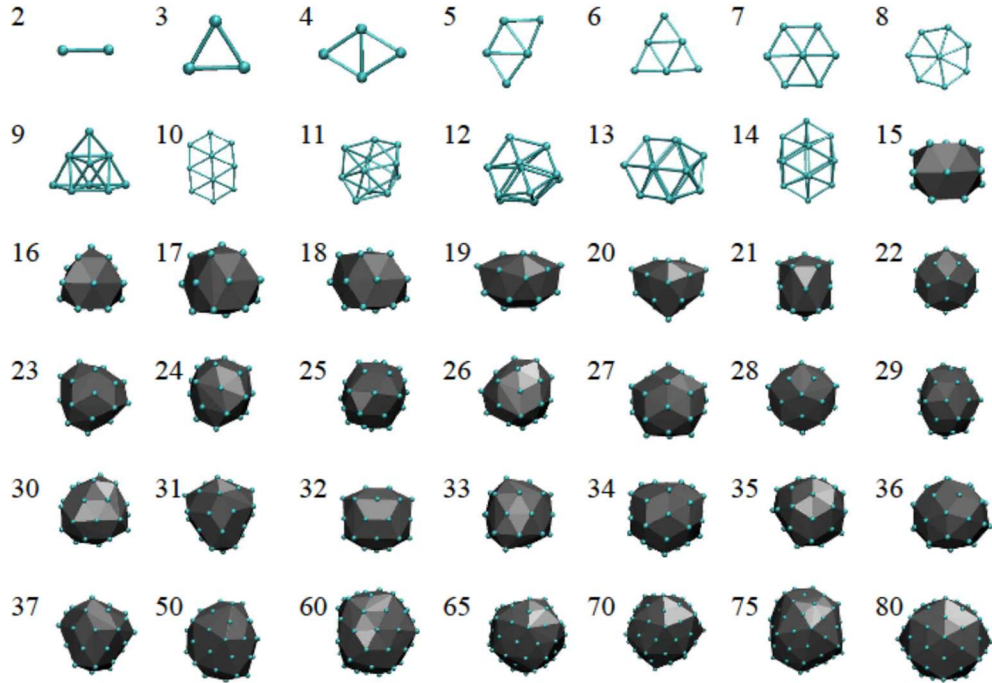


Figure 2.2. Minimum-energy structures of unsupported Pt clusters as predicted by our GA implementation using Albe et al.’s bond-order potential.

The efficacy of the combined empirical-potential and DFT approach becomes much more apparent when searching for minimum-energy structures of large clusters. As examples, we consider so-called “magic-number” Pt_{13} , Pt_{55} , Pt_{147} , and Pt_{309} clusters, which have been studied widely in their high-symmetry cuboctahedral (O_h) and icosahedral (I_h) structural motifs.^{14, 105, 141} As before, we use the GA to find minimum-energy structures for these various cluster sizes and then further relax the minimum-energy structures in DFT. The energies of the DFT-relaxed structures are then compared with corresponding DFT energies for the high-symmetry O_h and I_h structures; total energy differences relative to the

minimum-energy structure for each cluster size are reported in Table 2.3. These results show clearly that the high-symmetry structures are not the lowest-energy structures, as was also shown in previous DFT studies of Pt₁₃ and Pt₅₅ clusters.¹⁴⁰⁻¹⁴¹ Indeed, the results obtained here for larger clusters are particularly striking and prompt interesting questions regarding typical sizes at which transitions from low-symmetry to high-symmetry clusters may be expected to occur in faceted crystals of Pt nanoclusters; such issues will be discussed later in this thesis.

Table 2.3. Relative total energies (in eV) of high-symmetry (cuboctahedral – Oh; icosahedral – Ih) Pt clusters and GA-optimized, low-energy clusters calculated using DFT and Albe et al.’s empirical potential (EP). Energies are relative to the lowest energy isomer for each size and level of theory.

	Pt ₁₃		Pt ₅₅		Pt ₁₄₇		Pt ₃₀₉	
	DFT	EP	DFT	EP	DFT	EP	DFT	EP
I _h	1.3	1.7	3.3	3.4	6.5	5.1	7.7	5.6
O _h	2.0	1.8	5.1	6.4	8.2	12.4	9.7	18.4
GA	0.0	0.0	0.0	0.0	0.0	0.0	0.0	0.0

It is also apparent from these results that the performance of Albe et al.’s empirical potential—in terms of relative energetic ordering of structures—is surprisingly good when compared with DFT calculations, especially considering that the potential was parameterized for bulk properties. The lowest-energy structures found by the GA essentially resemble defective icosahedra that are approximately 0.01-0.1 eV/atom lower in energy (across the entire range of sizes) than the perfect icosahedra. Cuboctahedral structures are in general higher in energy than both the GA-optimized structures and the perfect icosahedra.

Overall, the benchmarking studies presented here lead us to two principal conclusions. First, Albe et al.’s bond-order potential is of sufficient accuracy to deliver near-minimum energy structures of unsupported clusters, which can then be subjected to

additional optimization in DFT calculations. Second, our GA implementation is able to deliver reliable minimum-energy results for unsupported clusters, which then lends us confidence in proceeding to the study of supported clusters, the subject of the next chapter.

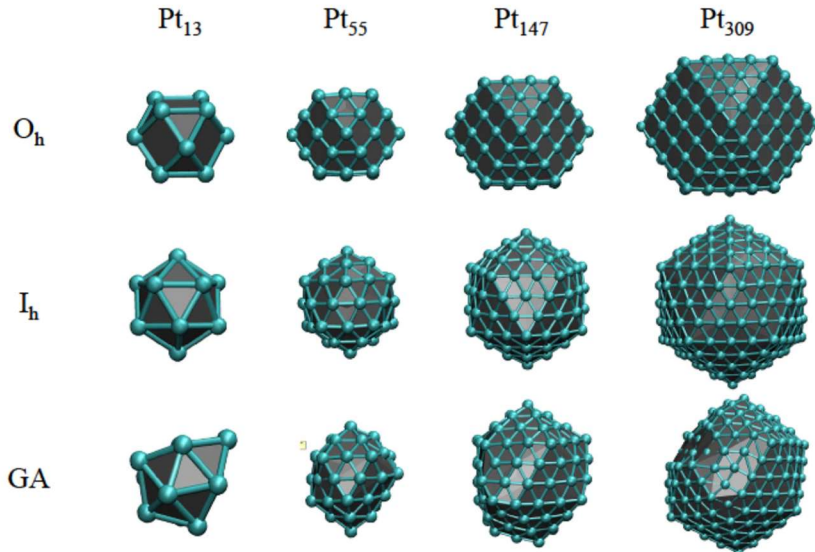


Figure 2.3. Geometries of low-energy “magic-number” Pt isomers in vacuum. The first two rows display high symmetry clusters cuboctahedral (O_h) and icosahedral (I_h) clusters. The third row displays minimum-energy structures found by the GA with an empirical potential.

2.3.2 Electronic Structure of Unsupported Pt Clusters

The d -band center energy of surface atoms is a widely employed and reliable descriptor for the adsorption energy of small molecules on transition-metal surfaces.¹¹³ In previous work we have also shown that the average d -band center energy of surface atoms on Pt_{13} nanoclusters can serve as a reasonable descriptor for the adsorption energies of methanol-decomposition intermediates and CO.^{59, 109, 142} Thus, we first examine the average d -band center energy of the surface atoms ($\overline{\epsilon_d^{sur}}$) for Pt_N ($N = 4-147$) clusters corresponding to particle diameters of 0.4-1.5 nm, to identify size-dependent trends as well as variations between low-symmetry and high-symmetry (I_h and O_h) morphologies.

From the angular-momentum-projected density of states, we compute the d -band center energy (ε_d) as

$$\varepsilon_d = \frac{\int \rho E dE}{\int \rho dE}, \quad (2.4)$$

where E is energy of each state and ρ is the corresponding density of d -states. Figure 2.4 displays the variation in $\overline{\varepsilon_d^{\text{sur}}}$ with cluster size for both GA-optimized, low-energy clusters as well as high-symmetry ones. For high symmetry clusters, $\overline{\varepsilon_d^{\text{sur}}}$ decreases rapidly with increasing cluster size, converging towards the bulk values for Pt (111) and (100) facets. This behavior can be rationalized by noting that the number of atoms on the (111) and (100) nanocrystal faces increases more rapidly than the number of atoms on (undercoordinated) edge or vertex sites with increasing crystal size, thus driving the average d -band position towards the bulk values. While the I_h clusters have only (111) facets and the O_h clusters display both (111) and (100) facets on the surface, $\overline{\varepsilon_d^{\text{sur}}}$ does not converge *precisely* to the bulk Pt(111) values for the former or to a weighted average for Pt(111) and (100) values for the latter, thus reflecting the as yet non-negligible contributions to the ensemble average from uncoordinated edge or vertex atoms that have relatively high d -band centers (Figure 2.5). The limiting bulk values should be recovered in the thermodynamic limit ($N \rightarrow \infty$). Irrespective of these details, the main point of note here is the monotonic decrease in $\overline{\varepsilon_d^{\text{sur}}}$ towards the limiting bulk values for high-symmetry (magic-number) clusters as a function of size. In contrast, the low-energy, low-symmetry, GA-optimized clusters consistently show lower $\overline{\varepsilon_d^{\text{sur}}}$ values than the high symmetry structures over the size range (4-147 atoms) considered here. Moreover, we observe that for clusters of size of 30 atoms large, $\overline{\varepsilon_d^{\text{sur}}}$ drops below the corresponding values for (111) and (100) facets reaching a

minimum value around $N = 100$. Beyond $N = 100$, there is a slight upshift in $\overline{\varepsilon}_d^{\text{sur}}$ but this remains below the values for (111) and (100) facets. While systematic modeling of clusters larger than 150 atoms is prohibitively expensive at this time, we attempted an additional test calculation (Table 2.4) for a larger Pt_{309} cluster and even in that case $\overline{\varepsilon}_d^{\text{sur}}$ remains about 0.1 eV below the Pt (111) value. The existence of a local minimum for $\overline{\varepsilon}_d^{\text{sur}}$ is particularly interesting as it suggests a preferred cluster size that might bind adsorbates more weakly and, for example, improve the resistance to CO poisoning. It should be noted though that the statistical errors in $\overline{\varepsilon}_d^{\text{sur}}$ for these low-symmetry clusters are large enough to suggest that this result is more suggestive of a size range (approximately 50-150 atoms) over which Pt nanoclusters bind adsorbates more weakly than macroscopic crystal facets.

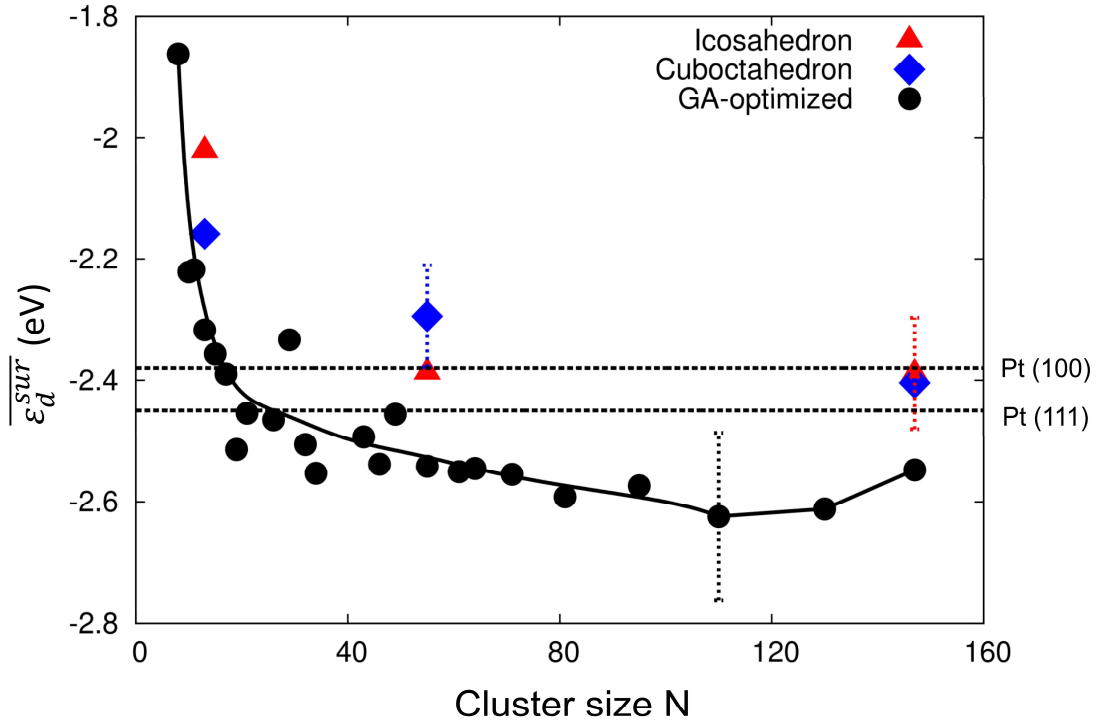


Figure 2.4. Average d -band center energy of the surface atoms, $\overline{\epsilon}_d^{\text{surf}}$, as a function of cluster size, N . The solid curve passing through data for GA-optimized structures is merely a guide to the eye. Error bars are standard deviations; representative error bars are shown only for certain sizes to maintain legibility. The exact values of d -band center energy with confidence intervals for every data point can be found in Table 2.4. Horizontal dashed lines indicate the reference d -band center energies on bulk-terminated, FCC Pt (111) and (100) surfaces.

While trends in d -band center energies are suggestive of lower adsorbate binding energies, they do not furnish definitive proof of such behavior. For sub-nanometer clusters, one can expect significant deformation of the cluster upon adsorbate binding and the magnitude of this effect could substantially alter conclusions based on relative d -band positions alone. Hence, we carry out DFT modeling of CO adsorption on Pt nanoclusters next to explicitly calculate CO adsorption energies as a function of cluster size and cluster morphology.

Table 2.4. Average d -band center energy of surface atoms, $\overline{\varepsilon_d^{\text{sur}}}$, and standard deviations, σ , as a function of cluster size, N .

N	GA-optimized		Icosahedron		Cuboctahedron	
	$\overline{\varepsilon_d^{\text{sur}}}$	σ	$\overline{\varepsilon_d^{\text{sur}}}$	σ	$\overline{\varepsilon_d^{\text{sur}}}$	σ
8	-1.86	0.14				
10	-2.22	0.38				
11	-2.22	0.36				
13	-2.32	0.27	-2.02	0.09	-2.16	—
15	-2.36	0.17				
17	-2.39	0.27				
19	-2.51	0.26				
21	-2.45	0.13				
26	-2.46	0.22				
29	-2.33	0.24				
32	-2.51	0.19				
34	-2.55	0.21				
43	-2.49	0.17				
46	-2.54	0.15				
49	-2.46	0.13				
55	-2.54	0.21	-2.39	0.11	-2.29	0.08
61	-2.55	0.15				
64	-2.55	0.13				
71	-2.55	0.11				
81	-2.59	0.16				
95	-2.57	0.15				
110	-2.62	0.14				
130	-2.61	0.17				
147	-2.55	0.15	-2.39	0.09	-2.40	0.08
309	-2.54	0.10	-2.38	0.10	-2.45	0.10

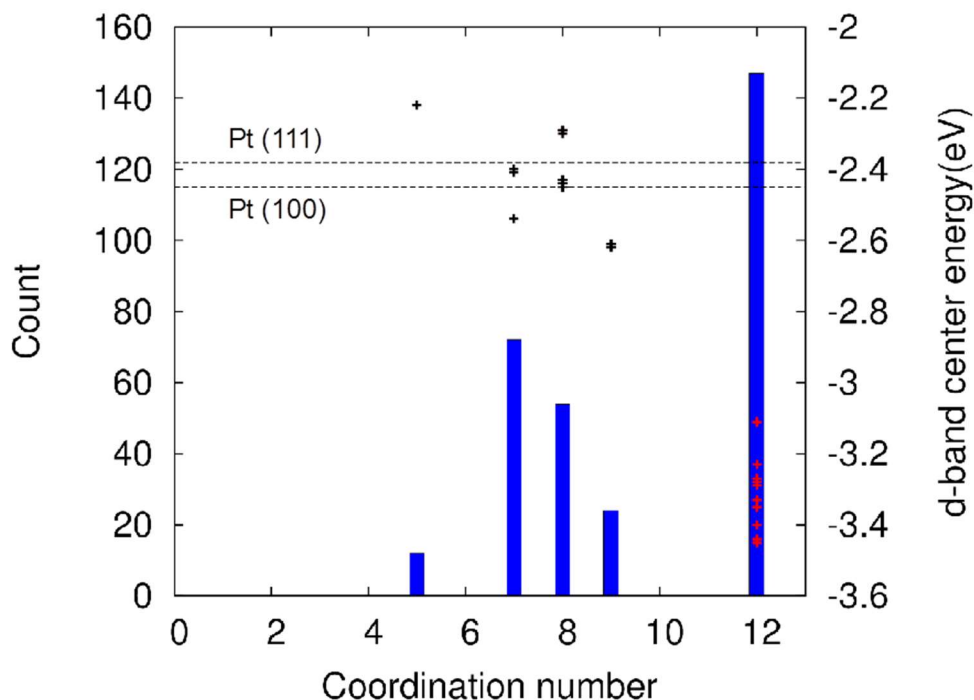


Figure 2.5. Distribution of coordination numbers (blue bars) as well as d -band center energies of atoms on the surface (black “+” symbols) and in the bulk (red “+” symbols) for the cuboctahedral Pt_{309} cluster. Surface d -band centers of FCC Pt (111) and Pt (100) surfaces are shown for reference.

2.3.3 Cluster-Size-Dependent CO Adsorption Energies and Their Correlation with d -band Center Energies

We sampled single-molecule CO adsorption energies across a wide range of GA-optimized Pt_N ($N = 4\text{--}147$) clusters considering approximately 200 adsorption sites in total that span the full range of both coordination number and site-specific d -band centers that the surfaces offer. High-symmetry I_h and O_h structures were also studied for comparison against their low-symmetry counterparts as these structures are often used as models for catalyst clusters. CO adsorption on Pt nanoclusters was calculated via DFT modeling by Raymond Gasper. Detailed results and analysis can be found in Ref. ¹⁴³; a summary of the main conclusions of these studies is as follows:

1. We find that with increasing cluster size, the CO adsorption energies monotonically approach the values for bulk surfaces, whereas the GA-optimized Pt clusters show the presence of a local maximum in the CO adsorption energy at a cluster size of $N = 55$, for which the CO adsorption energy is almost equal, within statistical error, to that of the Pt (111) surface.
2. In the sub-nanometer range, the low-symmetry Pt nanoclusters bind CO more weakly than the high-symmetry ones. The differences in CO binding energies on low- and high-symmetry structures are non-negligible, ranging from 0.1-1.0 eV, thereby justifying the need for proper optimization of cluster morphology via global minimization techniques as opposed to *ad hoc* choices of structures.

2.3.4 Prediction of CO Adsorption Energies via Machine Learning

Gaspar showed that the optimal cluster size for low CO binding, $N \approx 55$, does not coincide with the minimum in the average surface d -band center at $N \approx 100$ that we see in Figure 2.4. The coordination number of surface atoms, another potential descriptor, grows monotonically with size and approaches that for the low-energy facets,¹⁹ and hence cannot by itself capture the local maximum in the adsorption energy curve. These problems in arriving at a single-descriptor based model are magnified even further if one attempts to consider site-specific adsorption energies¹³ rather than surface averages. Hence, we turn next to more systematic approaches based on machine-learning algorithms that can help us arrive at robust multi-descriptor models.

Having established that single-descriptor models are of limited use in accurately predicting CO adsorption energies, we resort to the application of machine-learning (ML)

tools in the search for suitable multi-descriptor models. Specifically, we employ the gradient-boosting regression (GBR) algorithm as implemented in the scikit-learn python package.¹¹⁰⁻¹¹¹ The GBR model was used recently by Takigawa *et al.* and shown to be accurate in predicting the *d*-band center energies of crystal surfaces for various bimetallic alloys using readily available mechanical properties of the metals.¹¹⁶ The GBR is superior to a simple linear regression when working with nonlinear data relationships such as are seen between *d*-band center and CO adsorption energy on the nanoparticles under examination in this work.

To train the ML (Machine Learning) algorithm and access the accuracy of ML predictions, CO adsorption energies on different surface sites of Pt clusters, including both GA clusters and high symmetry clusters, were used as target data. A few low-(but not minimum-) energy clusters that were produced by the GA in some of the early generations were also sampled to explore a wider descriptor and target space. In total, 195 sites were sampled for CO adsorption, 75% of which were used for training and the remaining 25% for testing. To reduce bias in data partitioning, we used stratified six-fold validation, wherein the CO adsorption data for each cluster were randomly split into six different train–test sets, which are constructed to ensure that every data point is in a test set at least once.

Descriptors associated with each adsorption site that are used for the prediction of adsorption energy are broadly grouped into three types, in order of increasing computational effort:

- i. *Type 1 descriptors* involve only the electronic structure information calculated from DFT for each adsorption site. One of the most widely used descriptors of this type is the *d*-

band center energy ε_d^i defined here for a specific adsorption site i . Here, we use a slightly modified version, namely, the generalized d -band center energy $g\varepsilon_d^i$, following the concept of generalized coordination number, defined as

$$g\varepsilon_d^i = (\sum_{j \in nn} \varepsilon_d^j) / cn_i, \quad (2.5)$$

which is in essence a local average of the atomic d -band centers. cn_i is the coordination number of atom i , and the sum runs over all nearest neighbors j of site i . While either the usual site-specific d -band center energy or the generalized version can be used with little difference in the quality of the regression analysis for our present purposes (on-top binding), the latter is a more intuitive and convenient definition for further extensions to bridge or hollow binding sites that are not specifically associated with a single atom. Other Type 1 descriptors that were tested in the primary analysis also include s -band and p -band centers, electronic bandwidths, and Bader charges³⁷ of adsorption sites. Several of these were either highly correlated with the d -band properties or led to no further improvement in the testing errors. Hence, we work with the generalized d -band center energy as the sole Type 1 descriptor for now.

i. *Type 2 descriptors* involve only structural information of bare clusters, including average nearest-neighbor bond length \bar{d}_{Pt-Pt}^i , generalized coordination number gcn^i , and cluster radius of gyration R_g . The average bond length for a Pt atom i is calculated as

$$\bar{d}_{Pt-Pt}^i = \sum_{j \in nn} d_{ij} / cn_i, \quad (2.6)$$

where d_{ij} is the distance between an atom i and its nearest neighbors j , and cn_i is the coordination number of atom i . The general coordination number gcn^i defined as

$$gcn^i = \sum_{j \in nn} cn^j / cn_{bulk}, \quad (2.7)$$

is generally a better descriptor for adsorption energy than coordination number as has been shown for several small molecules on metal nanoparticle surfaces.¹⁰⁵ cn_{bulk} is the coordination number of a Pt atom in the bulk FCC phase. The radius of gyration R_g is a cluster property, and is the same for all sites on a cluster. These three descriptors thus quantify local, non-local, and global structural properties associated with the CO adsorption process. All these descriptors are readily calculated from the optimized cluster structure.

ii. *Type 3 descriptors* include for now a single descriptor that encapsulates both electronic and structural information of the adsorption site, namely, the fully-frozen CO adsorption energy E_{ads}^{AF} . As the Pt cluster (that has already been previously relaxed) and the CO molecule do not undergo any further ionic relaxation in this calculation, E_{ads}^{AF} can be obtained roughly two orders of magnitude faster than E_{ads}^{AR} . It is also clear from Figure 2.3 that E_{ads}^{AF} closely tracks the size-dependent trends of the target values of E_{ads}^{AR} thus making it a sensible choice of descriptor.

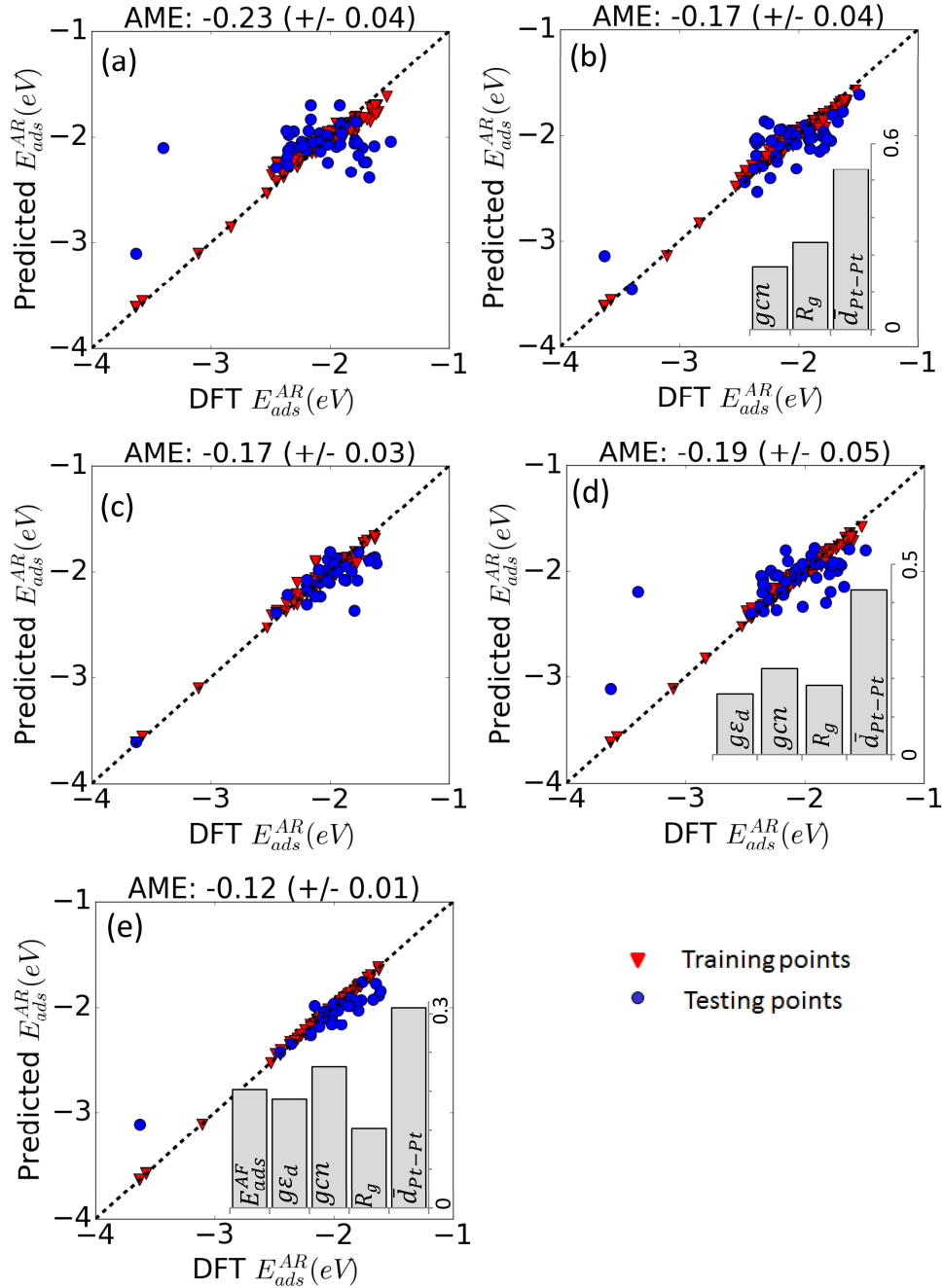


Figure 2.6. DFT-calculated CO adsorption energies on the surface sites of Pt clusters versus the prediction from GBR model with different sets of descriptors: (a) Generalized d -band center, (b) Type 2 descriptors, (c) E_{ads}^{AF} alone, (d) Generalized d -band center and Type 2 descriptors (e) all three descriptor types (5 descriptors total). Reported AME (absolute mean error) of the model predictions are the average over six-fold cross validation to avoiding splitting bias. The displayed data points are from one such randomly split dataset. Insets in (b), (d) and (e) show the relative importances of the descriptors in the models.

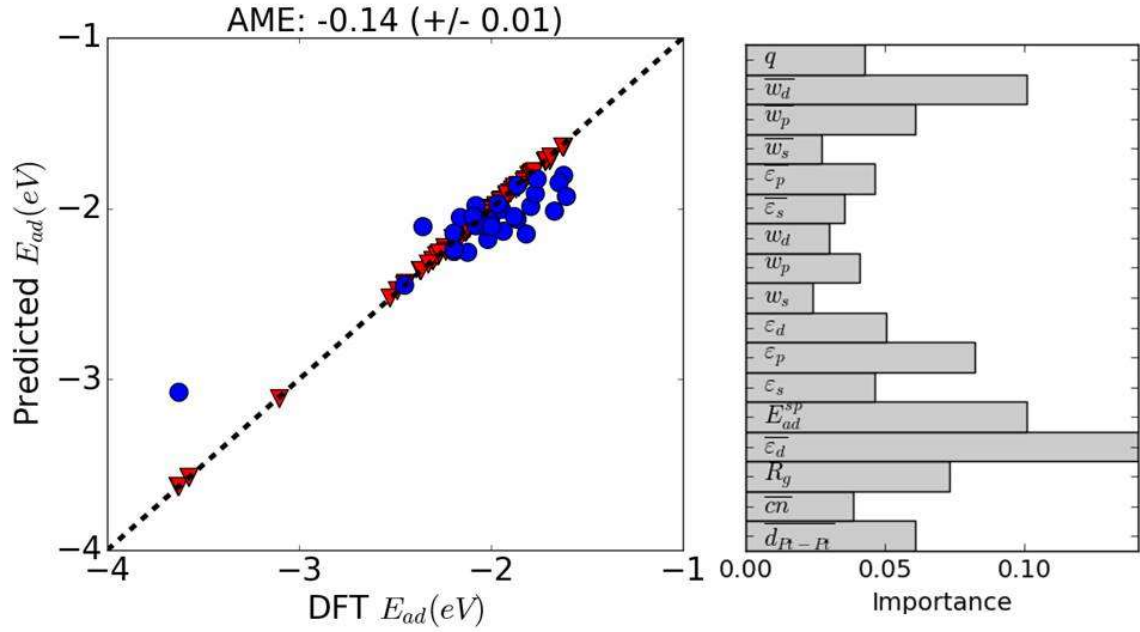


Figure 2.7: DFT-calculated CO adsorption energies on the surface sites of Pt clusters versus the prediction from GBR model with all descriptors. Below is a list of the descriptors used for this figure:

- q valence electrons associated with each atom (from Bader analysis)
- $\overline{w_d}$ general d -band width
- $\overline{w_p}$ general p -band width
- $\overline{w_s}$ general s -band width
- w_d d -band width
- w_p p -band width
- w_s s -band width
- $\overline{\epsilon_d}$ general d -band center energy with respect to the Fermi level
- $\overline{\epsilon_p}$ general p -band center energy with respect to the Fermi level
- $\overline{\epsilon_s}$ general s -band center energy with respect to the Fermi level
- ϵ_d d -band center energy with respect to the Fermi level
- ϵ_p p -band center energy with respect to the Fermi level
- ϵ_s s -band center energy with respect to the Fermi level

The remaining descriptors are explained in Section 3.3 of the paper.

The descriptors chosen here are by no means unique and other choices are equally reasonable. For now, we proceed with the above three classes and analyze their utility in predicting site-dependent CO adsorption energies.

Figure 2.6 displays the correlation between DFT-calculated and ML-predicted CO adsorption energies (site-specific and not cluster average) using different combinations of descriptors. When trained by Type 1 descriptors (the generalized d -band center energy) alone, the model shows an absolute mean error (AME) of -0.22 eV in the test sets [Figure 2.6 (a)]. It is evident that there are a large number of outliers in the training set and this is exacerbated for the testing set. Similarly, using purely structural information [Type 2 descriptors; Figure 2.6 (b) or only E_{ads}^{AF} [Type 3 descriptors; Figure 2.6 (c)] both result in AMEs of 0.17. In short, using just one class of descriptors is rather unsatisfactory in predicting the CO adsorption energies. A combination of electronic structure and structural information results only in a slightly improved AME [Figure 2.6 (d)]. By combining all descriptor classes though, the AME can be substantially reduced to 0.12 eV [Figure 2.6 (e)]. This error is of the same order as that reported recently by Xin and coworkers in ML predictions of adsorption of CO on a wide variety of pure transition metal and alloy surfaces.¹¹⁴⁻¹¹⁵ Importantly, visual inspection of Figure 2.6 (e) shows that the CO adsorption data is predicted quite accurately across a broad energy window of ~ 4 eV. The inset bar display the importances of the various descriptors in the final prediction. Focusing on the full descriptor set in Figure 2.6 (e), we see that the (generalized) d -band center, average Pt-Pt bond length, and (generalized) coordination number – conventional descriptors based on sound fundamental insights – are still indispensable, as reconfirmed by the ML algorithm. When focusing on sub-nanometer clusters, physical intuition suggests that size effects (quantified by R_g) ought to become relevant for cluster deformation; this is confirmed by the ML algorithm. Similarly, we expect that the inclusion of E_{ads}^{AF} as a descriptor incorporates some of the fundamental electronic processes during

CO chemisorption that are difficult to capture by simple electronic structure information alone (*d*-band positions and/or widths) thereby significantly improving the predictive capability of the ML algorithm. For completeness, we also tested models with numerous other descriptors and found little to no improvement over the smaller, physically motivated subset of descriptors employed here. In summary then, by combining modern computational tools with traditional physical insights, we are now able to implement accurate, inexpensive, and robust predictive models that can help push the frontier of rational catalyst design beyond macroscopic crystal surfaces to low-symmetry nanoscale catalysts.

2.4 Conclusions

We studied Pt nanoclusters, ranging from 0.2–1.5 nm in diameter, to understand size-dependent trends in the energetics of CO binding, and to correlate these with morphological and electronic descriptors. An important aspect of our approach was to employ a GA to determine unambiguously the low-energy morphologies of the Pt nanoclusters, which uniformly adopt low-symmetry structures for the sizes considered here. GA-optimized clusters show a non-monotonic trend of surface *d*-band centers with respect to size, going from very high values at small sizes to a minimum around Pt₁₀₀, before slowly asymptoting towards the Pt (111) surface value. This is in clear contrast to the essentially monotonic behavior of high-symmetry, cuboctahedral and icosahedral morphologies, which are not true low-energy structures for sub-nanometer Pt clusters. The CO adsorption behavior on GA-optimized clusters also presents similar non-monotonic behavior with a global maximum at around Pt₅₅.

By employing machine learning algorithms, we showed that the non-monotonic trends in CO adsorption energies are not accurately captured by traditional single descriptor models based on *d*-band center energies or coordination number. Multi-descriptor models based on *d*-band centers and structural information (coordination number, bond lengths, cluster size) do not perform much better either. By adding a new descriptor to our models, namely, the “all-frozen” adsorption energy (E_{ads}^{AF}), which partially incorporates some of the features of CO-Pt bond formation, we were able to achieve significant improvement in the machine-learning model. We suggest that this descriptor, E_{ads}^{AF} , which can be calculated at minimal computational overhead, might be broadly applied across other systems to predict site-specific adsorption energies with higher accuracy; studies along these lines will be pursued elsewhere.

Overall, our work demonstrates the potential for developing accurate, predictive models of adsorbate binding on realistic nanocluster morphologies by integrating robust structural optimization methods with machine learning algorithms. Progress along these lines can significantly aid rational design of nanoscale catalysts, particularly in the sub-nanometer range where both structural and electronic properties differ fundamentally from those at larger length scales.

CHAPTER 3

STABILITY, ENERGETICS, AND CATALYTIC PROPERTIES OF GRAPHENE-SUPPORTED PT CLUSTERS

3.1 Introduction

Typically, industrial Pt electrocatalysts are prepared by dispersing Pt powders as small as a few nanometers on conductive carbon black supports,¹⁴⁴ which results in a high electrocatalytically active surface area. However, it is well known that traditional Pt/C catalysts are easily poisoned by intermediates, most notably CO, produced during the methanol oxidation reaction at the cathode.^{43-44, 145} In addition, these Pt/C systems suffer from poor long-term stability arising from the corrosion of the carbon support and dissolution or aggregation of Pt on the support surface.^{33, 60, 146-147} Graphene has been shown to be an excellent support for transition-metal-based electrocatalysts, impacting many of the issues above through its strong interactions with a broad range of materials,¹⁴⁸ high electronic conductivity,¹⁴⁹ and potential for beneficial modification of the electrochemical properties of supported clusters.¹⁵⁰ However, Pt/graphene nanostructures remain poorly understood, making it challenging to optimize these electrocatalytic systems. In this article, we apply advanced optimization methods with force fields benchmarked by first principles theory to gain insights into Pt/graphene geometrical and electronic structures.

It is well accepted that the structure of catalyst particles plays a significant role in their catalytic performance¹⁵¹⁻¹⁵² and achieving a detailed understanding of structure–activity relationships is hence, an issue of much current interest. For example, in recent work Fampiou and Ramasubramaniam⁶ investigated the thermodynamic and electronic properties of Pt₁₃ isomers on graphene supports by examining both high-symmetry cluster

morphologies as well as low-symmetry ones (derived from molecular dynamics annealing). They observed appreciable differences with respect to cluster binding energies on the support, cluster *d*-band centers, adsorbate binding energies, and overall charge redistribution with different cluster morphologies (isomers). While those studies were limited to a relatively small set of candidate structures, they nevertheless established the need for careful initial selection of cluster morphologies prior to subsequent studies of catalytic reactions on clusters. Indeed, for computational studies of cluster catalysis, it is reasonable to invest initial effort in ascertaining thermodynamically (or kinetically) favored structures, as these are the most probable structures under experimental conditions.¹⁵³ While ground-state cluster morphologies might, in principle, be gleaned from experiments, e.g., via fluorescence spectroscopy techniques for vacuum Pt clusters,¹⁵⁴⁻¹⁵⁵ such studies are extremely challenging and hence, limited in number and scope. In contrast, computational studies of the energetics of Pt clusters in vacuum, using both quantum mechanics and empirical potential modeling, are more extensive.^{44, 137, 141, 156-160} However, to the best of our knowledge, there are as yet no systematic investigations of the ground-state energetics and morphologies of Pt clusters on graphene supports. In other words, the influence of Pt–graphene binding interactions on cluster morphology and the resulting effects on cluster activity still remain to be systematically understood.

The primary goal of this chapter is to present a robust methodology for identifying thermodynamically favorable structures of Pt clusters on graphene supports and to draw clear correlations between cluster energetics and catalytically relevant metrics such as the *d*-band center and Pt cluster charge transfer. The high-dimensional potential energy surface (PES) for the Pt/graphene system is extremely complex and a brute force search for energy

minima at the first principles level is computationally infeasible. Therefore, we carefully test and validate a Pt–C empirical potential, which we then employ within a GA¹⁶¹⁻¹⁶³ to facilitate rapid and thorough identification of minimum energy Pt_N ($N = 2-80$) clusters on defect-free and defective graphene supports. Optimized structures are then studied more thoroughly with DFT calculations to test the structural accuracy and energetic ordering of the empirical potential predictions. Finally, ensembles of supported near-minimum energy Pt₁₃ isomers are subjected to detailed electronic structure analyses via DFT calculations to identify clearly the role of support defects and cluster energetics on the potential catalytic activity of the Pt clusters. Overall, by combining an inexpensive empirical potential-based GA with *ab initio* calculations, we establish a tractable approach for systematic exploration of supported clusters at system sizes that are experimentally relevant and yet inordinately expensive for brute force *ab initio* calculation alone.

3.2 Computational Methods

3.2.1 GA for Supported Clusters

Following the methodology in Chapter 2, we will first explore the stable structures of Pt clusters supported on graphene. The approach followed here for optimization of supported clusters follows the spirit of the pioneering work of Ho and coworkers¹²⁷. Details of the GA implementation for unsupported nanoclusters have been described in Chapter 2 and we will only discuss the additional modifications to the GA when the graphene support is present. During the mating process, only the metal parts of the two parent candidates were sliced and glued together to form a new metal cluster, which is then positioned appropriately relative to the graphene sheet to form the child candidate. From numerical

testing, a minimum cluster–support distance of 2 Å was found to be a good initial guess for rapid convergence.

3.2.2 Empirical Potential Models for Graphene Supported Pt clusters

In Chapter 2, we employed a Pt interatomic potential developed by Albe et al.¹²⁸ based on the reactive bond-order Tersoff-Brenner form.¹²⁹ In addition to Pt-Pt interactions, Albe et al.’s potential also incorporates C-C and Pt-C interactions, which makes it ideally suited for describing Pt clusters on carbon supports. Fampiou and Ramasubramaniam⁶⁰ showed that the potential of Albe et al. is remarkably accurate relative to DFT in describing supported cluster morphologies, albeit with limited sampling. Here, we carry out a more extensive investigation of the fidelity of this potential for unsupported clusters, and show that this potential is generally in very good agreement with DFT structural models. We also perform careful tests of Albe et al.’s potential for supported clusters and demonstrate that the potential is indeed capable of delivering accurate low-energy structures for further electronic structure analyses. All empirical potential simulations are performed using the LAMMPS simulation package.

3.2.3 Global Optimization for Supported Clusters

We performed GA optimization of Pt_N ($N = 2\text{--}80$) clusters on defect-free (pristine) and defective (vacancy and divacancy defects) graphene supports using Albe et al.’s potential. In all supported cluster calculations, we used an 8×8 graphene super-cell (128 C atoms in pristine graphene), as shown in Figure 3.1, which is sufficiently large to eliminate long-ranged interactions between Pt_{80} clusters (the largest clusters studied here). From the converged GA results, various structural properties of clusters such as the radius of

gyration, coordination numbers, and average bond lengths were calculated.

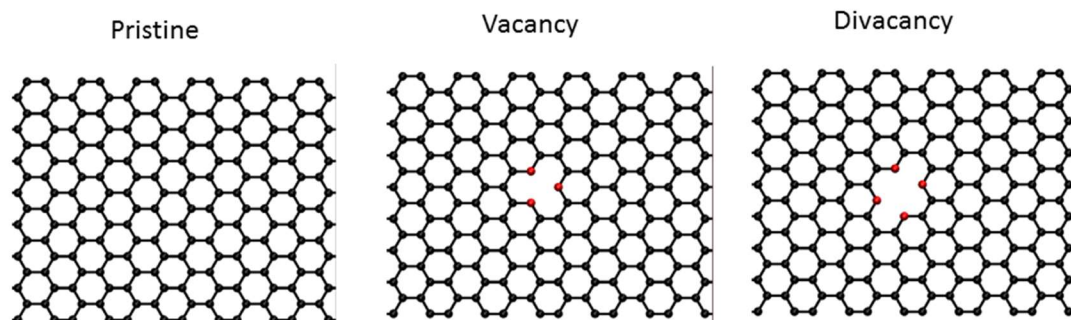


Figure 3.1. Defect-free and defective graphene substrates employed in this study

3.2.4 DFT Calculations

DFT calculations were performed to study the thermodynamic and electronic properties of selected low-energy structures using VASP. Core and valence electrons were described using the Projected Augmented Wave method. The PBE form of the generalized-gradient approximation was employed to describe electron exchange and correlation. A kinetic energy cutoff of 400 eV was used for the plane-wave basis set and the conjugate gradient algorithm was used to relax ions into their ground state until the force on any atom is smaller than 0.01 eV/Å. For supported clusters (128 C atoms in pristine support), a $2 \times 2 \times 1$ Γ -centered k -point mesh was sufficient to converge total energies to within 0.5 meV per graphene atom.

3.3 Result and Discussion

3.3.1 Structure and Energetics of Supported Pt Clusters

We now consider the energetics of Pt_N clusters on graphene supports. Point defects in graphene are known to act as strong anchoring sites for nanoclusters and have also been shown to modify the electronic structure and catalytic activity of small clusters.⁵⁸⁻⁶⁰ The metrics we adopt for thermodynamic comparisons are the cluster adsorption energy and the overall formation energy of the composite Pt/graphene system. The adsorption energy (E_{ad}) is defined as

$$E_{ad} = E_{Pt_N+Gr} - E_{Pt_N} - E_{Gr} , \quad (3.1)$$

where E_{Pt_N+Gr} is the total energy of the Pt/graphene system, E_{Pt_N} is the total energy of the Pt_N cluster without the support, and E_{Gr} is the total energy of the (pristine/defective) graphene sheet. The overall formation energy of the composite Pt/graphene system (E_f) is defined as

$$E_f = E_{Pt_N+Gr} - M \times E_C - N \times E_{Pt} , \quad (3.2)$$

where E_{Pt_N+Gr} is the total energy of the Pt/graphene system, E_{Pt} is the energy of an isolated Pt atom in vacuum, E_C is the energy of a single C atom in graphene, and M and N are the number of C and Pt atoms, respectively.

Table 3.1. Formation energies (eV) of minimum-energy Pt clusters on pristine and defective (vacancy, divacancy) graphene supports identified using the GA and by molecular-dynamics-based annealing (Ref. ⁶⁰)

	Pristine		Vacancy		Divacancy	
	GA	annealing	GA	annealing	GA	annealing
Pt₂	-5.75	-5.62	-5.33	-5.30	-5.59	-5.25
Pt₃	-10.11	-10.06	-9.55	-8.73	-9.88	-8.38
Pt₄	-14.24	-13.12	-13.80	-11.69	-14.13	-13.80
Pt₁₃	-55.50	-55.20	-55.16	-55.14	-55.65	-55.67

Table 3.2. Formation energies (eV) of minimum-energy Pt clusters on pristine and defective (vacancy, divacancy) graphene supports identified using GA.

	Pristine		Vacancy		Divacancy	
	Tersoff	DFT	Tersoff	DFT	Tersoff	DFT
Pt₂	-5.75	-1.34	-5.33	-0.68	-5.59	1.37
Pt₃	-10.11	-5.20	-9.55	-3.50	-9.88	-3.38
Pt₄	-14.24	-9.11	-13.80	-5.33	-14.13	-7.10
Pt₁₃	-55.50	-45.94	-55.16	-41.56	-55.65	-41.73

First, to test the performance of our GA, we study supported Pt_N ($N = 2, 3, 4, 13$) clusters and compare our results with those of Fampiou and Ramasubramaniam⁶⁰ who also used Albe et al.’s bond-order potential but adopted a molecular dynamics (MD) annealing scheme for energy minimization. The formation energies for Pt_N ($N = 2, 3, 4, 13$) clusters with pristine and defective graphene supports are reported in Table 3.1, and the corresponding structures (from the GA) are displayed in Figure 3.2. For additional comparison, we also report formation energies calculated using the empirical potential and by DFT in the Table 3.2. In all cases, the GA delivers structures with lower formation energies than the MD annealing results previously reported. The differences are particularly noticeable for few-atom clusters. In the Pt₂ case, the GA produces ground states consisting of dimer orientations parallel to the surface on pristine and defective graphene supports. MD-based annealing consistently generates local minima with vertically oriented Pt dimers on pristine graphene; on defective graphene, the dimers lie parallel to the support.

For Pt₃ clusters on pristine graphene, both GA and MD annealing find the vertical triangle as the ground state; on defective graphene, the GA finds structures that are appreciably more stable by (1.0-1.5 eV) than those from MD annealing. For Pt₄ clusters, the GA finds a planar cluster that is nearly vertically oriented to the pristine graphene sheet as the minimum energy structure; a tetrahedron is the most stable structure on defective graphene supports. The MD annealing algorithm is again stuck in various local minima at higher energies. Finally, for Pt₁₃ clusters on graphene supports, Fampiou and Ramasubramaniam showed that the clusters prefer more open structures instead of high-symmetry ones (I_h or O_h); the GA results confirm those findings and the minimum energy structures are also energetically very close to those found by MD annealing. It thus appears that clusters with very small number of atoms present pathological challenges for the MD annealing procedure, in particular, capturing the precise orientation and location of cluster atoms on the support. With increasing cluster sizes, the energetics appear to be dominated by the inherent morphology of the cluster itself, with orientational effects relative to the support being of lesser importance. In any case, it is clear that a global minimization algorithm, such as a GA, performs more reliably at finding ground states than ad hoc procedures such as simulated annealing.

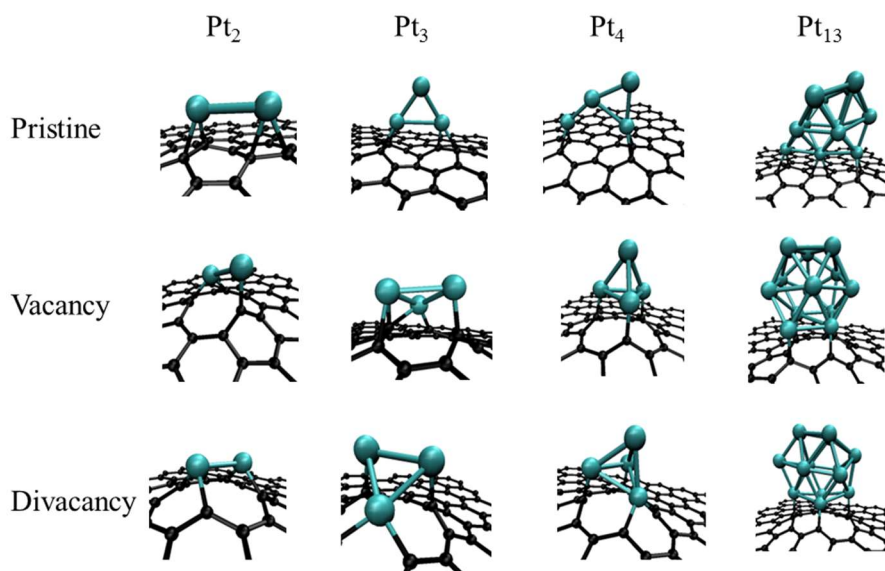


Figure 3.2. Minimum-energy structures of Pt_N ($N = 2, 3, 4, 13$) on pristine graphene (upper row), and graphene with single vacancy (middle row) and divacancy defects (bottom row).

Next, we study the properties of supported Pt_N clusters over the size range $N = 2$ -80 analogous to the unsupported cluster studies. In addition to thermodynamic properties such as adsorption and formation energies, we also thoroughly characterize the structural properties of clusters through metrics such as the radius of gyration, average coordination number, average bond lengths, and fraction of (potentially) catalytically active surface atoms, which are variously displayed in Figure 3.3. Note that while the catalytic activity of a site on a crystalline facet (terrace, step, edge, kink) or on a large nanoparticle (face, edge, corner) can vary significantly due to local coordination, the nanoclusters considered here are too small to display such distinguishing morphological features. Thus, we focus on understanding average properties of surface sites throughout this work. The various configurations studied here are all minimum-energy structures obtained via the GA.

Figure 3.3 (a) displays the radius of gyration (R_g) of Pt_N clusters with and without the graphene support. As seen, R_g tends to be noticeably higher for unsupported clusters and clusters on pristine graphene supports relative to those on defective supports up to $N = 12$. This is due to 2D morphologies being preferable both in vacuum as well as on pristine graphene supports at these cluster sizes; the presence of point defects in the graphene support favors 3D structures beginning from the smallest possible size, Pt_4 , as seen in Figure 3.3. For $N \geq 13$, the support effect on cluster morphology is negligible— R_g is approximately the same for supported as well as unsupported clusters. Physically, this result suggests that the Pt–C contribution to the total energy becomes less important compared with the Pt–Pt interaction for larger clusters.

Another important structural metric used to characterize clusters is the atomic coordination number; Figure 3.3 (b) displays the average coordination number (Z_{avg}) of Pt atoms as a function of cluster size. The precise number of neighbors of an atom is sensitive to the cutoff distance chosen for bond counting and, for consistency, we use the same cutoff distance as that for Pt–Pt interactions in the bond-order potential (3.3 Å). As seen from Figure 3.3 (b), the average coordination number increases monotonically with cluster size, as is to be expected due to the increase in the bulk-to-surface ratio. For the range of clusters studied here, $Z_{avg} = 8$ is the largest value attained; for reference, we recall that the coordination number of atoms on the Pt (111) surface is nine while that in the bulk is 12. This significant overall degree of undercoordination is to be expected for such small clusters that are mostly “surface” rather than “bulk”. Our calculations show that the smallest cluster size for which at least one atom has a coordination number of 12 is $N = 19$.

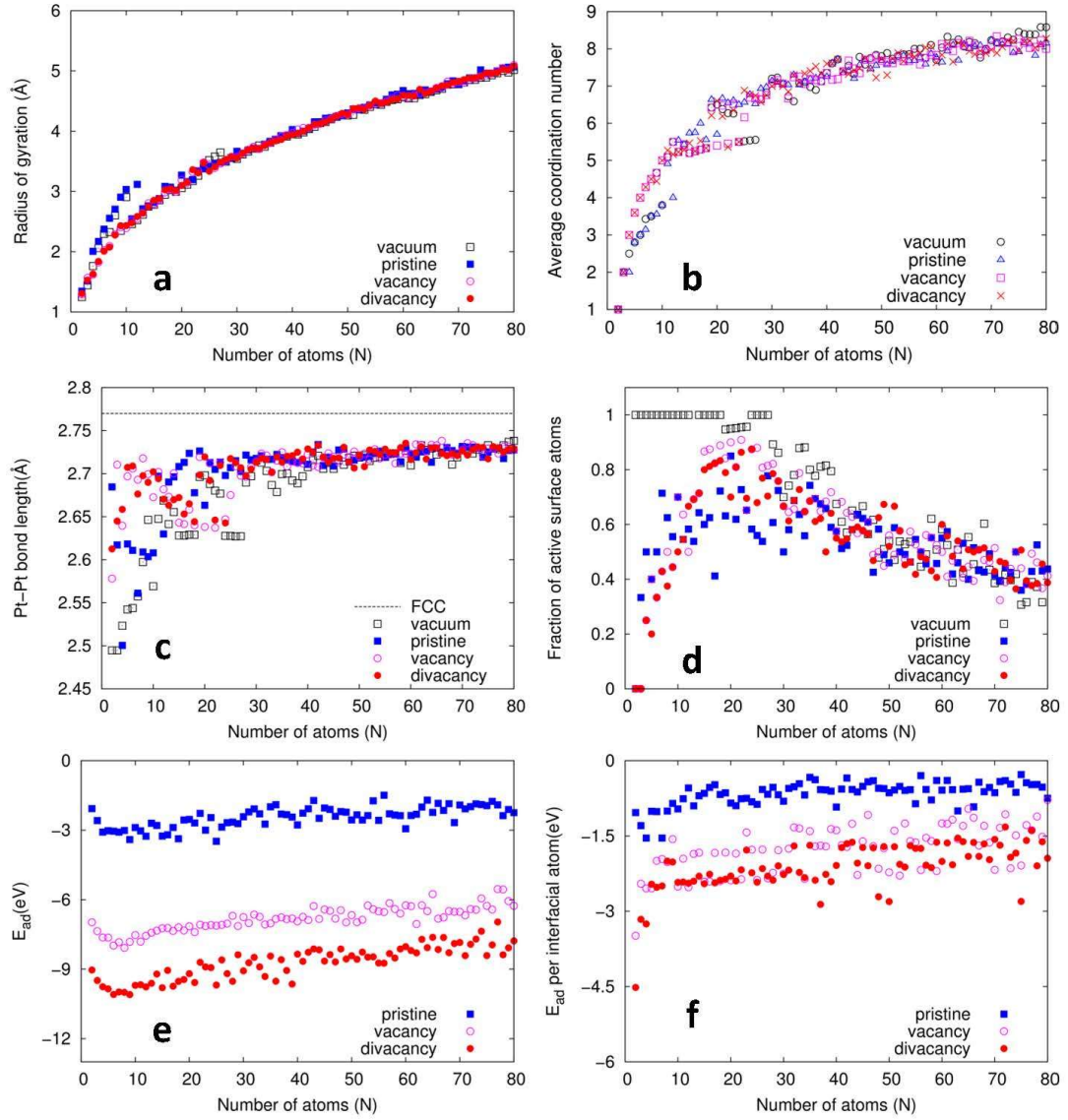


Figure 3.3. Evolution of structural and energetic properties of global minima of $Pt_N/graphene$ calculated using the GA as a function of particle number N : (a) radius of gyration; (b) average coordination number of Pt atoms (excluding Pt-C bonds); (c) average Pt-Pt bond length (dashed line is for bulk FCC Pt); (d) fraction of active surface atoms, defined in equation 3.3; (e) adsorption energy (E_{ad}) of Pt clusters on graphene; (f) average contribution of Pt atoms at the Pt-C interface to E_{ad} .

Figure 3.3 (c) offers insight complementary to this analysis of coordination numbers by displaying the average Pt-Pt bond length (a_{avg}) in the unsupported and

supported Pt clusters; the horizontal dashed line in that figure indicates the bulk, FCC Pt–Pt bond length (2.77 Å) for comparison. The average Pt–Pt bond decreases in length with decreasing cluster size, which once again reflects the increase in the ratio of surface to bulk atoms as under-coordinated surface atoms exhibit shorter bonds to compensate for having fewer neighbors. The trends for a_{avg} are similar for unsupported clusters and for those on pristine graphene supports, especially at small cluster sizes, reflecting the relatively small role of the support in the absence of strong perturbations such as those arising from point defects. Again, for larger clusters, the differences in a_{avg} are small, thus reflecting the relatively minor role of the support on cluster morphology. For the range of cluster sizes studied here, a_{avg} is still about 0.1 Å smaller than the bulk FCC value. There are some systematic deviations in the monotonic growth of Z_{avg} and a_{avg} in the $N = 20$ -40 as seen from Figure 3.3 (b, c). Closer visual inspection of these clusters leads us to attribute the fluctuations to a competition between hollow-core and filled-center cluster morphologies.

A structural property of interest and immediate relevance to cluster catalysis is the number of potentially active Pt atoms on the cluster surface. Atoms within the interior of the cluster do not directly participate in surface reactions and we also assume that atoms directly bonded to the support are less likely to participate in surface reactions due to constraints arising from, e.g., steric hindrance and possibly from electronic effects (saturation of dangling bonds). There are of course exceptions to such criteria, notably for single-site catalysts bound at point defects in graphene,¹⁶⁴⁻¹⁶⁵ but these are essentially pathological cases and the proposed criterion is both intuitively appealing and physically reasonable for larger clusters. Thus, we define the fraction of active surface atoms ($f_{\text{Pt}}^{\text{surf}}$) as

$$f_{Pt}^{surf} = (N_{Pt}^{surf} - N_{Pt}^C) / N_{Pt} , \quad (3.3)$$

where N_{Pt}^{surf} is the number of atoms on the surface of the Pt cluster, and N_{Pt}^C is the number of Pt atoms bonded to the support. Various criteria may be established for identifying a “surface” atom; we do so here by assigning an atom with six or fewer neighbors to be a surface atom. Visual inspection of several clusters confirms the validity of this coordination number cutoff. As seen from Figure 4 (d), f_{Pt}^{surf} displays rather interesting behavior. For unsupported clusters all atoms are on the surface for $N < 19$; for larger unsupported clusters, most of the Pt atoms are in the bulk and consequently are not active. For supported clusters, the fraction of active sites is initially small as many Pt atoms are bonded directly to the graphene support; at large cluster sizes, most of the Pt atoms are again in the bulk and are consequently not active. The optimal value for f_{Pt}^{surf} is achieved in the range $N = 20-30$ irrespective of the presence or absence of the support defects. This is a key result as it identifies an optimal range of cluster sizes that maximally utilizes the precious metal catalyst; to the best of our knowledge, this result has not been reported before and, in particular, not for supported Pt clusters.

Finally, Figure 3.3 (e) and Figure 3.3 (f) display the total adsorption energy and adsorption energy per interfacial Pt atom for supported Pt_N clusters. It is clear that point defects in the graphene support bind Pt clusters more strongly than does pristine graphene across the entire range of cluster sizes; divacancies are also seen to be stronger binding sites than vacancies due to a higher number of dangling bonds. In general, the variation in adsorption energies with cluster size is rather small; similar results were reported by Ramos-Sanchez et al.,¹⁶⁶ who used DFT calculations to study clusters on graphite in the

range of $N = 1-38$. The slight decrease in binding strength (less negative adsorption energies) with increasing cluster sizes (beyond $N = 10$) is indicative of weaker trapping of larger clusters by the vacancy/divacancy, thus suggesting the need for larger support defects to improve the stability of larger Pt clusters against aggregation.

3.3.2 Support Effect on Electronic Structure of Pt₁₃ isomers

It is well known that chemisorption of adsorbates on transition metal surfaces is strongly correlated with the so-called *d*-band center energy of the surface.¹¹³ Several studies have now extended this metric to the study of supported clusters and shown similar correlations.^{57, 59, 167} In particular, the influence of cluster morphology as well as the role of the support in modulating the *d*-band center energy are issues of current interest for rational catalyst design. Our ability to produce low-energy isomers at low computational expense using the GA now allows us to examine more broadly the issues of cluster morphology and support effects on the catalytic activity of clusters (beyond the limited cases studied in our previous work⁵⁹⁻⁶⁰). As an example, we focus here on Pt₁₃ clusters; more comprehensive studies across a range of cluster sizes will be reported elsewhere.

Using GA, we identified several Pt₁₃ isomers within a 30 meV/atom energy window close to the global minimum for Pt₁₃ in vacuum or with various support types. All candidates, supported or otherwise, were imported into VASP and subjected to conjugate-gradient structural relaxation. For vacuum Pt₁₃ isomers, an additional 15 candidates were obtained by simply eliminating the support from the low-energy Pt₁₃/graphene systems and relaxing the residual Pt₁₃ cluster; such clusters are merely local rather than global minima, but including these in our analyses gives us a larger statistical sample for studying

structure-property correlations.

Figure 3.4 (a) displays d -band center energies as a function of cluster adsorption energy and formation energy for supported and unsupported clusters, respectively. For unsupported clusters, the d -band center energy varies almost linearly with the formation energy and spans about 0.1 eV within a formation energy window of width 0.2 eV/atom. In the presence of the graphene support, ϵ_d can be significantly lowered, especially in the presence of vacancy and divacancy defects, and once again the lowering of the d -band center is correlated with the adsorption energy, which was also noted earlier by Fampiou and Ramasubramaniam.⁶⁰ In general, for the various clusters on defective supports, we find that when a Pt atom occupies the center of the defect (vacancy/divacancy), the total energy as well as the adsorption energy decrease significantly, as indicated by the points within the dashed square in Figure 3.4 (a); this decrease in adsorption energy is accompanied by a drop in the d -band center energy. Furthermore, for all cases of clusters on defective supports, the d -band center lies slightly below that for Pt (111), suggesting comparable or possibly weaker adsorbate binding. In the absence of point defects, the cluster d -band center approximately coincides with the calculated value for Pt (111); for unsupported clusters, the d -band centers are appreciably higher than that for Pt (111).

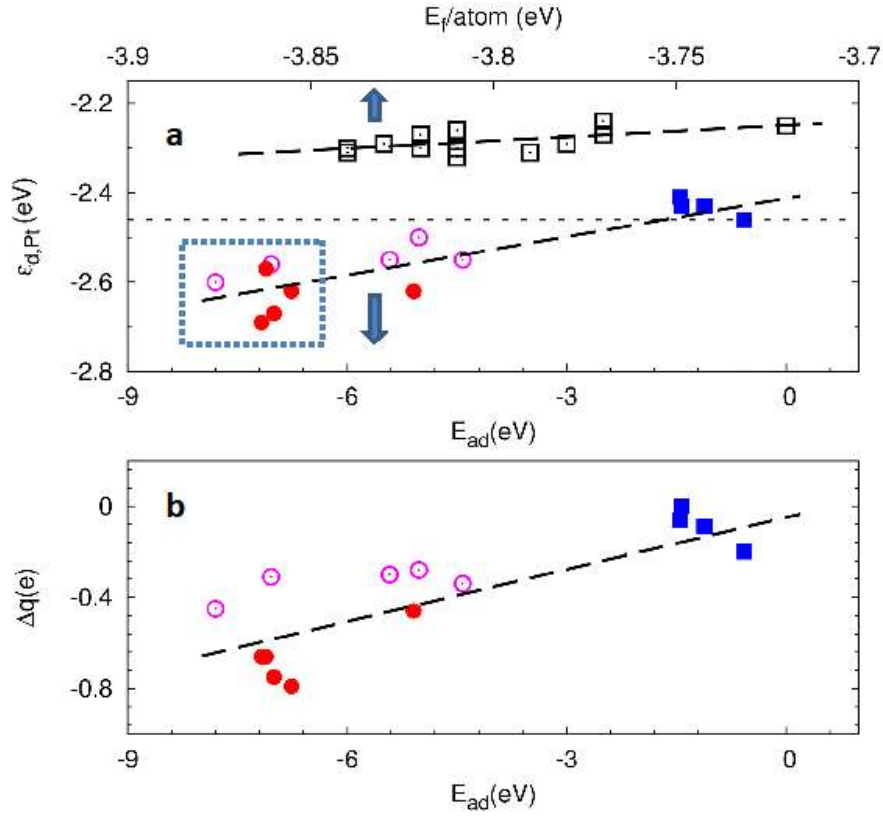


Figure 3.4. Position of d -band center ($\epsilon_{d,Pt}$) relative to the Fermi level (a) and net charge transferred (b) to Pt₁₃ isomers in vacuum and on graphene support. Data for Pt₁₃ clusters in vacuum and on support are plotted with respect to the formation energy (E_f) per atom and the adsorption energy (E_{ad}), respectively. The horizontal dashed line represents $\epsilon_{d,Pt}$ for Pt (111) surface. Other dash lines are guides to the eyes. Points inside dashed square correspond to structures with Pt atoms occupying the center of the defect.

As noted in prior work,^{57,60} the total charge transferred from the cluster to graphene is an important factor in shifting the cluster d -band center. Thus, we also perform a Bader charge analysis,¹⁶⁸⁻¹⁶⁹ to evaluate the total charge transferred from the cluster to the graphene support. Figure 3.4 (b) displays the transferred charge with respect to the adsorption energy and the trends are similar to that of the d -band analysis. Similar to previous reports,⁶⁰ we observe that stronger binding of clusters to the support results in greater depletion of charge from the cluster, which then leads to a lowering of the d -band center of the cluster.

A complementary and chemically intuitive view of bonding at the Pt-C interface can also be obtained from a natural bond orbital (NBO) analysis¹⁷⁰⁻¹⁷¹ of low-energy structures for Pt₁₃ on vacancy and divacancy (

Figure 3.5). We used the method and associated package developed by Dunnington and Schmidt⁵ to yield localized representation of bond for a periodic system. A Gaussian-type atom centered SBKJC basis set was used for both C and Pt to project the plane-wave (PW) based electronic wave functions. For Pt₁₃ on pristine graphene, NBO analysis shows negligible covalent bonding between Pt and C atoms and hence, we don't pursue this case in detail here. For a Pt₁₃ cluster bounded a vacancy in graphene, a predominant covalent picture can be observed for atoms at the interface, as shown in

Figure 3.5 (a) and Table 3.3. For a Pt₁₃ cluster bound at a divacancy in graphene, we also observe, for the most part, clear sp³ hybridization of C atoms involved in C-Pt bonds (C₁-Pt₁₃₈, C₁₅-Pt₁₃₈, C₁₁₂-Pt₁₃₈, C₁₄-Pt₁₃₈). The occupancies of the bonding states in all cases (~1.9) are consistent with localized two-center bonding. Nevertheless, in all cases there is non-negligible occupation of antibonding states (as high as 0.78 for C₁₄-Pt₁₃₈) indicative of a more complex nature of C-Pt bonds rather than a simple covalent picture. Irrespective of these fine details, the overall polarization towards carbon atoms in the C – Pt σ bonds agrees with the picture of charge transfer from Pt to graphene, as inferred from Bader analysis. In addition, the polarization towards carbon atoms in the covalent bond agrees well with the overall charge transfer from Pt to graphene, as shown in Figure 3.7.

Broadly speaking, the NBO analysis does not show any significant bonding between Pt₁₃ clusters and pristine graphene; for the defective graphene supports, a predominantly covalent nature is found for C-Pt bonds at the defect center with clear polarization towards

the C atoms, which bolsters the picture of charge transfer from Pt to graphene obtained from the Bader analysis.

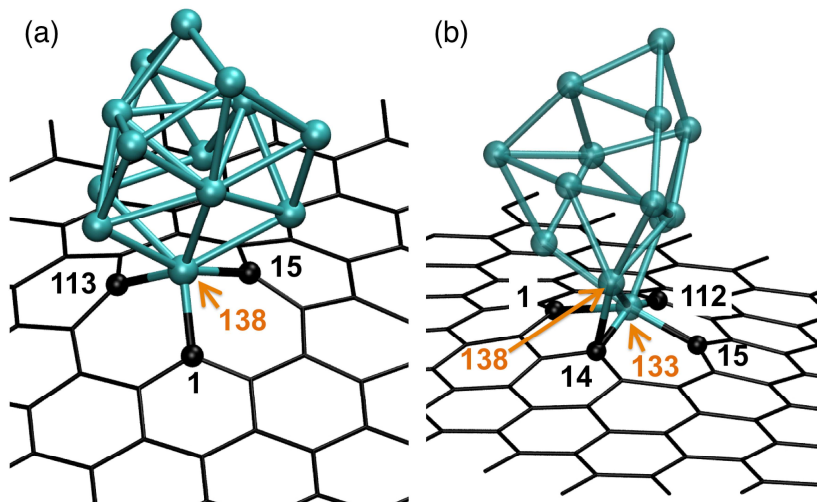


Figure 3.5. Pt_{13} clusters on vacancy (a) and divacancy (b) graphene support. Labels are the indices of atoms forming covalent bonds at the interface.

The electronic structure analysis presented here is essentially in agreement with previous work by Fampiou and Ramasubramaniam,⁶⁰ among others,⁵⁷ although with much better statistics and more careful attention to computational procedures for generating low-energy structures. The role of the support is relatively clear in our studies: defective supports appreciably lower the *d*-band centers, at least of small Pt clusters, and consequently have implications for adsorbate binding and reaction barriers.⁵⁸⁻⁵⁹ In terms of proper selection of structures for electronic structure analyses and/or studies of reaction pathways, it would appear that small deviations from the minimum-energy cluster morphology are unlikely to lead to large deviations in the energies of the surface states at least for small clusters. Thus, we expect that any reasonably robust method for generating low-energy morphologies ought to result in plausible predictions of catalytic behavior from subsequent electronic structure studies.

Table 3.3. Covalent NBOs for Pt₁₃ on vacancy graphene

NBO	Occupancy	Center (bond % polarization)	Hybridization (function,%)
C – Pt σ^*	0.32	C(1)(56) Pt(138)(44)	s 24, p 76 s 32, p 68,
C – Pt σ	1.87	C(1)(44) Pt(138)(56)	s 24, p 76 s 27, p 6, d 66
C – Pt σ^*	0.26	C(15)(55) Pt(138)(45)	s 25, p 75 s 33, p 67,
C – Pt σ	1.87	C(15)(45) Pt(138)(55)	s 25, p 75 s 30, p 7, d 63
C – Pt σ^*	0.34	C(113)(56) Pt(138)(44)	s 24, p 76 s 32, p 68,
C – Pt σ	1.87	C(113)(44) Pt(138)(56)	s 24, p 76 s 27, p 6, d 67

Table 3.4. Covalent NBOs for Pt₁₃ on divacancy graphene

NBO	Occupancy	Center (bond % polarization)	Hybridization (function,%)
C – Pt σ^*	0.47	C(1)(60) Pt(133)(40)	s 24, p 76 s 23, p 4, d 72
C – Pt σ	1.88	C(1)(40) Pt(133)(60)	s 24, p 76 s 23, p 4, d 72
C – Pt σ^*	0.48	C(14)(61) Pt(133)(39)	s 19, p 81 s 22, p 4, d 74
C – Pt σ	1.87	C(14)(39) Pt(133)(61)	s 19, p 81 s 22, p 4, d 74
C – Pt σ^*	0.73	C(14)(76) Pt(138)(24)	s 13, p 87 d 100
C – Pt σ	1.82	C(14)(24) Pt(138)(76)	s 13, p 87 d 100
C – Pt σ^*	0.57	C(15)(65) Pt(133)(35)	s 23, p 77 s 20, p 3, d 77
C – Pt σ	1.89	C(15)(35) Pt(133)(65)	s 23, p 77 s 20, p 3, d 77
C – Pt σ^*	0.41	C(112)(57) Pt(133)(43)	s 27, p 73 s 26, p 6, d 68
C – Pt σ	1.90	C(112)(43) Pt(133)(57)	s 27, p 73 s 26, p 6, d 68

3.3.3 Charge Transfer Between Pt clusters and Graphene Support

Finally, data for adsorption energies of several clusters of varying sizes on defective and defect-free graphene supports calculated by DFT are displayed in the (Figure 3.6), as are the charge transfer data associated with these various cases (Figure 3.7).

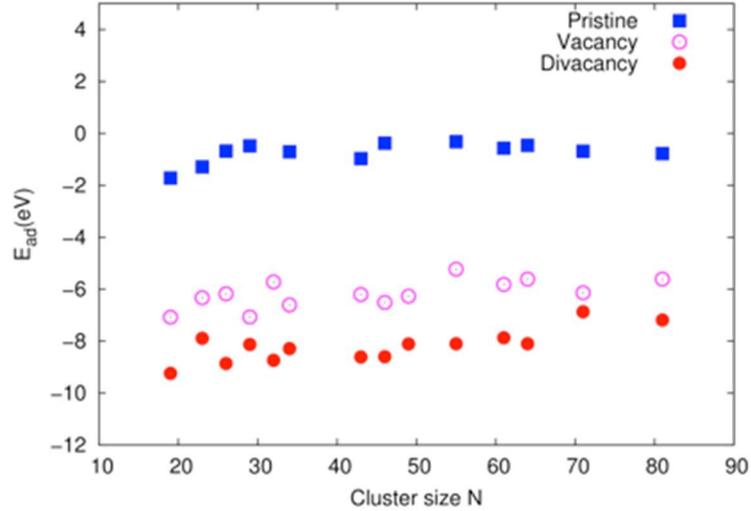


Figure 3.6. DFT adsorption energies for selected Pt_N clusters in the size range $N=20-80$ on defective and defect-free graphene supports.

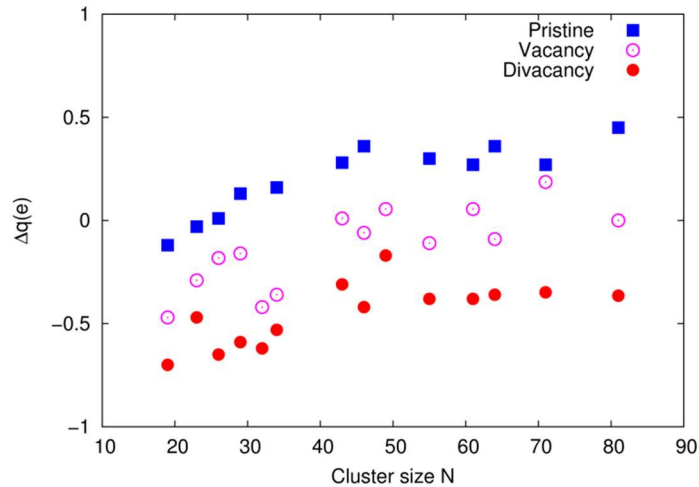


Figure 3.7. Charge (Δq in electrons) transferred from Pt_N clusters to defective and defect-free graphene supports for selected clusters in the size range $N = 20-80$.

Figure 3.7 displays the calculated charge transfer between the low-energy clusters and the defective/defect-free graphene supports. With increasing cluster size, there is an

overall decrease—although not necessarily monotonic—in the extent of charge transferred from the cluster to the support. Furthermore, the extent of charge transfer for any particular cluster size is directly correlated with the strength of binding to the graphene support. Interestingly, for clusters on pristine graphene, when the cluster size exceeds $N \approx 30$, the direction of charge transfer between the cluster and support is reversed: the support donates charge to the Pt cluster rather than the other way around. The onset of a similar reversal in the direction of charge transfer is seen for Pt clusters bound at vacancy defects at $N \approx 40$. For the range of cluster sizes studied here, there is no such reversal in the direction of charge transfer for clusters bound at divacancies, i.e., the cluster always loses electrons to the support. More systematic correlations between these charge transfer trends and the catalyst *d*-band shifts are currently being investigated.

3.4 Conclusions

We implemented an empirical-potential based GA for structural optimization of unsupported and supported Pt nanoclusters. Using a bond-order potential for the Pt-C system developed by Albe et al., we explored the morphological properties of Pt_N ($N = 2-80$) clusters considering unsupported clusters as well as those supported on pristine or defective graphene supports. A key finding from the structural analysis is that the fraction of potentially active surface sites for Pt clusters is maximal for 20-30 atom clusters irrespective of the presence or absence of the support and support defects; this result provides a useful synthetic target for optimal utilization of the precious metal catalyst. Selected ground-state clusters from the GA process were subjected to structural relaxation with DFT calculations and compared with corresponding high-symmetry icosahedral and

cuboctahedral clusters. For all “magic number” clusters, the GA optimization process produced cluster morphologies that are lower in energy than their high-symmetry counterparts (both at the empirical potential and DFT levels). The inclusion of the graphene support is found to influence cluster morphologies at very small sizes; beyond ~ 10 atoms, the cluster morphology is essentially dominated by Pt-Pt interactions with minimal perturbations from the support, at least for the cases considered here with small point defects in the support. From a case study of Pt_{13} clusters, we found that graphene supports—in particular, defective ones—can lower the d -band center relative to the Fermi level, which is expected to correspondingly reduce the binding energies of catalyst poisons such as CO.

CHAPTER 4

STABILITY AND ENERGETICS OF PtRu ALLOY CLUSTERS

4.1 Introduction

Platinum and platinum-group metals serve as important electrocatalysts in hydrogen-based or methanol-based proton-exchange-membrane fuel cells (PEMFC).^{99, 147, 172} In spite of the widespread use of these metals, there are still important challenges that need to be met in ensuring catalyst selectivity and durability. For example, carbon monoxide, which is a common impurity in hydrogen feeds or produced as a reaction intermediate, easily poisons the active sites of Pt catalysts. PtRu alloy clusters are known to show the highest resistance to CO poisoning and highest catalytic activity in PEMFCs.⁹⁹ Yet, there remain important gaps in our systematic understanding of the influence of size, structure, and composition of PtRu alloys on catalytic performance at the nanoscale (alloy nanoclusters).

DFT is a particularly useful tool for calculating potential energy surfaces and has been widely used for global optimization of nanoscale alloy structures.¹⁷³⁻¹⁷⁴ On the one hand, DFT requires very few adjustable parameters making it a reliable modeling tool for most chemical elements. On the other hand, the unfavorable scaling of the method which implies that optimization studies at the DFT level are typically limited to small clusters. Empirical interatomic potentials, which are much less computationally demanding, can help push the size limit on cluster optimization studies. However, these suffer from their own drawbacks in terms of transferability and possible over-parameterization. In the present context, we

are unaware of widely-used, well-tested interatomic potentials for Pt-Ru alloy clusters, which stymies progress in modeling this important class of catalysts.

Density-functional tight-binding (DFTB) represents another powerful modeling approach that has been widely employed for studying carbon-based systems¹⁷⁵⁻¹⁷⁶ and metals with delocalized valence electrons.¹⁷⁷⁻¹⁷⁹ Recently, the accuracy of DFTB has been further improved¹⁸⁰⁻¹⁸¹ by adding self-consistent charge (SCC) corrections to take into account charge transfer due to interatomic interactions. The computational speed of SCC-DFTB is intermediate between DFT and empirical potential methods thus opening up possibilities for global optimization for larger clusters sizes with high accuracy. Thus, the primary goal of this paper is to obtain an accurate set of SCC-DFTB parameters for modeling PtRu alloy clusters. (We use the terms SCC-DFTB and DFTB interchangeably from here on for convenience.) In the process, of developing a suitable parameterization for Pt-Ru interatomic interactions, we also obtain an accurate set of parameters for the homo-elemental Pt-Pt and Ru-Ru interactions, which also do not exist in the literature to date. Thus, our work contributes an important set of tools for SCC-DFTB modeling of Pt, Ru, and PtRu clusters that can be employed in a wide range of applications, including molecular dynamics and structural optimization, while pushing the size limits currently imposed by more expensive DFT-based approaches.

4.2 Computational Methods

4.2.1 SCC-DFTB Method

Formally, the total energy, E , of a tight-binding system can be expressed within the DFTB approximation as¹⁷⁷

$$E = E_{bs} + E_{Coul} + E_{rep}, \quad (4.1)$$

where E_{bs} is the band structure energy, E_{Coul} is the Coulomb interaction energy and E_{rep} is the repulsive energy. In the DFTB formalism, E_{bs} is obtained simply from the summation of orbital interaction energies, which are constants that only need to be calculated once for a given set of elements, while E_{Coul} is determined by a single parameter, namely, the Hubbard U parameter. All cumbersome terms related to electron exchange and correlation as well as terms related to ion-ion repulsion are clumped together in the pairwise potential, $V_{rep}(R_{IJ})$, from which the repulsive energy is obtained as

$$E_{rep} = \sum_{I < J} V_{rep}(R_{IJ}). \quad (4.2)$$

The potential function, $V_{rep}(R_{IJ})$, is treated as an empirical function that is to be determined by fitting to experimental data and/or data from higher-level electronic structure calculations. In this work, we employ training sets obtained from DFT calculations. The details of the fitting procedure and results of subsequent tests are reported in Section 3. For now, we simply note that the potential fitting in this work was performed using the Hotbit package¹⁸² Slater-Koster parameter tables from Hotbit were converted to the standard DFTB format and the DFTB+ package¹⁸² was used for the testing phase as well as for subsequent global optimization studies.

4.2.2 Calculation Procedures

First, we performed DFT calculations on randomly generated PtRu clusters of varying size and composition (20 clusters in total) to create a large database (approximately 200

samples) of equilibrium (structurally optimized) and non-equilibrium (artificially deformed) structures, energies, and forces. Thereafter, 50% of this database was used as a training set to parameterize DFTB potentials for Pt-Pt, Pt-Ru and Ru-Ru interactions; the remaining 50% of the database was used as a testing set to verify the accuracy of the DFTB-predicted energetics relative to DFT. Since the clusters used in the fitting procedure were randomly generated, the ability of the DFTB potentials to predict minimum energy configurations of clusters with accuracy remained to be verified. Therefore, as the second phase of the simulations, the potential energy surface generated by the Pt-Ru DFTB model was sampled using a GA and minimum energy configurations calculated for a selected set of clusters of varying sizes and compositions (see Table 4.1). The DFTB-optimized minimum energy clusters were imported into VASP and further minimized using a conjugate-gradient algorithm (local minimization) at the DFT level. The DFTB and DFT results were then compared in terms of cluster formation energies to validate trends across cluster sizes and compositions.

4.3 Parameterization and Testing of SCC-DFTB Potentials

In the first step of potential parameterization, the onsite energies of valence orbitals (ϕ_μ) in free atoms are obtained for calculating the diagonal elements ($H_{\mu\mu}^0 = \langle \phi_\mu | H | \phi_\mu \rangle = \epsilon_{\text{free}}$) of the Hamiltonian matrix. Using the Hotbit package, ϵ_{free} was obtained from all-electron, scalar-relativistic DFT calculations with the PW92 local density approximation¹⁸³ for electron exchange and correlation. The onsite energies of the valence orbitals for Pt and Ru are listed in Table 4.2. The charge transfer energetics can be described within DFTB by a single key parameter, the Hubbard U, having the default value¹⁸⁴

$$U \approx IE - EA \quad (4.3)$$

where IE is the ionization energy and EA the electronic affinity. The ionization energy and electron affinity are calculated by removing and adding electrons from and to corresponding orbitals of the unconfined atom and then calculating the energy change. Although Hubbard U values can differ by orbital, for simplicity, we use the same U for all orbitals. As adding a full electron may cause convergence problem, only a fraction of an electron is added or removed in practice (0.15 and 0.2 electrons for Pt and Ru *d*-orbitals, respectively). U values calculated from DFT are listed in Table 4.2.

As free-atom orbital wavefunctions are too diffuse to be considered as basis functions for wavefunction expansion in DFTB, a common strategy to generate more compact orbital basis sets is to model a pseudo-atom, in which an additional confinement is used to mimic the atomic environment. We use here a common choice for confinement, namely a quadratic form potential¹⁷⁶

$$V_{conf}(r) = \left(\frac{r}{r_0}\right)^2, \quad (4.4)$$

where, as a rule of thumb r_0 is chosen to be twice the covalent radius. Thus, in the second step of DFTB parameterization, the localized basis functions of valence orbitals for the confined pseudo-atom were calculated with all-electron DFT (in Hotbit). At the end of the first two steps, the Hamiltonian and overlap matrices for elementary integrals as a function of distance are calculated once and for all for interaction of two atoms and stored in a parameter file (Slater–Koster table).

Table 4.1. Lowest energy (in eV) found by GA and simulated-annealing (SA) method

Atom Size N	x% (Pt)	N _{Pt}	N _{Ru}	GA	SA
13	0	0	13	-759.44	-757.79

13	25	3	10	-805.28	-801.07
13	50	6	7	-850.70	-849.03
13	75	10	3	-911.21	-909.45
13	100	13	0	-953.27	-951.95
28	0	0	28	-1648.91	-1641.96
28	25	7	21	-1753.17	-1746.93
28	50	14	14	-1859.13	-1853.09
28	75	21	7	-1962.74	-1956.27
28	100	28	0	-2062.51	-2059.71
32	0	0	32	-1885.62	-1878.28
32	25	8	24	-2003.99	-1998.58
32	50	16	16	-2124.23	-2112.82
32	75	24	8	-2244.73	-2236.32
32	100	32	0	-2358.89	-2356.79
55	0	0	55	-3247.15	-3242.32
55	25	14	41	-3456.19	-3441.76
55	50	28	27	-3666.78	-3651.25
55	75	41	14	-3860.30	-3852.03
55	100	55	0	-4068.83	-4059.78
81	0	0	81	-4790.87	-4786.96
81	25	20	61	-5087.53	-5070.88
81	50	40	41	-5385.75	-5363.58
81	75	61	20	-5699.71	-5680.94
81	100	81	0	-5998.52	-5988.39

Table 4.2. Electronic configurations and confinement potential parameters for Pt and Ru

Element	Valence shell	$r_0(\text{Bohr})$	N	$\varepsilon_d(\text{Ha})$	$\varepsilon_p(\text{Ha})$	$\varepsilon_s(\text{Ha})$	$U_d(\text{Ha})$
Pt	5d ⁹ 6s ¹ 6p ⁰	4.80	2	-0.235	-0.035	-0.218	0.367
Ru	4d ⁷ 5s ¹ 5p ⁰	5.27	2	-0.199	-0.038	-0.166	0.356

In the third and final step, we fit the repulsive pairwise function, $V_{\text{rep}}(R_{IJ})$, that accounts for ion-ion interaction and exchange-correlation effects. The parameters of this potential can be optimized by fitting to a suitable training set. It is well known that DFTB approximations are sufficiently crude so that training data from a single system result in poor transferability. Thus in order to achieve higher transferability, we model numerous clusters with different size and geometries in DFT and use these data for training and testing purpose. As force (energy gradient) minimization rather than energy minimization is the appropriate metric for structural optimization, we define our objective function as

$|\mathbf{F}^{\text{DFT}}(\mathbf{R}) - \mathbf{F}^{\text{DFTB}}(\mathbf{R})|$, which is norm of the force difference between DFT benchmarks and DFTB outputs.

Figure 4.1 displays the results of the training procedure as applied to Pt-Pt, Ru-Ru, and Pt-Ru interactions. All training data are from DFT calculations with spin polarization; the DFTB parameterization developed in this work does not include either spin polarization or spin-orbit effects. To the extent that our goal is to simply employ DFTB for structural optimization rather than detailed electronic structure calculations, this approach is similar in spirit to empirical potential approaches. The training set employed here includes (strained) atomic dimers, which we find to be very important in determining the shape of the repulsive potential curves over a large range of interatomic distances. For larger clusters, we similarly employ both ground state configurations as well as structures that are homogeneously expanded or contracted to sample a range of atomic environments. As seen from Figure 4.1, the training procedure results in repulsive potentials that are in excellent agreement for both homo-elemental and alloy systems. In particular, we found that empirically tuning the d -orbital energies ε_d relative to their default DFT-calculated values (Table 4.2) has a significant effect on the quality of the data fits. Figure 4.1 displays the results for the optimal onset energies (-0.25 Ha for Pt and -0.24 Ha for Ru).

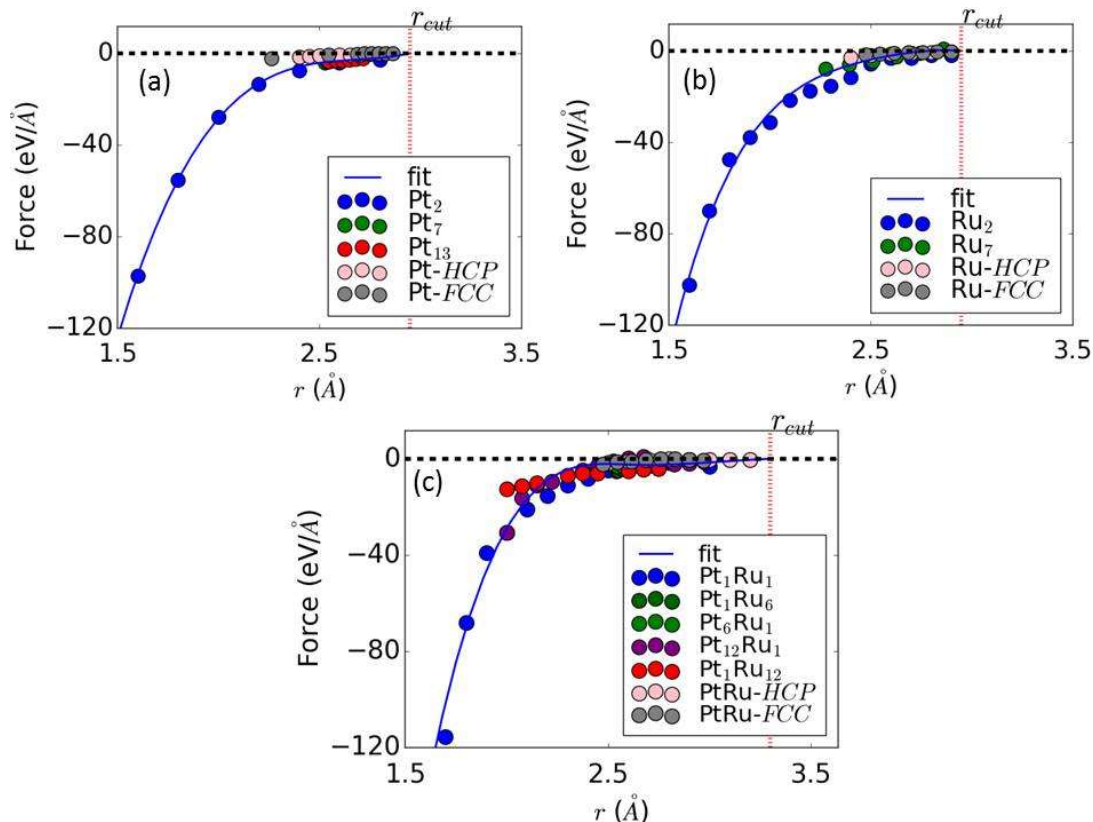


Figure 4.1. Fitting the derivatives of repulsive potential: (a): Pt-Pt interaction; (b): Ru-Ru interaction; (c): Pt-Ru interaction. Family of points are from various structures. Here $r_{cut} = 3.3$ Å.

While we also attempted to include bulk data in the training set, this seemed to adversely affect accuracy for clusters. Since our focus here is on modeling alloy clusters rather than bulk systems, we chose not to include bulk data in the training sets. The transferability of the homo-elemental parameterizations (Pt-Pt and Ru-Ru) from cluster data is nevertheless satisfactory for bulk Pt and Ru systems as shown in Table 4.3; the transferability to bulk Pt-Ru alloys is, however, poor and we caution against using this DFTB parameter set beyond clusters.

The quality of the DFTB parameterization is tested by comparing cluster formation energies calculated using both DFTB and DFT as shown in Figure 4.2. The formation energy for a Pt_mRu_n cluster (on a per atom basis) is defined as

$$E_f = [E(\text{Pt}_m\text{Ru}_n) - m E_{\text{Pt}} - n E_{\text{Ru}}]/(m + n), \quad (4.5)$$

where $E(\text{Pt}_m\text{Ru}_n)$ is the total energy of the cluster, and E_{Pt} and E_{Ru} are the energies per atom of bulk FCC Pt and HCP Ru, respectively. Test geometries for each size and composition are based on cluster morphologies from our previous study on Pt nanoclusters;¹⁸ Ru and PtRu clusters are simply generated by replacing Pt atoms in these clusters and subjecting them to structural relaxation. In general, we see that for both homoelemental as well as alloy clusters, the DFTB formation energies faithfully represent the target DFT data. Indeed, in addition to R^2 values being very close to one, indicating small statistical scatter, the slopes of the fits are also close to unity, indicating excellent one-to-one correspondence in the DFTB and DFT formation energies. Based on this successful parameterization, we pursue next a few examples of GA-based morphological optimization of PtRu alloy clusters.

Table 4.3. Calculated structural and energetic properties of Pt and Ru in the bulk phase. Listed below are lattice constants a and c , cohesive energy per atom E_{cov} , formation energy E_f , and surface energies.

Pt (FCC)	DFT	DFTB				
$E_d(\text{Ha})$		-0.17	-0.20	-0.25	-0.26	-0.29
a (Å)	3.95	4.14	4.13	4.14	4.14	4.15
$E_{\text{cov}}(\text{eV})$	-5.90	-5.63	-8.10	-5.63	-6.71	-5.12
(111)	0.63	0.52	0.50	0.52	0.53	0.57
(100)	0.91	0.74	0.77	0.74	0.75	0.74
Ru(HCP)	DFT	DFTB				
$E_d(\text{Ha})$		-0.16	-0.19	-0.22	-0.24	-0.26
a (Å)	2.72	2.76	2.75	2.71	2.70	2.73
c/a	1.57	1.58	1.57	1.57	1.56	1.56
$E_{\text{coh}}(\text{eV})$	-8.74	-12.68	-11.07	-9.18	-8.63	-6.73
(0001)	1.05	1.12	0.99	0.99	0.88	0.76
(1010)	2.61	3.20	2.63	2.47	2.15	1.80
Pt-Ru		DFT	DFTB ^a			
	HCP	0.24	2.44			
	FCC	0.19	2.33			
$E_f(\text{eV})^b$	BCC	0.81	5.25			
	SCC	1.74	2.89			
	HCP	2.78(1.58)	2.76(2.08)			
$a(c/a)(\text{Å})$	FCC	3.90	4.55			
	BCC	3.10	3.51			
	SCC	2.60	2.57			

^a $E_d^{\text{Pt}} = -0.25 \text{ Ha}$, $E_d^{\text{Ru}} = -0.24 \text{ Ha}$

^b $E_f = E_{\text{PtRu}} - E_{\text{Pt}} - E_{\text{Ru}}$ where E_{PtRu} is the total energy of a Pt-Ru pair in a fictitious Pt_1Ru_1 alloy. E_{Pt} and E_{Ru} are the energy of a single Pt and Ru in FCC and HCP lattice, respectively.

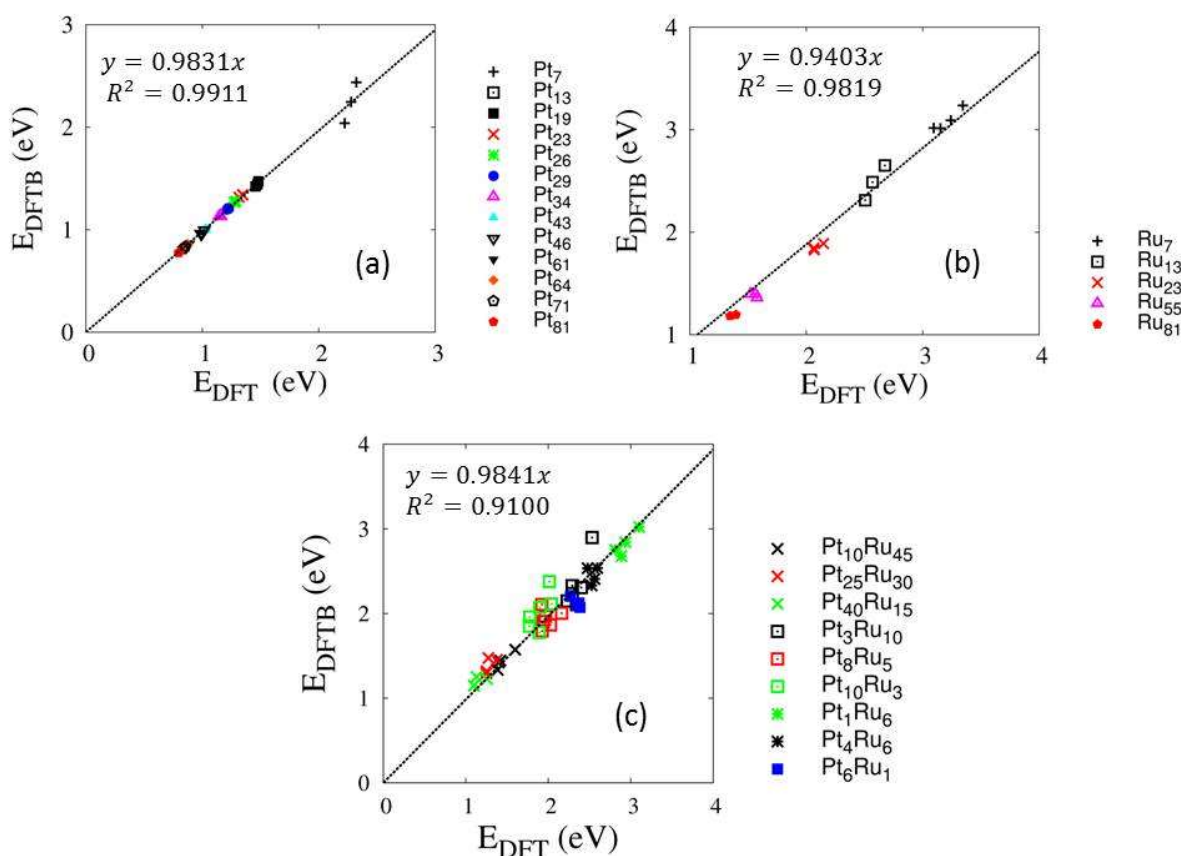


Figure 4.2. Comparison of DFT and DFTB formation energies of Pt, Ru and PtRu clusters. Dashed lines indicate the least-squares fit to the data. The slopes of the lines (ideally unity) and the R^2 values indicate an accurate DFTB representation of the target DFT data.

4.4 DFTB-Based GA Optimization of PtRu Clusters

We now apply our new SCC-DFTB parameterization to the problem of ascertaining minimum-energy morphologies of PtRu clusters as a function of cluster size and composition. The goal here is not to undertake a detailed study of the structural and electronic properties of PtRu alloy clusters but simply to use the DFTB parameterization in conjunction with a GA to confirm experimentally observed features of sub-nanometer PtRu clusters and validate the model. As examples, we consider PtRu clusters with 13, 32, 55, and 81 atoms with (approximate) Pt atomic fractions of 0%, 25%, 50%, 75% and

100% in each case. Figure 4.3 displays the various minimum-energy cluster morphologies for various cluster sizes and composition. As seen from Figure 4.3, the clusters exhibit low-symmetry morphologies in all cases with little or no resemblance to high-symmetry icosahedral or cuboctahedral geometries as is often assumed *ad hoc* in computational studies. In particular, the finding that low-energy Pt clusters typically adopt low-symmetry structures at small sizes is consistent with several prior studies.^{60, 109, 137} In the case of PtRu alloy clusters, it is well known from several experimental studies¹⁸⁵⁻¹⁸⁶ that Pt atoms preferentially occupy surface sites whereas Ru atoms segregate towards the core sites. This is also borne out by our simulations, as seen from Figure 4.3, wherein we consistently find segregation of Pt atoms to the surface with (near) core-shell-like morphologies visible at intermediate Pt compositions. As noted by Wang et al.,¹⁸⁶ this segregation is a mechanism for reducing the energetically unfavorable filling of antibonding states of Pt that occurs during alloying with Ru. One may also note that the cohesive energy of HCP Ru is much stronger than that of FCC Pt (by 2.8 eV; Table 4.3), whereas the surface energies of typical low-index Miller surfaces of Ru are higher than that of Pt (Table 4.3); both of these facts would also point towards the tendency for phase segregation with Pt preferentially occupying surface sites.

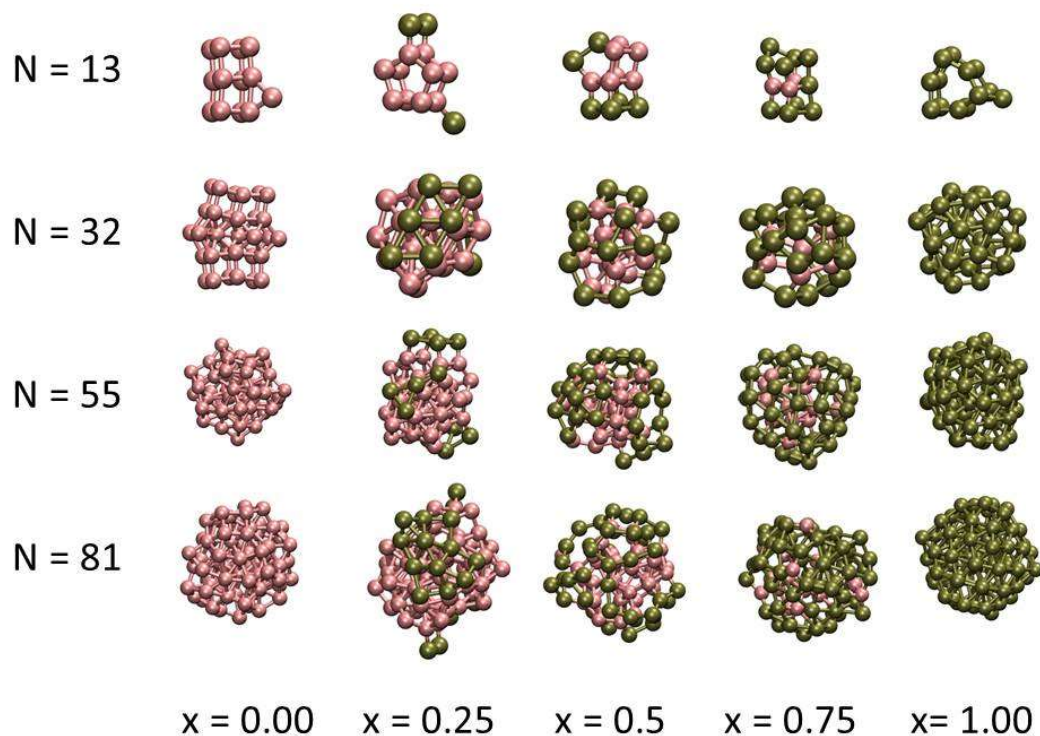


Figure 4.3. Morphologies of minimum-energy PtRu clusters of various sizes (N – number of atoms) and compositions (x – Pt fraction) as predicted by our DFTB-based GA implementation. Gold and pink spheres represent Pt and Ru atoms, respectively.

As a quantitative comparison of the DFTB model against DFT, we display in Figure 4.4 the formation energies of the GA-optimized clusters (Figure 4.3). The DFTB results are obtained by the application of the GA; these GA-optimized clusters are simply imported into VASP and subjected to a conjugate-gradient structural relaxation (local energy minimization) after which formation energies are calculated using Equation 4.5. In general, we see from Figure 4.4 that at any given composition, smaller clusters have larger formation energies (less thermodynamically stable), which is to be expected due to the larger number of undercoordinated atoms in smaller clusters. For the 13-atom cluster, both DFTB and DFT predict a minimum formation energy at $x=0.75$. For the 32-atom cluster, DFTB predicts a shallow minimum in formation energy at $x=0.75$, which is not captured

in DFT. For larger clusters, the DFTB and DFT results agree in predicting a monotonic decrease in formation energy from pure Ru to pure Pt clusters. In general, DFTB tends to underestimate formation energies relative to DFT (on average by about 0.41 eV/atom) although the overall trends are broadly captured. Nevertheless, to the extent that we propose to use DFTB as a “pre-processing” step to search the potential-energy hypersurface for low-energy candidates for subsequent higher-level DFT calculations, the agreement may be deemed satisfactory.

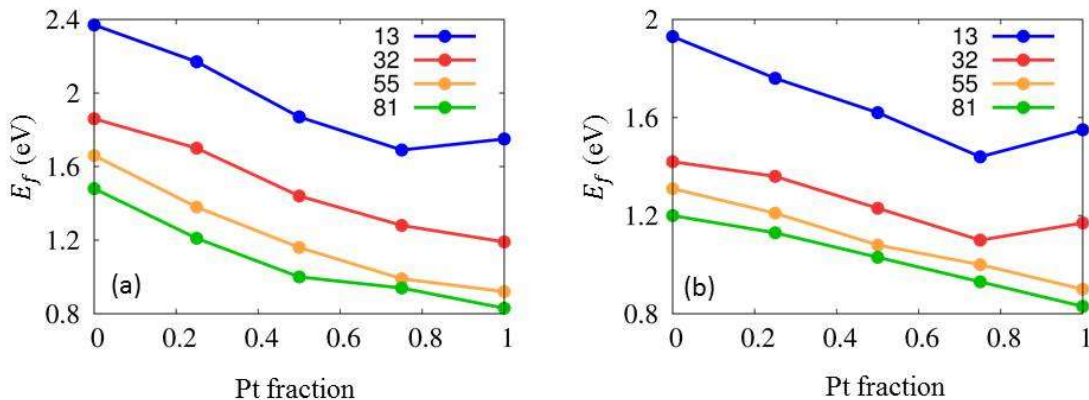


Figure 4.4. Formation energies of GA-optimized PtRu clusters (displayed in Figure 4.3) as a function of Pt concentration, calculated with (a) DFT and (b) DFTB. Cluster sizes (number of atoms) are indicated in the legends.

4.5 Conclusions

We have developed an SCC-DFTB parameterization that allows us to model chemical bonding in Pt-Ru alloy clusters. The parameter set was developed by using a training set of first-principles DFT data for homo-elemental (Pt and Ru) and alloy clusters. Our new parameterization is able to describe the thermodynamics (formation energies) of Pt, Ru, PtRu nanoclusters in excellent agreement with benchmark DFT calculations.

As an example application, we employed the validated DFTB parameter set within a GA for structural optimization of PtRu clusters and showed that the procedure correctly captures surface segregation of Pt in PtRu nanoclusters. The low-energy structures predicted by the DFTB-based GA can serve as good starting points for future investigations of electronic properties and catalytic activity with higher-level DFT calculations. More broadly, the new DFTB parameter set for Pt-Ru interactions presented in this work opens up avenues for detailed investigation of structure–function relationships in this important class of catalytic materials.

CHAPTER 5

CONCLUSIONS AND FUTURE WORK

5.1 Conclusions

The aim of this thesis was to investigate the effects of particle size and structure, supports (graphene), and alloying (with Ru) on the catalytic properties of Pt nanoclusters with the aim of providing useful targets for catalyst design. Below, we summarize the key findings and conclusions of our work.

First, we studied unsupported Pt nanoclusters using an empirical-potential-based GA and determined the thermodynamically relevant, low-energy structures. For nanoclusters up to 309 atoms (~ 1.5 nm), low-symmetry structures were found to be consistently preferred over high-symmetry ones, especially for small cluster sizes. GA-optimized clusters show a non-monotonic decrease of surface d -band centers with respect to size, and a minimum around Pt₁₀₀ was found. CO adsorption on GA-optimized clusters also presented similar non-monotonic behavior with a global maximum at around Pt₅₅. By employing machine-learning algorithms that incorporate a combination of structural and electronic descriptors, we were able to achieve significant improvement in the prediction of CO binding energies compared with traditional d -band model.

Next we explored the energetics and morphology of Pt_{*N*} ($N = 2$ -309) clusters supported on graphene supports. We found that the fraction of potentially active surface sites for Pt clusters is maximal for 20-30 atom clusters on graphene support; noticeable modification of cluster morphologies from their unsupported cases were observed only when clusters were smaller than ten atoms and primarily on defective graphene supports. The effect of the support—more precisely support defects—on the electronic properties of

Pt clusters is more pronounced. For the cases of supported Pt₁₃ clusters studied here, the cluster *d*-band energy is downshifted relative to the Fermi level in direct proportion to the strength of binding of the cluster to the support. Cluster adsorption energies on the support and the attendant *d*-band shifts are sensitive to the precise details of bonding at the cluster–support interface, especially for small clusters, requiring careful structural optimization. By integrating computationally inexpensive empirical-potential based GAs for global structural optimization with DFT modeling for local minimization and electronic structure analyses, we demonstrated a viable approach for systematic studies of supported catalyst nanoclusters.

In the last part of this thesis, we developed an SCC-DFTB parameterization that allows us to model chemical bonding in Pt-Ru alloy clusters. The parameter set was developed by employing a training set of cluster energies and interatomic forces obtained from Kohn-Sham DFT calculations for homo-elemental and alloy clusters. Extensive simulations of a testing set of PtRu alloy nanoclusters show that this SCC-DFTB scheme is capable of capturing cluster formation energies with high accuracy relative to DFT calculations. The new SCC-DFTB parameterization was employed within a GA to search for global minima of PtRu clusters in the range of 13-81 atoms and the emergence of Ru-core/Pt-shell structures at intermediate alloy compositions was systematically demonstrated. Our new SCC-DFTB parameterization now enables computationally inexpensive modeling of Pt-Ru clusters that are among the best-performing catalysts in numerous energy applications. Minimum-energy structures found in this work can be used as good starting points for DFT investigations of electronic properties in the future.

While this work was restricted to the Pt-C and Pt-Ru material systems, there is no fundamental impediment to applying similar approaches to multicomponent catalyst clusters on various supports as long as appropriate interatomic potentials, preferably of low computational complexity, are available for the systems of interest. In addition, by integrating computationally inexpensive empirical-potential or DFTB based GAs for global structural optimization with DFT modeling for local minimization and electronic structure analyses, we have demonstrated a viable approach for systematic studies of nanocluster catalysis. The findings presented in this thesis can significantly aid rational design of nanoscale catalysts, particularly in the sub-nanometer range where both structural and electronic properties differ fundamentally from those at larger length scales.

5.2 Future Directions

Significant progress has been made in recent years in improving the catalytic performance of Pt nanoparticles in fuel cells thanks to the progress in experimental synthesis technology. Computational modeling, on the other hand, plays an indispensable role in elucidating the fundamental relationships and factors that determines the catalytic performance of Pt clusters, thus supporting experimental design and optimization. However, due to the considerable complexity of coupling between cluster morphology (size and shape), interactions with supports and adsorbates, and presence of alloying elements, there remain several open and interesting questions for future investigation.

As part of this thesis, we have showed that the morphology of Pt clusters, especially in the sub-nanometer regime, has substantial impact on its stability, electronic structure, and adsorption energetics. One interesting possibility for future work is to study how

adsorbates affect the stability of Pt and PtRu clusters. For example, several experimental studies have shown pronounced CO-induced structural changes of Pt clusters, especially for smaller cluster sizes and high CO pressures.¹⁸⁷⁻¹⁹⁰ Currently, such (dynamic) adsorbate-induced restructuring is completely ignored in computational catalysis studies. Therefore, to further bridge the gap between modeling and experiments, we would like to explore the low-energy structures of Pt and PtRu clusters in the presence of CO. Development of accurate and computationally inexpensive models that capture the interactions between CO molecules and Pt clusters is a key prerequisite due to the intricate dependence of CO binding strength on the local environment of surface atoms as well as CO coverage. Subsequently, with the aid of GAs and DFT modeling, the structural stability and catalytic properties of Pt and PtRu clusters at realistic CO coverages can be further explored.

Machine learning is a powerful tool to capture hidden relationships between descriptors and targets. Recently, several research groups have successfully applied machine-learning algorithms to predict the complex, nonlinear interactions between adsorbates and catalysts, however, focusing only on simple crystal surfaces.¹¹⁴⁻¹¹⁵ In this thesis, we showed the promising ability of machine-learning models for rapid estimation of binding energies between CO molecule and Pt clusters. In future work, this method can be extended to predict adsorption energies of CO on PtRu alloy clusters and, more generally, for various adsorbates and metal systems. Such inexpensive yet accurate models can facilitate rapid analysis of reaction pathways and screening of metal catalysts.

Beyond these immediate extensions of the current work, there are still other open problems such as (1) understanding the effect of defect patterns or dopants in graphene supports on the catalytic properties of supported Pt particles, (2) understanding the kinetics

of the key reactions occurring on the surface of Pt nanoclusters with micro-kinetic modeling, and (3) seeking non-precious metal alternatives via computational screening.

APPENDICES

APPENDIX A

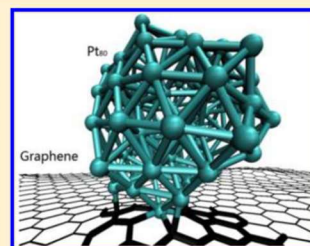
FIRST-PRINCIPLES PREDICATIONS OF STRUCTURE FUNCTION RELATIONSHIPS OF GRAPHENE-SUPPORTED PLATINUM NANOCCLUSERS

First-Principles Predictions of Structure–Function Relationships of Graphene-Supported Platinum Nanoclusters

Hongbo Shi,[†] Scott M. Auerbach,^{*,†,‡} and Ashwin Ramasubramanian^{*,§}[†]Department of Chemical Engineering, [‡]Department of Chemistry, and [§]Department of Mechanical and Industrial Engineering, University of Massachusetts Amherst, Amherst, Massachusetts 01003, United States

Supporting Information

ABSTRACT: Platinum-based materials play an important role as electrocatalysts in energy conversion technologies. Graphene-supported Pt nanoclusters were recently found to be promising electrocatalysts for fuel-cell applications due to their enhanced activity and tolerance to CO poisoning as well as their long-term stability toward sintering. However, structure–function relationships that underpin the improved performance of these catalysts are still not well understood. Here, we employ a combination of empirical potential simulations and density functional theory (DFT) calculations to investigate structure–function relationships of small Pt_N (N = 2–80) clusters on model carbon (graphene) supports. A bond-order empirical potential is employed within a genetic algorithm to go beyond local optimizations in obtaining minimum-energy structures of Pt_N clusters on pristine as well as defective graphene supports. Point defects in graphene strongly anchor Pt clusters and also appreciably affect the morphologies of small clusters, which are characterized via various structural metrics such as the radius of gyration, average bond length, and average coordination number. A key finding from the structural analysis is that the fraction of potentially active surface sites in supported clusters is maximized for stable Pt clusters in the size range of 20–30 atoms, which provides a useful design criterion for optimal utilization of the precious metal. Through selected *ab initio* studies, we find a consistent trend for charge transfer from small Pt clusters to defective graphene supports resulting in the lowering of the cluster d-band center, which has implications for the overall activity and poisoning of the catalyst. The combination of a robust empirical potential-based genetic algorithm for structural optimization with *ab initio* calculations opens up avenues for systematic studies of supported catalyst clusters at much larger system sizes than are accessible to purely *ab initio* approaches.



1. INTRODUCTION

Platinum clusters and nanoparticles are widely used as electrocatalysts and play an important role in the development of clean energy technologies such as hydrogen-based or methanol-based proton-exchange membrane fuel cells.^{1–3} Typically, industrial Pt electrocatalysts are prepared by dispersing Pt powders as small as a few nanometers on conductive carbon black supports,⁴ which results in a high electrocatalytically active surface area. However, it is well-known that traditional Pt/C catalysts are easily poisoned by intermediates, most notably CO, produced during the methanol oxidation reaction at the cathode.^{5–7} In addition, these Pt/C systems suffer from poor long-term stability arising from the corrosion of the carbon support and dissolution or aggregation of Pt on the support surface.^{8–10} Graphene has been shown to be an excellent support for transition-metal-based electrocatalysts, impacting many of the issues above through its strong interactions with a broad range of materials,¹¹ high electronic conductivity,¹² and potential for beneficial modification of the electrochemical properties of supported clusters.¹³ However, Pt/graphene nanostructures remain poorly understood, making it challenging to optimize these electrocatalytic systems. In this article, we apply advanced

optimization methods with force fields benchmarked by first-principles theory to gain insights into Pt/graphene geometrical and electronic structures.

Several experiments have demonstrated the superior performance of Pt/graphene nanocatalysts in direct-methanol fuel cells,^{5,7,14} proton-exchange membrane fuel cells (for the oxygen reduction reaction),¹⁵ and hydrogen fuel cells.¹⁶ Such improved performance has been quantified via metrics such as electrocatalytic activity, tolerance to CO poisoning, and long-term stability toward catalyst sintering. Investigators typically attribute such improvements in catalytic performance to the synergistic interactions between the Pt catalyst and the graphene support, mediated by defects and functional groups in the graphene support that act as strong binding sites for catalyst nanoparticles.^{5,15,17–21} Computational studies corroborate this interpretation and show strong binding of Pt clusters at support defects in graphene, accompanied by a significant modification of the morphology and electronic structure of the clusters.^{9,22–30} In particular, *ab initio* studies indicate a

Received: February 5, 2016

Revised: April 23, 2016

Published: May 19, 2016

noteworthy correlation between the binding energy of a Pt cluster at support defect and the d-band center of cluster, which suggests an additional pathway for optimizing catalytic activity through defect engineering of supports.^{9,28,29} In the present work, we compare pristine and defective graphene supports to better understand how support structure alters Pt/graphene binding properties.

It is well accepted that the structure of catalyst particles plays a significant role in their catalytic performance,^{31,32} and achieving a detailed understanding of structure–activity relationships is hence an issue of much current interest. For example, in recent work Fampiou and Ramasubramaniam⁶ investigated the thermodynamic and electronic properties of Pt₁₃ isomers on graphene supports by examining both high-symmetry cluster morphologies and low-symmetry ones (derived from molecular dynamics annealing). They observed appreciable differences with respect to cluster binding energies on the support, cluster d-band centers, adsorbate binding energies, and overall charge redistribution with different cluster morphologies (isomers). While those studies were limited to a relatively small set of candidate structures, they nevertheless established the need for careful initial selection of cluster morphologies prior to subsequent studies of catalytic reactions on clusters. Indeed, for computational studies of cluster catalysis, it is reasonable to invest initial effort in ascertaining thermodynamically (or kinetically) favored structures, as these are the most probable structures under experimental conditions.³³ While ground-state cluster morphologies might, in principle, be gleaned from experiments, e.g., via fluorescence spectroscopy techniques for vacuum Pt clusters,^{34,35} such studies are extremely challenging and hence limited in number and scope. In contrast, computational studies of the energetics of Pt clusters in vacuum, using both quantum mechanics and empirical potential modeling, are more extensive.^{3,36–42} However, to the best of our knowledge, there are as yet no systematic investigations of the ground-state energetics and morphologies of Pt clusters on graphene supports. In other words, the influence of Pt–graphene binding interactions on cluster morphology and the resulting effects on cluster activity still remain to be systematically understood.

The primary goal of this paper is to present a robust methodology for identifying thermodynamically favorable structures of Pt clusters on graphene supports and to draw clear correlations between cluster energetics and catalytically relevant metrics such as the d-band center and Pt cluster charge transfer. The high-dimensional potential energy surface (PES) for the Pt/graphene system is extremely complex and a brute force search for energy minima at the first-principles level is computationally infeasible. Therefore, we carefully test and validate a Pt–C empirical potential, which we then employ within a genetic algorithm (GA)^{43–45} to facilitate rapid and thorough identification of minimum energy Pt_N ($N = 2–80$) clusters on defect-free and defective graphene supports. Optimized structures are then studied more thoroughly with density functional theory (DFT) calculations to test the structural accuracy and energetic ordering of the empirical potential predictions. Finally, ensembles of unsupported and supported near-minimum energy Pt₁₃ isomers are subjected to detailed electronic structure analyses via DFT calculations to identify clearly the role of support defects and cluster energetics on the potential catalytic activity of the Pt clusters. Overall, by combining an inexpensive empirical potential-based GA with *ab initio* calculations, we establish a tractable approach for

systematic exploration of supported clusters at system sizes that are experimentally relevant and yet inordinately expensive for brute force *ab initio* calculation alone.

2. COMPUTATIONAL METHODS

2.1. Genetic Algorithm for Optimization of Unsupported and Supported Clusters. Structural optimization of nanoparticles/clusters entails the nontrivial task of efficiently identifying the global minimum on a complex PES by performing unbiased sampling. Several global optimization techniques have been developed to address this challenge, including basin-hopping,^{46–50} particle-swarm optimization,^{51,52} and genetic algorithms.^{53,54} In this work, we chose to implement a genetic algorithm⁵⁵ (GA) to determine low-energy structures of unsupported and supported Pt clusters. Local energy optimization was implemented using the LAMMPS package.⁵⁶ In general, the GA produces child clusters from parent clusters by splitting parents in half and cross-mating to form children. At each new generation, local optimization is performed to drain high energies that arise from mating. Promising child clusters then become the parents for the next iteration of the GA, continued until the energies of promising clusters converge within a given tolerance. The specific approach followed here, in particular for optimization of supported clusters, follows the spirit of the pioneering work of Ho and co-workers;⁵⁷ the individual steps of the GA are discussed in detail below.

Initial Population. For a given cluster Pt_N, initial configurations for the starting generations are randomly generated with a minimum Pt–Pt distance of 1.7 Å to avoid biased searching. The distance of 1.7 Å was obtained from numerical testing; of course, no cutoff is necessary, but setting a reasonable one avoids calculating structures that will be rejected due to very short bond lengths. The quality of the *i*th cluster with energy E_i is determined by its fitness f_i , which is calculated by a linear function⁵⁵

$$f_i = 1 - 0.7\rho_i \quad (1)$$

where the scaled energy ρ_i is normalized as

$$\rho_i = (E_i - E_{\min}) / (E_{\max} - E_{\min}) \quad (2)$$

and where E_{\min} and E_{\max} are the lowest and highest energies of the initial configurations. The scaled energy ρ_i for each configuration is thus always between 0 and 1; as such, the fitness values corresponding to the lowest and highest energies are 1.0 and 0.3, respectively.

Selection. A selection operator is used to choose candidates from the current generation for mating. Here, we use the roulette wheel method of selection:⁵⁵ a configuration is chosen at random and selected for mating if its fitness value f_i is greater than a randomly generated number between 0 and 1. Otherwise, another configuration is chosen at random and tested for mating. This process is continued until two configurations are chosen for mating.

Crossover. Crossover refers to the process by which “genetic” information (coordinates) from two parent clusters is combined to generate offspring. The computational approaches for crossovers are quite different for supported and unsupported clusters. For unsupported (vacuum) clusters, the centroids of the two parent clusters are shifted to the origin, after which the parents are subjected to random rotations. The plane at $z = 0$ is used to cut each parent cluster into two parts;

the top half of parent 1 and bottom half of parent 2 are then “glued” together to form a new child. (To conserve particle number between parents and offspring, the cutting plane might require a slight offset from the $z = 0$ position.) A minimum separation of 1 Å is maintained between the glued cluster halves to avoid artificially high energies and/or forces on atoms. For supported clusters, in addition to the steps noted above, the child clusters need to be positioned appropriately relative to the graphene sheet. From numerical testing, a minimum cluster–support distance of 2 Å was found to be a good initial guess for rapid convergence.

Natural Selection. In natural evolution, individuals with higher fitness are more likely to survive and pass on their genes. In our GA, clusters with lower energies have higher fitness (eqs 1 and 2) and are chosen with higher probability for reproduction. The energy evaluation is performed using the LAMMPS package. To facilitate rapid initial relaxation of randomly generated offspring, we employ low-temperature molecular dynamics at 100 K for 0.1 ps using a 1 fs time step. Thereafter, conjugate-gradient minimization is performed for a minimum of 100 iterations or until the norm of the energy gradient on each atom is less than 10^{-3} eV/Å. The new offspring is accepted if its energy falls below an acceptance threshold

$$E_{\text{accept}} = E_{\text{min}} + N_{\text{Pt}} \Delta E \quad (3)$$

where E_{min} is the lower energy of the two parents, N_{Pt} is the number of Pt atoms in the cluster, and ΔE is a numerical parameter. The smaller the value of ΔE the more stringent is the acceptance criterion; from numerical testing, $\Delta E = 0.1$ eV was found to be a useful choice for this parameter because this value caused the algorithm to efficiently produce valid ground states. We note that this parameter (ΔE) is system-specific and can be ascertained through a small initial set of calibration runs.

Elite Species. The population size is maintained at 30 individuals throughout the optimization process. To avoid loss of high quality species, within any generation, we always maintain 20% of fittest individuals from the previous generation.

Convergence. The GA was deemed to have converged if the lowest energy clusters in each generation remained unchanged for 20 generations or if the total number of generations exceeded 1000.

2.2. Empirical Potential Models. In this work, we employ a Pt interatomic potential developed by Albe et al.⁵⁸ based on the reactive bond-order Tersoff–Brenner form.⁵⁹ In addition to Pt–Pt interactions, Albe et al.’s potential also incorporates C–C and Pt–C interactions, which makes it ideally suited for describing Pt clusters on carbon supports. In previous work, Fampiou and Ramasubramaniam⁹ showed that the potential of Albe et al. is remarkably accurate relative to DFT in describing supported cluster morphologies, albeit with limited sampling. Here, we carry out a more extensive investigation of the fidelity of this potential for unsupported clusters and show that this potential is generally in very good agreement with DFT structural models. We also perform careful tests of Albe et al.’s potential for supported clusters and demonstrate that the potential is indeed capable of delivering accurate low-energy structures for further electronic structure analyses. All empirical potential simulations are performed using the LAMMPS simulation package.

2.3. Density Functional Theory Calculations. DFT calculations are performed to study the thermodynamic and

electronic properties of selected low-energy structures using the Vienna Ab initio Simulation Package (VASP).^{60,61} Core and valence electrons are described using the projected augmented wave method.^{62,63} The Perdew–Burke–Ernzerhof (PBE)^{64–66} form of the generalized-gradient approximation is employed to describe electron exchange and correlation. A kinetic energy cutoff of 400 eV is used for the plane-wave basis set, and the conjugate gradient algorithm is used to relax ions into their ground state until the force on any atom is smaller than 0.01 eV/Å. Brillouin zone sampling is performed using a single Gamma point for unsupported clusters. For supported clusters (128 C atoms in pristine support), a $2 \times 2 \times 1$ Γ -centered k -point mesh is found to provide accuracy for energy calculations to within 0.5 meV/graphene atom. From convergence tests, at least 10 Å of vacuum is used to eliminate spurious interactions between periodic images of unsupported and/or supported clusters.

2.4. Simulation Procedure. Unsupported Pt_N ($N = 2–80$) clusters are optimized using our GA code employing Albe et al.’s empirical potential. To ensure better sampling, we run three GA simulations for each particle size, and the geometry with the lowest energy from all simulations is chosen as the global minimum. In almost all cases, the geometries obtained at the end of these three simulations are identical, indicating the robustness of GA. We also perform GA optimization of Pt_N ($N = 2–80$) clusters on defect-free (pristine) and defective (vacancy and divacancy defects) graphene supports using Albe et al.’s potential. In all supported cluster calculations, we use an 8×8 graphene supercell (128 C atoms in pristine graphene), which is sufficiently large to eliminate long-ranged interactions between Pt_{80} clusters (the largest clusters studied here). From the converged GA results, various structural properties of clusters such as the radius of gyration, coordination numbers, and average bond lengths are calculated.

By extensive exploration with the GA, we establish an ensemble of minimum and near-minimum energy Pt_N isomers; Pt_{13} isomers are chosen as a convenient example for further investigation with DFT studies. We choose five isomers of Pt_{13} clusters on pristine, vacancy, and divacancy graphene supports. These structures are subjected to additional relaxation in DFT calculations followed by electronic structure analyses.

3. RESULTS AND DISCUSSION

3.1. Structure and Energetics of Unsupported Pt Clusters. Several DFT-based studies have focused on the structure and energetics of unsupported Pt clusters,^{37,67–69} thereby providing a basis for evaluating both the quality of the empirical potential used in this work as well as the robustness of the GA. Thus, we focus first on unsupported clusters and present a critical evaluation of our simulation methods. A common shortcoming in studies of clusters is that the methods for generating low-energy structures do not use global search algorithms, relying instead on less robust techniques such as simulated annealing. Adopting high-symmetry shapes based on geometric shell models is usually incorrect for small transition-metal clusters as has been well documented in the literature.^{37,67,68} Combining global search algorithms, such as GAs, with inexpensive yet reliable empirical potentials thus offers a significant advantage for reliable and efficient sampling of the PES.

Figure 1 displays the lowest energy structures of Pt_N ($N = 2–80$) found by our GA implementation using Albe et al.’s bond-order potential. Figure 1 shows that Pt clusters are planar up to

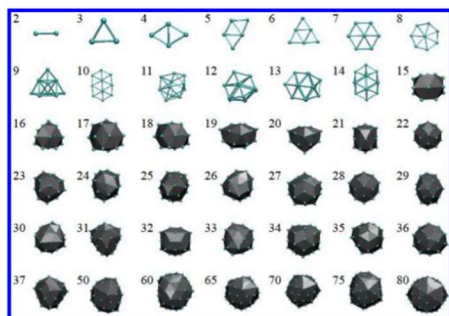


Figure 1. Minimum-energy structures of unsupported Pt clusters as predicted by our GA implementation using Albe et al.'s bond-order potential.

$N = 8$ atoms, which is consistent with the DFT study reported by Kumar et al.³⁷ Furthermore, none of the minimum-energy structures exhibit high symmetry, calling into question common assumptions about enforcing symmetry made in cluster catalysis studies. To examine the accuracy of the empirical potential in greater detail, we focus on $N = 7$ clusters as a specific example. For Pt_7 clusters, the GA predicts a centered six-member ring as the lowest energy structure (see Table 1).

Table 1. Relative Total Energies (in eV) of Pt_7 Isomers from Kumar et al.'s³⁷ and Our DFT Calculations (PBE Functional; PW91 Results in Parentheses) as Well as Albe et al.'s Empirical Potential (EP)^a

Geometry	DFT (Ref. 37)	DFT (this work)	EP
	0.00	0.00 (0.00)	unstable
	0.08	0.07 (0.06)	0.59
	0.12	0.38 (0.07)	0.00

^aEnergies are relative to the lowest energy isomer for each level of theory.

However, both Kumar et al.'s and our DFT results show that side-capped isomers turn out to be lower in energy than the centered ring. Of these side-capped structures, only one is even stable as per the empirical potential (see Table 1), and the energy is appreciably higher (~ 0.6 eV) than that of the centered-ring structure. Of course, the GA prediction can only be as good as the underlying model, and to this extent, the discrepancy between the empirical potential and DFT points to shortcomings of the former. It should be noted, though, that the centered-ring structure is fairly close in energy to the side-capped ground state at the DFT level (within 0.06–0.08 eV).

The efficacy of the combined empirical-potential and DFT approach becomes much more apparent when searching for minimum-energy structures of large clusters. As examples, we consider so-called “magic-number” Pt_{13} , Pt_{55} , Pt_{147} , and Pt_{309} clusters, which have been studied widely in their high-symmetry cuboctahedral (O_h) and icosahedral (I_h) structural motifs.^{40,70,71}

As before, we use the GA to find minimum-energy structures for these various cluster sizes and then further relax the minimum-energy structures in DFT (Figure 2). The energies of

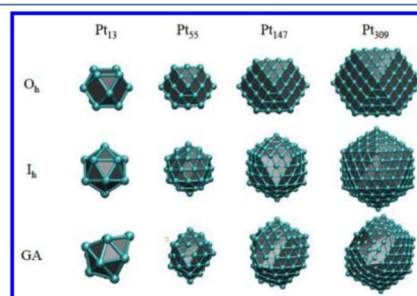


Figure 2. Geometries of low-energy “magic-number” Pt isomers in vacuum. The first two rows display high symmetry cuboctahedral (O_h) and icosahedral (I_h) clusters. The third row displays minimum-energy structures found by the genetic algorithm with an empirical potential.

the DFT-relaxed structures are then compared with corresponding DFT energies for the high-symmetry O_h and I_h structures; total energy differences relative to the minimum-energy structure for each cluster size are reported in Table 2.

Table 2. Relative Total Energies (in eV) of High-Symmetry (Cuboctahedral: O_h ; Icosahedral: I_h) Pt Clusters and GA-Optimized, Low-Energy Clusters Calculated Using DFT and Albe et al.'s Empirical Potential (EP)^a

	Pt_{13}		Pt_{55}		Pt_{147}		Pt_{309}	
	DFT	EP	DFT	EP	DFT	EP	DFT	EP
I_h	1.3	1.7	3.3	3.4	6.5	5.1	7.7	5.6
O_h	2.0	1.8	5.1	6.4	8.2	12.4	9.7	18.4
GA	0.0	0.0	0.0	0.0	0.0	0.0	0.0	0.0

^aEnergies are relative to the lowest energy isomer for each size and level of theory.

These results show clearly that the high-symmetry structures are not the lowest-energy structures, as was also shown in previous DFT studies of Pt_{13} and Pt_{55} clusters.^{40,69} Indeed, the results obtained here for larger clusters are particularly striking and prompt interesting questions regarding typical sizes at which transitions from low-symmetry to high-symmetry clusters may be expected to occur in faceted crystals of Pt nanoclusters; such issues will be discussed elsewhere.

It is also apparent from these results that the performance of Albe et al.'s empirical potential—in terms of relative energetic ordering of structures—is surprisingly good when compared with DFT calculations, especially considering that the potential was parametrized for bulk properties. The lowest-energy structures found by the GA essentially resemble defective icosahedra that are approximately 0.01–0.1 eV/atom lower in energy (across the entire range of sizes) than the perfect icosahedra. Cuboctahedral structures are in general higher in energy than both the GA-optimized structures and the perfect icosahedra.

Overall, the benchmarking studies presented here lead us to two principal conclusions. First, Albe et al.'s bond-order

potential is of sufficient accuracy to deliver near-minimum energy structures of unsupported clusters, which can then be subjected to additional optimization in DFT calculations. Second, our GA implementation is able to deliver reliable minimum-energy results for unsupported clusters, which then lends us confidence in proceeding to the study of supported clusters, the primary target of this work and the subject of the next discussion.

3.2. Structure and Energetics of Graphene-Supported Pt Clusters. We now consider the energetics of Pt_N clusters on graphene supports. As model supports, we use graphene sheets that are either defect-free (pristine) or sheets that contain point defects (vacancies and divacancies). Point defects in graphene are known to act as strong anchoring sites for nanoclusters and have also been shown to modify the electronic structure and catalytic activity of small clusters.^{9,28,29} The metrics we adopt for thermodynamic comparisons are the cluster adsorption energy and the overall formation energy of the composite Pt/graphene system. The adsorption energy (E_{ad}) is defined as

$$E_{ad} = E_{Pt_N+Gr} - E_{Pt_N} - E_{Gr} \quad (4)$$

where E_{Pt_N+Gr} is the total energy of the Pt/graphene system, E_{Pt_N} is the total energy of the Pt_N cluster without the support, and E_{Gr} is the total energy of the (pristine/defective) graphene sheet. The overall formation energy of the composite Pt/graphene system (E_f) is defined as

$$E_f = E_{Pt_N+Gr} - ME_C - NE_{Pt} \quad (5)$$

where E_{Pt_N+Gr} is the total energy of the Pt/graphene system, E_{Pt} is the energy of an isolated Pt atom in vacuum, E_C is the energy of a single C atom in graphene, and M and N are the number of C and Pt atoms, respectively.

First, to test the performance of our GA, we study supported Pt_N ($N = 2, 3, 4, 13$) clusters and compare our results with those of Fampiou and Ramasubramanian,⁹ who also used Albe et al.'s bond-order potential but adopted a molecular dynamics (MD) annealing scheme for energy minimization. The formation energies for Pt_N ($N = 2, 3, 4, 13$) clusters with pristine and defective graphene supports are reported in Table 3, and the corresponding structures (from the GA) are

Table 3. Formation Energies (eV) of Minimum-Energy Pt Clusters on Pristine and Defective (Vacancy, Divacancy) Graphene Supports Identified Using the GA and by Molecular-Dynamics-Based Annealing (Ref 9)

	pristine		vacancy		divacancy	
	GA	annealing	GA	annealing	GA	annealing
Pt_2	-5.75	-5.62	-5.33	-5.30	-5.59	-5.25
Pt_3	-10.11	-10.06	-9.55	-8.73	-9.88	-8.38
Pt_4	-14.24	-13.12	-13.80	-11.69	-14.13	-13.80
Pt_{13}	-55.50	-55.20	-55.16	-55.14	-55.65	-55.67

displayed in Figure 3. For additional comparison, we also report formation energies calculated using the empirical potential in the Supporting Information (Table S1). In all cases, the GA delivers structures with lower formation energies than the MD annealing results previously reported. The differences are particularly noticeable for few-atom clusters. In the Pt_2 case, the GA produces ground states consisting of dimer orientations parallel to the surface on pristine and defective graphene supports. MD-based annealing consistently generates

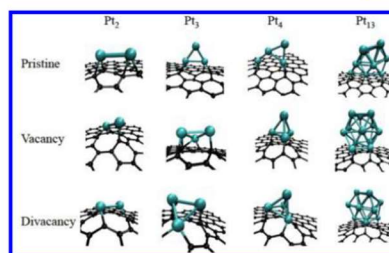


Figure 3. Minimum-energy structures of Pt_N ($N = 2, 3, 4, 13$) on pristine graphene (upper row) and graphene with single vacancy (middle row) and divacancy defects (bottom row).

local minima with vertically oriented Pt dimers on pristine graphene; on defective graphene, the dimers lie parallel to the support. For Pt_3 clusters on pristine graphene, both GA and MD annealing find the vertical triangle as the ground state; on defective graphene, the GA finds structures that are appreciably more stable by 1.0–1.5 eV than those from MD annealing. For Pt_4 clusters, the GA finds a planar cluster that is nearly vertically oriented to the pristine graphene sheet as the minimum-energy structure; a tetrahedron is the most stable structure on defective graphene supports. The MD annealing algorithm is again stuck in various local minima at higher energies. Finally, for Pt_{13} clusters on graphene supports, Fampiou and Ramasubramanian showed that the clusters prefer more open structures instead of high-symmetry ones (I_h or O_h); the GA results confirm those findings, and the minimum-energy structures are also energetically very close to those found by MD annealing. It thus appears that clusters with very small number of atoms present pathological challenges for the MD annealing procedure, in particular, capturing the precise orientation and location of cluster atoms on the support. With increasing cluster sizes, the energetics appear to be dominated by the inherent morphology of the cluster itself, with orientational effects relative to the support being of lesser importance. In any case, it is clear that a global minimization algorithm, such as a GA, performs more reliably at finding ground states than *ad hoc* procedures such as simulated annealing.

Next, we study the properties of supported Pt_N clusters over the size range $N = 2$ –80 analogous to the unsupported cluster studies. In addition to thermodynamic properties such as adsorption and formation energies, we also thoroughly characterize the structural properties of clusters through metrics such as the radius of gyration, average coordination number, average bond lengths, and fraction of (potentially) catalytically active surface atoms, which are variously displayed in Figure 4. Note that while the catalytic activity of a site on a crystalline facet (terrace, step, edge, kink) or on a large nanoparticle (face, edge, corner) can vary significantly due to local coordination, the nanoclusters considered here are too small to display such distinguishing morphological features. Thus, we focus on understanding average properties of surface sites throughout this work. The various configurations studied here are all minimum-energy structures obtained via the GA.

Figure 4a displays the radius of gyration (R_g) of Pt_N clusters with and without the graphene support. As seen, R_g tends to be noticeably higher for unsupported clusters and clusters on pristine graphene supports relative to those on defective

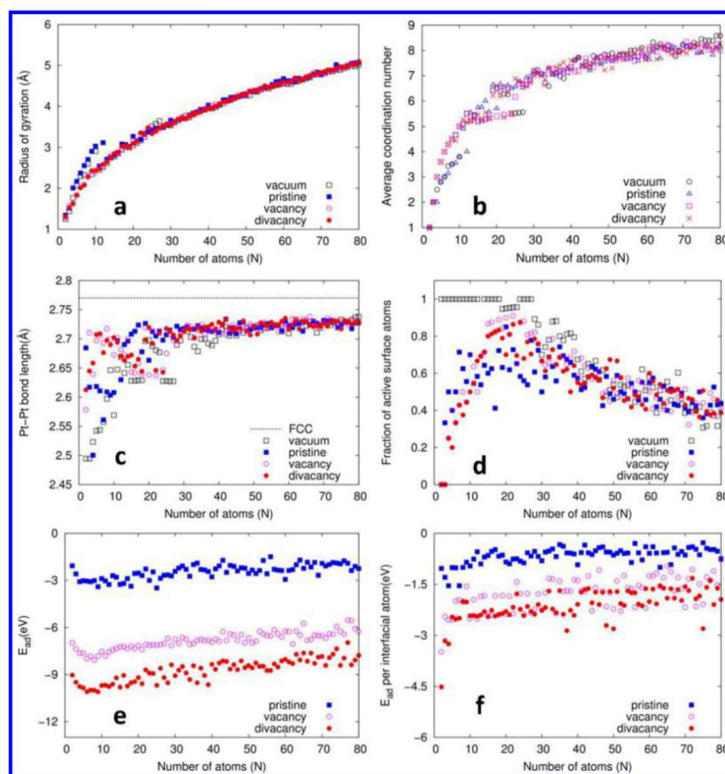


Figure 4. Evolution of structural and energetic properties of global minima of Pt_N /graphene calculated using the genetic algorithm as a function of particle number N : (a) radius of gyration; (b) average coordination number of Pt atoms (excluding Pt–C bonds); (c) average Pt–Pt bond length (dashed line is for bulk FCC Pt); (d) fraction of active surface atoms, defined in eq 6; (e) adsorption energy (E_{ad}) of Pt clusters on graphene; (f) average contribution of Pt atoms at the Pt–C interface to E_{ad} .

supports up to $N = 12$. This is due to 2D morphologies being preferable both in vacuum and on pristine graphene supports at these cluster sizes; the presence of point defects in the graphene support favors 3D structures beginning from the smallest possible size, Pt_4 , as seen in Figure 3. For $N \geq 13$, the support effect on cluster morphology is negligible— R_g is approximately the same for supported as well as unsupported clusters. Physically, this result suggests that the Pt–C contribution to the total energy becomes less important compared with the Pt–Pt interaction for larger clusters.

Another important structural metric used to characterize clusters is the atomic coordination number; Figure 4b displays the average coordination number (Z_{avg}) of Pt atoms as a function of cluster size. The precise number of neighbors of an atom is sensitive to the cutoff distance chosen for bond counting, and for consistency, we use the same cutoff distance as that for Pt–Pt interactions in the bond-order potential (3.3 Å). As seen from Figure 4b, the average coordination number increases monotonically with cluster size, as is to be expected due to the increase in the bulk-to-surface ratio. For the range of

clusters studied here, $Z_{avg} = 8$ is the largest value attained; for reference, we recall that the coordination number of atoms on the Pt(111) surface is 9 while that in the bulk is 12. This significant overall degree of undercoordination is to be expected for such small clusters that are mostly “surface” rather than “bulk”. Our calculations show that the smallest cluster size for which at least one atom has a coordination number of 12 is $N = 19$.

Figure 4c offers insight complementary to this analysis of coordination numbers by displaying the average Pt–Pt bond length (a_{avg}) in the unsupported and supported Pt clusters; the horizontal dashed line in that figure indicates the bulk, FCC Pt–Pt bond length (2.77 Å) for comparison. The average Pt–Pt bond decreases in length with decreasing cluster size, which once again reflects the increase in the ratio of surface to bulk atoms as undercoordinated surface atoms exhibit shorter bonds to compensate for having fewer neighbors. The trends for a_{avg} are similar for unsupported clusters and for those on pristine graphene supports, especially at small cluster sizes, reflecting the relatively small role of the support in the absence of strong

perturbations such as those arising from point defects. Again, for larger clusters, the differences in a_{avg} are small, thus reflecting the relatively minor role of the support on cluster morphology. For the range of cluster sizes studied here, a_{avg} is still about 0.1 Å smaller than the bulk FCC value. There are some systematic deviations in the monotonic growth of Z_{avg} and a_{avg} in the $N = 20$ –40 as seen from Figures 4b and 4c. Closer visual inspection of these clusters leads us to attribute the fluctuations to a competition between hollow-core and filled-center cluster morphologies.

A structural property of interest and immediate relevance to cluster catalysis is the number of potentially active Pt atoms on the cluster surface. Atoms within the interior of the cluster do not directly participate in surface reactions, and we also assume that atoms directly bonded to the support are less likely to participate in surface reactions due to constraints arising from e.g. steric hindrance and possibly from electronic effects (saturation of dangling bonds). There are of course exceptions to such criteria, notably for single-site catalysts bound at point defects in graphene,^{72,73} but these are essentially pathological cases and the proposed criterion is both intuitively appealing and physically reasonable for larger clusters. Thus, we define the fraction of active surface atoms ($f_{\text{Pt}}^{\text{surf}}$) as

$$f_{\text{Pt}}^{\text{surf}} = (N_{\text{Pt}}^{\text{surf}} - N_{\text{Pt}}^{\text{C}})/N_{\text{Pt}} \quad (6)$$

where $N_{\text{Pt}}^{\text{surf}}$ is the number of atoms on the surface of the Pt cluster and N_{Pt}^{C} is the number of Pt atoms bonded to the support. Various criteria may be established for identifying a “surface” atom; we do so here by assigning an atom with six or fewer neighbors to be a surface atom. Visual inspection of several clusters confirms the validity of this coordination number cutoff. As seen from Figure 4d, $f_{\text{Pt}}^{\text{surf}}$ displays rather interesting behavior. For unsupported clusters all atoms are on the surface for $N < 19$; for larger unsupported clusters, most of the Pt atoms are in the bulk and consequently are not active. For supported clusters, the fraction of active sites is initially small as many Pt atoms are bonded directly to the graphene support; at large cluster sizes, most of the Pt atoms are again in the bulk and are consequently not active. The optimal value for $f_{\text{Pt}}^{\text{surf}}$ is achieved in the range $N = 20$ –30 irrespective of the presence or absence of the support defects. This is a key result as it identifies an optimal range of cluster sizes that maximally utilizes the precious metal catalyst; to the best of our knowledge, this result has not been reported before and, in particular, not for supported Pt clusters.

Finally, Figures 4e and 4f display the total adsorption energy and adsorption energy per interfacial Pt atom for supported Pt_N clusters. It is clear that point defects in the graphene support bind Pt clusters more strongly than does pristine graphene across the entire range of cluster sizes; divacancies are also seen to be stronger binding sites than vacancies due to a higher number of dangling bonds. In general, the variation in adsorption energies with cluster size is rather small; similar results were reported by Ramos-Sanchez et al.,⁷⁴ who used DFT calculations to study clusters on graphite in the range of $N = 1$ –38. The slight decrease in binding strength (less negative adsorption energies) with increasing cluster sizes (beyond $N = 10$) is indicative of weaker trapping of larger clusters by the vacancy/divacancy, thus suggesting the need for larger support defects to improve the stability of larger Pt clusters against aggregation.

3.3. Electronic Structure of Pt_{13} Isomers. It is well-known that chemisorption of adsorbates on transition metal surfaces is strongly correlated with the so-called d-band center energy of the surface.⁷⁵ Several studies have now extended this metric to the study of supported clusters and shown similar correlations.^{27,29,76} In particular, the influence of cluster morphology as well as the role of the support in modulating the d-band center energy are issues of current interest for rational catalyst design. Our ability to produce low-energy isomers at low computational expense using the GA now allows us to examine more broadly the issues of cluster morphology and support effects on the catalytic activity of clusters (beyond the limited cases studied in our previous work^{9,29}). As an example, we focus here on Pt_{13} clusters; more comprehensive studies across a range of cluster sizes will be reported elsewhere.

Using the GA, we identified several Pt_{13} isomers within a 30 meV/atom energy window close to the global minimum for Pt_{13} in vacuum or with various support types. All candidates, supported or otherwise, were imported into VASP and subjected to conjugate-gradient structural relaxation. For vacuum Pt_{13} isomers, an additional 15 candidates were obtained by simply eliminating the support from the low-energy Pt_{13} /graphene systems and relaxing the residual Pt_{13} cluster; such clusters are merely local rather than global minima, but including these in our analyses gives us a larger statistical sample for studying structure–property correlations. From the angular-momentum-projected density of states, we compute the d-band center energy (ϵ_d) as

$$\epsilon_d = \frac{\int \rho E \, dE}{\int \rho \, dE} \quad (7)$$

where E is energy of each state and ρ is the corresponding density of d-states. Figure 5a displays d-band center energies as a function of cluster adsorption energy and formation energy for supported and unsupported clusters, respectively. For unsupported clusters, the d-band center energy varies almost linearly with the formation energy and spans about 0.1 eV within a formation energy window of width 0.2 eV/atom. In the presence of the graphene support, ϵ_d can be significantly lowered, especially in the presence of vacancy and divacancy defects, and once again the lowering of the d-band center is correlated with the adsorption energy, which was also noted earlier by Fampiou and Ramasubramanian.⁹ In general, for the various clusters on defective supports, we find that when a Pt atom occupies the center of the defect (vacancy/divacancy), the total energy as well as the adsorption energy decrease significantly, as indicated by the points within the dashed square in Figure 5a; this decrease in adsorption energy is accompanied by a drop in the d-band center energy. Furthermore, for all cases of clusters on defective supports, the d-band center lies slightly below that for $\text{Pt}(111)$, suggesting comparable or possibly weaker adsorbate binding. In the absence of point defects, the cluster d-band center approximately coincides with the calculated value for $\text{Pt}(111)$; for unsupported clusters, the d-band centers are appreciably higher than that for $\text{Pt}(111)$.

As noted in prior work,^{9,27} the total charge transferred from the cluster to graphene is an important factor in shifting the cluster d-band center. Thus, we also perform a Bader charge analysis^{77,78} to evaluate the total charge transferred from the cluster to the graphene support. Figure 5b displays the transferred charge with respect to the adsorption energy, and

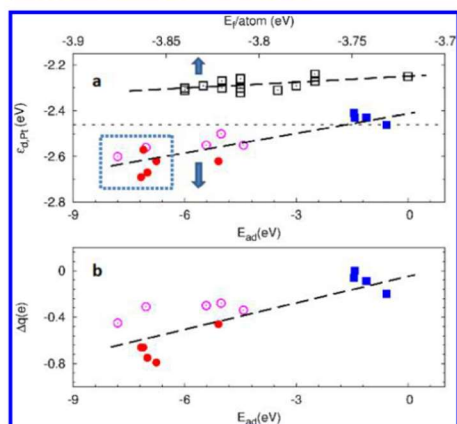


Figure 5. Position of d-band center (ϵ_{dPt}) relative to the Fermi level (a) and net charge transferred (b) to Pt_{13} isomers in vacuum and on graphene support. Data for Pt_{13} clusters in vacuum and on support are plotted with respect to the formation energy (E_f) per atom and the adsorption energy (E_{ad}), respectively. The horizontal dashed line represents ϵ_{dPt} for the Pt(111) surface. Other dashed lines are guides to the eyes. Points inside dashed square correspond to structures with Pt atoms occupying the center of the defect.

the trends are similar to that of the d-band analysis. Similar to previous reports,⁹ we observe that stronger binding of clusters to the support results in greater depletion of charge from the cluster, which then leads to a lowering of the d-band center of the cluster. A complementary and chemically intuitive view of bonding at the Pt–C interface can also be obtained from a natural bond orbital (NBO) analysis,^{79,80} which we present in the Supporting Information. Broadly speaking, the NBO analysis does not show any significant bonding between Pt_{13} clusters and pristine graphene; for the defective graphene supports, a predominantly covalent nature is found for C–Pt bonds at the defect center with clear polarization toward the C atoms, which bolsters the picture of charge transfer from Pt to graphene obtained from the Bader analysis.

The electronic structure analysis presented here is essentially in agreement with previous work by Fampiou and Ramasubramanian,⁹ among others,²⁷ although with much better statistics and more careful attention to computational procedures for generating low-energy structures. The role of the support is relatively clear in our studies: defective supports appreciably lower the d-band centers, at least of small Pt clusters, and consequently have implications for adsorbate binding and reaction barriers.^{28,29} In terms of proper selection of structures for electronic structure analyses and/or studies of reaction pathways, it would appear that small deviations from the minimum-energy cluster morphology are unlikely to lead to large deviations in the energies of the surface states at least for small clusters. Thus, we expect that any reasonably robust method for generating low-energy morphologies ought to result in plausible predictions of catalytic behavior from subsequent electronic structure studies.

Finally, data for adsorption energies of several clusters of varying sizes on defective and defect-free graphene supports are

displayed in the Supporting Information (Figure S1), as are the charge transfer data associated with these various cases (Figure S2). As shown there, the adsorption energy of Pt_N clusters to the graphene supports increases weakly (i.e., binding becomes less strong) with increasing cluster size. Associated with this inverse correlation between adsorption energy and cluster size, we also see that the extent of charge transfer is also reduced at larger cluster sizes. Additional electronic structure analyses to investigate these results with more extensive statistical sampling are underway and will be reported elsewhere.

4. CONCLUSIONS

We have implemented an empirical-potential-based genetic algorithm for structural optimization of unsupported and supported Pt nanoclusters. Using a bond-order potential for the Pt–C system developed by Albe et al., we explored the morphological properties of Pt_N ($N = 2–80$) clusters considering unsupported clusters as well as those supported on pristine or defective graphene supports. A key finding from the structural analysis is that the fraction of potentially active surface sites for supported Pt clusters is maximal for 20–30 atom clusters irrespective of the presence or absence of support defects; this result provides a useful synthetic target for optimal utilization of the precious metal catalyst. Selected ground-state clusters from the GA process were subjected to structural relaxation with DFT calculations and compared with corresponding high-symmetry icosahedral and cuboctahedral clusters. For all “magic number” clusters, the GA optimization process produced cluster morphologies that are lower in energy than their high-symmetry counterparts (at both the empirical potential and DFT levels). The inclusion of the graphene support is found to influence cluster morphologies at very small sizes; beyond ~ 10 atoms, the cluster morphology is essentially dominated by Pt–Pt interactions with minimal perturbations from the support, at least for the cases considered here with small point defects in the support. The effect of the support—more precisely support defects—on the electronic properties of Pt clusters is more pronounced. For the cases of supported Pt_{13} clusters studied here, the cluster d-band energy is downshifted relative to the Fermi level in direct proportion to the strength of binding of the cluster to the support. Cluster adsorption energies on the support and the attendant d-band shifts are sensitive to the precise details of bonding at the cluster–support interface, especially for small clusters, requiring careful structural optimization.

By integrating computationally inexpensive empirical-potential-based GAs for global structural optimization with DFT modeling for local minimization and electronic structure analyses, we have demonstrated a viable approach for systematic studies of supported catalyst nanoclusters. While this work was restricted to the Pt–C system, there is no fundamental impediment to applying similar approaches to multicomponent catalyst clusters on various supports as long as appropriate interatomic potentials, preferably of low computational complexity, are available for the systems of interest. Advances along such directions for supported alloy nanoclusters will be reported in future work.

■ ASSOCIATED CONTENT

Supporting Information

The Supporting Information is available free of charge on the ACS Publications website at DOI: 10.1021/acs.jpcc.6b01288.

DFT calculations of adsorption energies of Pt_N (*N* = 20–80) clusters on graphene; comparison of DFT vs bond-order potential formation energies of Pt–graphene composite systems; natural bond orbital analysis of Pt₁₃ clusters adsorbed at vacancy and divacancy defects in graphene (PDF)

AUTHOR INFORMATION

Corresponding Authors

*E-mail: auerbach@chem.umass.edu (S.M.A.).

*E-mail: ashwin@engin.umass.edu (A.R.).

Notes

The authors declare no competing financial interest.

ACKNOWLEDGMENTS

H.S. and A.R. gratefully acknowledge research funding from the U.S. Department of Energy under Award DE-SC0010610. Computational resources were provided by the Massachusetts Green High Performance Computing Center and also by the National Energy Research Scientific Computing Center, which is supported by the Office of Science of the U.S. Department of Energy under Contract DE-AC02-05CH11231.

REFERENCES

- (1) Yu, X. W.; Ye, S. Y. Recent advances in activity and durability enhancement of Pt/C catalytic cathode in PEMFC - Part I. Physicochemical and electronic interaction between Pt and carbon support, and activity enhancement of Pt/C catalyst. *J. Power Sources* **2007**, *172*, 133–144.
- (2) Zhang, S. S.; Yuan, X. Z.; Hin, J. N. C.; Wang, H. J.; Friedrich, K. A.; Schulze, M. A review of platinum-based catalyst layer degradation in proton exchange membrane fuel cells. *J. Power Sources* **2009**, *194*, 588–600.
- (3) Antolini, E.; Salgado, J. R. C.; Gonzalez, E. R. The stability of Pt-M (*M* = first row transition metal) alloy catalysts and its effect on the activity in low temperature fuel cells - A literature review and tests on a Pt-Co catalyst. *J. Power Sources* **2006**, *160*, 957–968.
- (4) Song, W. Y.; Chen, Z. X.; Yang, C.; Yang, Z. P.; Tai, J. P.; Nan, Y. L.; Lu, H. B. Carbon-coated, methanol-tolerant platinum/graphene catalysts for oxygen reduction reaction with excellent long-term performance. *J. Mater. Chem. A* **2015**, *3*, 1049–1057.
- (5) Li, Y. J.; Gao, W.; Ci, L. J.; Wang, C. M.; Ajayan, P. M. Catalytic performance of Pt nanoparticles on reduced graphene oxide for methanol electro-oxidation. *Carbon* **2010**, *48*, 1124–1130.
- (6) Wen, Z. H.; Liu, J.; Li, J. H. Core/shell Pt/C nanoparticles embedded in mesoporous carbon as a methanol-tolerant cathode catalyst in direct methanol fuel cells. *Adv. Mater.* **2008**, *20*, 743–747.
- (7) Yoo, E.; Okata, T.; Akita, T.; Kohyama, M.; Nakamura, J.; Honma, I. Enhanced Electrocatalytic Activity of Pt Subnanoclusters on Graphene Nanosheet Surface. *Nano Lett.* **2009**, *9*, 2255–2259.
- (8) Shao, Y. Y.; Wang, J.; Kou, R.; Engelhard, M.; Liu, J.; Wang, Y.; Lin, Y. H. The corrosion of PEM fuel cell catalyst supports and its implications for developing durable catalysts. *Electrochim. Acta* **2009**, *54*, 3109–3114.
- (9) Fampiou, I.; Ramasubramaniam, A. Binding of Pt Nanoclusters to Point Defects in Graphene: Adsorption, Morphology, and Electronic Structure. *J. Phys. Chem. C* **2012**, *116*, 6543–6555.
- (10) Yu, X. W.; Ye, S. Y. Recent advances in activity and durability enhancement of Pt/C catalytic cathode in PEMFC - Part II: Degradation mechanism and durability enhancement of carbon supported platinum catalyst. *J. Power Sources* **2007**, *172*, 145–154.
- (11) Park, S.; Ruoff, R. S. Chemical methods for the production of graphenes. *Nat. Nanotechnol.* **2009**, *4*, 217–224.
- (12) Yang, J.; Zang, C. L.; Sun, L.; Zhao, N.; Cheng, X. N. Synthesis of graphene/Ag nanocomposite with good dispersibility and electroconductivity via solvothermal method. *Mater. Chem. Phys.* **2011**, *129*, 270–274.
- (13) Wang, C. M.; Ma, L.; Liao, L. W.; Bai, S.; Long, R.; Zuo, M.; Xiong, Y. J. A unique platinum-graphene hybrid structure for high activity and durability in oxygen reduction reaction. *Sci. Rep.* **2013**, *3*, 2580.
- (14) Huang, H. J.; Chen, H. Q.; Sun, D. P.; Wang, X. Graphene nanoplate-Pt composite as a high performance electrocatalyst for direct methanol fuel cells. *J. Power Sources* **2012**, *204*, 46–52.
- (15) Kou, R.; et al. Enhanced activity and stability of Pt catalysts on functionalized graphene sheets for electrocatalytic oxygen reduction. *Electrochim. Commun.* **2009**, *11*, 954–957.
- (16) Seger, B.; Kamat, P. V. Electrocatalytically Active Graphene-Platinum Nanocomposites. Role of 2-D Carbon Support in PEM Fuel Cells. *J. Phys. Chem. C* **2009**, *113*, 7990–7995.
- (17) Tang, Y. N.; Yang, Z. X.; Dai, X. Q. Trapping of metal atoms in the defects on graphene. *J. Chem. Phys.* **2011**, *135*, 224704.
- (18) Rodriguez-Manzo, J. A.; Cretu, O.; Banhart, F. Trapping of Metal Atoms in Vacancies of Carbon Nanotubes and Graphene. *ACS Nano* **2010**, *4*, 3422–3428.
- (19) Gan, Y. J.; Sun, L. T.; Banhart, F. One- and two-dimensional diffusion of metal atoms in graphene. *Small* **2008**, *4*, 587–591.
- (20) Wu, G. H.; Huang, H.; Chen, X. M.; Cai, Z. X.; Jiang, Y. Q.; Chen, X. Facile synthesis of clean Pt nanoparticles supported on reduced graphene oxide composites: Their growth mechanism and tuning of their methanol electro-catalytic oxidation property. *Electrochim. Acta* **2013**, *111*, 779–783.
- (21) He, D. P.; Cheng, K.; Li, H. G.; Peng, T.; Xu, F.; Mu, S. C.; Pan, M. Highly Active Platinum Nanoparticles on Graphene Nanosheets with a Significant Improvement in Stability and CO Tolerance. *Langmuir* **2012**, *28*, 3979–3986.
- (22) Tang, Y. A.; Yang, Z. X.; Dai, X. Q. A theoretical simulation on the catalytic oxidation of CO on Pt/graphene. *Phys. Chem. Chem. Phys.* **2012**, *14*, 16566–16572.
- (23) Durbin, D. J. D.; Malardier-Jugroot, C. Density Functional Theory Analysis of Metal/Graphene Systems As a Filter Membrane to Prevent CO Poisoning in Hydrogen Fuel Cells. *J. Phys. Chem. C* **2011**, *115*, 808–815.
- (24) Zhou, M.; Zhang, A. H.; Dai, Z. X.; Zhang, C.; Feng, Y. P. Greatly enhanced adsorption and catalytic activity of Au and Pt clusters on defective graphene. *J. Chem. Phys.* **2010**, *132*, 194704.
- (25) Kim, G.; Jhi, S. H. Carbon Monoxide-Tolerant Platinum Nanoparticle Catalysts on Defect-Engineered Graphene. *ACS Nano* **2011**, *5*, 805–810.
- (26) Lim, D. H.; Wilcox, J. Mechanisms of the Oxygen Reduction Reaction on Defective Graphene-Supported Pt Nanoparticles from First-Principles. *J. Phys. Chem. C* **2012**, *116*, 3653–3660.
- (27) Lim, D. H.; Wilcox, J. DFT-Based Study on Oxygen Adsorption on Defective Graphene-Supported Pt Nanoparticles. *J. Phys. Chem. C* **2011**, *115*, 22742–22747.
- (28) Fampiou, I.; Ramasubramaniam, A. Influence of Support Effects on CO Oxidation Kinetics on CO-Saturated Graphene-Supported Pt-13 Nanoclusters. *J. Phys. Chem. C* **2015**, *119*, 8703–8710.
- (29) Fampiou, I.; Ramasubramaniam, A. CO Adsorption on Defective Graphene-Supported Pt-13 Nanoclusters. *J. Phys. Chem. C* **2013**, *117*, 19927–19933.
- (30) Okamoto, Y. Density-functional calculations of icosahedral M-13 (*M* = Pt and Au) clusters on graphene sheets and flakes. *Chem. Phys. Lett.* **2006**, *420*, 382–386.
- (31) Zhang, L.; Anderson, R. M.; Crooks, R. M.; Henkelman, G. Correlating Structure and Function of Metal Nanoparticles for Catalysis. *Surf. Sci.* **2015**, *640*, 65–72.
- (32) Smith, G. V.; Tjandra, S.; Musoiu, M.; Wiltowski, T.; Notheisz, F.; Bartok, M.; Hannus, I.; Ostgard, D.; Malhotra, V. Modified activities and selectivities of silated-oxidized-reduced Pd and Pt catalysts. *J. Catal.* **1996**, *161*, 441–450.
- (33) Hartke, B. Global cluster geometry optimization by a phenotype algorithm with niches: Location of elusive minima, and low-order scaling with cluster size. *J. Comput. Chem.* **1999**, *20*, 1752–1759.

- (34) Airola, M. B.; Morse, M. D. Rotationally resolved spectroscopy of Pt-2. *J. Chem. Phys.* **2002**, *116*, 1313–1317.
- (35) Fabbì, J. C.; Langenberg, J. D.; Costello, Q. D.; Morse, M. D.; Karlsson, L. Dispersed fluorescence spectroscopy of jet-cooled AgAu and Pt-2. *J. Chem. Phys.* **2001**, *115*, 7543–7549.
- (36) Wang, X. L.; Tian, D. X. Structures and structural evolution of Pt-*n* (*n* = 15–24) clusters with combined density functional and genetic algorithm methods. *Comput. Mater. Sci.* **2009**, *46*, 239–244.
- (37) Kumar, V.; Kawazoe, Y. Evolution of atomic and electronic structure of Pt clusters: Planar, layered, pyramidal, cage, cubic, and octahedral growth. *Phys. Rev. B: Condens. Matter Mater. Phys.* **2008**, *77*, 205418.
- (38) Sebetci, A.; Guvenc, Z. B. Global minima of Al(*N*), Au(*N*) and Pt(*N*), *N* ≤ 80, clusters described by the Voter-Chen version of embedded-atom potentials. *Modell. Simul. Mater. Sci. Eng.* **2005**, *13*, 683–698.
- (39) Sebetci, A.; Guvenc, Z. B. Global minima for free Pt-*N* clusters (*N* = 22–56): a comparison between the searches with a molecular dynamics approach and a basin-hopping algorithm. *Eur. Phys. J. D* **2004**, *30*, 71–79.
- (40) Xiao, L.; Wang, L. C. Structures of platinum clusters: Planar or spherical? *J. Phys. Chem. A* **2004**, *108*, 8605–8614.
- (41) Sebetci, A.; Guvenc, Z. B. Energetics and structures of small clusters: Pt(*N*), *N* = 2–21. *Surf. Sci.* **2003**, *525*, 66–84.
- (42) Tian, W. Q.; Ge, M. F.; Sahu, B. R.; Wang, D. X.; Yamada, T.; Mashiko, S. Geometrical and electronic structure of the Pt-7 cluster: A density functional study. *J. Phys. Chem. A* **2004**, *108*, 3806–3812.
- (43) Pittaway, F.; Paz-Borbon, L. O.; Johnston, R. L.; Arslan, H.; Ferrando, R.; Mottet, C.; Barcaro, G.; Fortunelli, A. Theoretical Studies of Palladium-Gold Nanoclusters: Pd-Au Clusters with up to 50 Atoms. *J. Phys. Chem. C* **2009**, *113*, 9141–9152.
- (44) Borbon-Gonzalez, D. J.; Pacheco-Contreras, R.; Posada-Amarillas, A.; Schon, J. C.; Johnston, R. L.; Montejano-Carrizales, J. M. Structural Insights into 19-Atom Pd/Pt Nanoparticles: A Computational Perspective. *J. Phys. Chem. C* **2009**, *113*, 15904–15908.
- (45) Chen, F. Y.; Johnston, R. L. Structure and spectral characteristics of the nanocluster Ag₃Au₁₀. *Appl. Phys. Lett.* **2007**, *90*, 153123.
- (46) Priest, C.; Tang, Q.; Jiang, D. E. Structural Evolution of Tc-*n* (*n* = 4–20) Clusters from First-Principles Global Minimization. *J. Phys. Chem. A* **2015**, *119*, 8892–8897.
- (47) Arslan, H. Structures and energetic of Palladium-Cobalt binary clusters. *Int. J. Mod. Phys. C* **2008**, *19*, 1243–1255.
- (48) Gould, A. L.; Heard, C. J.; Logsdail, A. J.; Catlow, C. R. A. Segregation effects on the properties of (AuAg)₁₄₇. *Phys. Chem. Chem. Phys.* **2014**, *16*, 21049–21061.
- (49) Ouyang, R. H.; Xie, Y.; Jiang, D. E. Global minimization of gold clusters by combining neural network potentials and the basin-hopping method. *Nanoscale* **2015**, *7*, 14817–14821.
- (50) Hamad, S.; Catlow, C. R. A.; Woodley, S. M.; Lago, S.; Mejias, J. A. Structure and stability of small TiO₂ nanoparticles. *J. Phys. Chem. B* **2005**, *109*, 15741–15748.
- (51) Lv, J.; Wang, Y. C.; Zhu, L.; Ma, Y. M. Particle-swarm structure prediction on clusters. *J. Chem. Phys.* **2012**, *137*, 084104.
- (52) Zhang, Y. X.; Yang, Z. X. Tuning the catalytic activity of Ag-Pd alloy cluster for hydrogen dissociation by controlling the Pd ratio. *Comput. Theor. Chem.* **2015**, *1071*, 39–45.
- (53) Zhao, J. J.; Xie, R. H. Genetic Algorithms for the Geometry Optimization of Atomic and Molecular Clusters. *J. Comput. Theor. Nanosci.* **2004**, *1*, 117–131.
- (54) Lloyd, L. D.; Johnston, R. L.; Roberts, C.; Mortimer-Jones, T. V. Geometry optimization of aluminium clusters using a genetic algorithm. *ChemPhysChem* **2002**, *3*, 408–415.
- (55) Johnston, R. L. Evolving better nanoparticles: Genetic algorithms for optimizing cluster geometries. *Dalton Trans.* **2003**, 4193–4207.
- (56) Plimpton, S. Fast Parallel Algorithms for Short-Range Molecular-Dynamics. *J. Comput. Phys.* **1995**, *117*, 1–19.
- (57) Chuang, F. C.; Liu, B.; Wang, C. Z.; Chan, T. L.; Ho, K. M. Global structural optimization of Si magic clusters on the Si(111) 7 × 7 surface. *Surf. Sci.* **2005**, *598*, L339–L346.
- (58) Albe, K.; Nordlund, K.; Averback, R. S. Modeling the metal-semiconductor interaction: Analytical bond-order potential for platinum-carbon. *Phys. Rev. B: Condens. Matter Mater. Phys.* **2002**, *65*, 195124.
- (59) Tersoff, J. Empirical Interatomic Potential for Carbon, with Applications to Amorphous-Carbon. *Phys. Rev. Lett.* **1988**, *61*, 2879–2882.
- (60) Kresse, G.; Furthmüller, J. Efficiency of ab-initio total energy calculations for metals and semiconductors using a plane-wave basis set. *Comput. Mater. Sci.* **1996**, *6*, 15–50.
- (61) Kresse, G.; Furthmüller, J. Efficient iterative schemes for ab initio total-energy calculations using a plane-wave basis set. *Phys. Rev. B: Condens. Matter Mater. Phys.* **1996**, *54*, 11169–11186.
- (62) Blochl, P. E. Projector Augmented-Wave Method. *Phys. Rev. B: Condens. Matter Mater. Phys.* **1994**, *50*, 17953–17979.
- (63) Kresse, G.; Joubert, D. From ultrasoft pseudopotentials to the projector augmented-wave method. *Phys. Rev. B: Condens. Matter Mater. Phys.* **1999**, *59*, 1758–1775.
- (64) Perdew, J. P.; Burke, K.; Wang, Y. Generalized gradient approximation for the exchange-correlation hole of a many-electron system. *Phys. Rev. B: Condens. Matter Mater. Phys.* **1996**, *54*, 16533–16539.
- (65) Perdew, J. P.; Burke, K.; Ernzerhof, M. Generalized gradient approximation made simple. *Phys. Rev. Lett.* **1996**, *77*, 3865–3868.
- (66) Perdew, J. P.; Yue, W. Accurate and Simple Density Functional for the Electronic Exchange Energy - Generalized Gradient Approximation. *Phys. Rev. B: Condens. Matter Mater. Phys.* **1986**, *33*, 8800–8802.
- (67) Longo, R. C.; Gallego, L. J. Structures of 13-atom clusters of fcc transition metals by ab initio and semiempirical calculations. *Phys. Rev. B: Condens. Matter Mater. Phys.* **2006**, *74*, 193409.
- (68) Chang, C. M.; Chou, M. Y. Alternative low-symmetry structure for 13-atom metal clusters. *Phys. Rev. Lett.* **2004**, *93*, 133401.
- (69) Wang, L. L.; Johnson, D. D. Density functional study of structural trends for late-transition-metal 13-atom clusters. *Phys. Rev. B: Condens. Matter Mater. Phys.* **2007**, *75*, 235405.
- (70) Li, L.; Larsen, A. H.; Romero, N. A.; Morozov, V. A.; Glinvad, C.; Abild-Pedersen, F.; Greeley, J.; Jacobsen, K. W.; Nørskov, J. K. Investigation of Catalytic Finite-Size-Effects of Platinum Metal Clusters. *J. Phys. Chem. Lett.* **2013**, *4*, 222–226.
- (71) Toyoda, E.; Jinnouchi, R.; Hatanaka, T.; Morimoto, Y.; Mitsuhashi, K.; Visikovsky, A.; Kido, Y. The d-Band Structure of Pt Nanoclusters Correlated with the Catalytic Activity for an Oxygen Reduction Reaction. *J. Phys. Chem. C* **2011**, *115*, 21236–21240.
- (72) Liu, X.; Sui, Y. H.; Duan, T.; Meng, C. G.; Han, Y. CO oxidation catalyzed by Pt-embedded graphene: a first-principles investigation. *Phys. Chem. Chem. Phys.* **2014**, *16*, 23584–23593.
- (73) Li, Y. F.; Zhou, Z.; Yu, G. T.; Chen, W.; Chen, Z. F. CO Catalytic Oxidation on Iron-Embedded Graphene: Computational Quest for Low-Cost Nanocatalysts. *J. Phys. Chem. C* **2010**, *114*, 6250–6254.
- (74) Ramos-Sanchez, G.; Balbuena, P. B. Interactions of platinum clusters with a graphite substrate. *Phys. Chem. Chem. Phys.* **2013**, *15*, 11950–11959.
- (75) Nørskov, J. K.; Bligaard, T.; Rossmeisl, J.; Christensen, C. H. Towards the computational design of solid catalysts. *Nat. Chem.* **2009**, *1*, 37–46.
- (76) Kim, G.; Kawazoe, Y.; Lee, K. R. Controlled Catalytic Properties of Platinum Clusters on Strained Graphene. *J. Phys. Chem. Lett.* **2012**, *3*, 1989–1996.
- (77) Bader, R. F. W. A Quantum-Theory of Molecular-Structure and Its Applications. *Chem. Rev.* **1991**, *91*, 893–928.
- (78) Henkelman, G.; Arnaldsson, A.; Jonsson, H. A fast and robust algorithm for Bader decomposition of charge density. *Comput. Mater. Sci.* **2006**, *36*, 354–360.

APPENDIX B
AB INITIO AND CLASSICAL SIMULATIONS OF THE TEMPERATURE
DEPENDENCE OF ZEOLITE PORE SIZES

Ab initio and classical simulations of the temperature dependence of zeolite pore sizes†

Hongbo Shi,^a Angela N. Migués^b and Scott M. Auerbach^{*a,b}

Cite this: *Green Chem.*, 2014, **16**, 875

Ab initio and classical simulations were used to study the equilibrium and fluctuating ring diameters for all-silica zeolites SOD, FER, and MFI over the temperature range 300–900 K. Such simulations are important for understanding and predicting zeolite/guest fit, especially for relatively bulky guest species, e.g., those derived from biomass. We simulated equilibrium zeolite structures, IR spectra, thermal expansion coefficients, and ring breathing vibrations to investigate the competition between negative thermal expansion and enhanced vibrational amplitudes with increasing temperature. We find that although negative thermal expansion tends to shrink equilibrium ring sizes with increasing temperature, this trend is nullified by considering ring breathing vibrations, giving effective pore sizes that are roughly constant with temperature, and larger than those extracted from X-ray data. Several force fields were tested and a modified BKS force field was found to give the best agreement with the simulated properties listed above, especially for MFI. Our results are consistent with previous work suggesting that effective zeolite ring sizes are underestimated by using oxygen ionic radii for estimating atomic excluded volume.

Received 17th August 2013,
Accepted 18th December 2013
DOI: 10.1039/c3gc41681j
www.rsc.org/greenchem

1. Introduction

The regular arrays of pores and channels in zeolites¹ make them indispensable tools for myriad green chemistry applications requiring shape-selective catalysts and adsorbents.² Zeolites may also provide efficient routes for producing fuels and chemicals directly from plant biomass,³ thus being doubly green in terms of both process and feedstock. To achieve this important goal, we need better understanding of the role of zeolite flexibility⁴ in processing biomass-derived species. On the one hand, zeolites are often thought of as highly incompressible solids with large bulk moduli in the range 10–100 GPa. On the other hand, zeolites can often adsorb and/or produce guest molecules with kinetic diameters larger than nominal zeolite pore sizes. For example, catalytic fast pyrolysis (CFP) studies of cellulose in contact with HZSM-5 zeolite at 600 °C carried out by Jae *et al.*⁵ establish the production of naphthalene (~6.2 Å) in the channels of HZSM-5 (5.3 Å × 5.7 Å).⁶ This raises the fundamental question of whether our conceptions of zeolite pore size – determined by X-ray data corrected by estimates of atomic radii – are useful for predicting zeolite/guest fit over a range of conditions (e.g., at the high temperatures of CFP). Accurate pore-size estimates are crucial for designing selective zeolite-based separations

and zeolite-catalyzed reactions – staples of green chemistry – with tight-fitting molecular substrates. To address this issue, we report the application of *ab initio* and classical molecular simulations in the present article to investigate the temperature dependences of pore sizes in small- and medium-pore zeolite types SOD, FER, and MFI.

It is not obvious a priori how heating zeolites influences their effective pore sizes. Indeed, the behaviour of zeolites with increasing temperature likely involves the competition between negative thermal expansion which decreases average pore sizes;⁷ and enhanced thermal vibrations of pores and channels,⁴ which serve to increase effective pore sizes. This competition may be better understood by positing a hierarchy of zeolite structure/energy fluctuations. Towards this end for a given zeolite, we denote the zeolite framework potential energy fluctuation $\Delta V = V(r) - V(r_0)$, where $V(r)$ is the zeolite potential energy at the framework structure given by r , and $V(r_0)$ is the ground state potential energy at the optimal (low pressure) geometry r_0 . [In what follows we ignore the quantity $V_0 = V(r_0)$, which sets the zero of energy but often has little additional physical meaning except in the case of ionic models, for which $|V_0|$ is the vaporization energy of an ionic solid to its corresponding plasma, which itself has little relevance for the present discussion.]

The hierarchy of zeolite structure/energy fluctuations can be understood with the following Taylor-series expansion:

$$\Delta V = \Delta V_1 + \Delta V_2 + \Delta V_3, \quad (1)$$

where ΔV_1 arises from linear displacements, ΔV_2 is the quadratic potential, and ΔV_3 provides cubic corrections. The

^aDepartment of Chemical Engineering, University of Massachusetts, Amherst, MA 01003, USA. E-mail: auerbach@chem.umass.edu

^bDepartment of Chemistry, University of Massachusetts, Amherst, MA 01003, USA

† Electronic supplementary information (ESI) available. See DOI: 10.1039/c3gc41681j

expansion in eqn (1) maps onto the following hierarchy of length scales for a given zeolite pore:

$$d^{\text{eff}}(T) = d_1 + \Delta d_2(T) + \Delta d_3(T), \quad (2)$$

where d_1 is an optimized equilibrium pore size obtained when $\Delta V_1 = 0$, $\Delta d_2(T)$ arises from thermal vibrations at fixed-volume controlled by the quadratic term ΔV_2 ,⁸ and $\Delta d_3(T)$ is from thermal expansion or contraction controlled by the cubic correction Δd_3 .⁹ This hierarchy relies on the fact that harmonic oscillators do not exhibit thermal expansion/contraction; anharmonicities such as cubic terms are required to produce such phenomena.¹⁰

Zeolite pore sizes are usually estimated by measuring d_1 with low- and/or room-temperature X-ray diffraction (XRD), and subtracting a correction for oxygen excluded volume, typically (but not always⁵) using oxygen's crystal ionic radii 1.35 Å.¹¹ However, relatively few systematic studies have been reported⁴ on the temperature dependences of thermal vibrations ($\Delta d_2(T)$) and thermal expansion/contraction ($\Delta d_3(T)$), and how these influence effective pore sizes. Thermal expansion/contraction (*i.e.*, $\Delta d_3(T)$) can be measured by high-temperature XRD,^{7,12} but $\Delta d_3(T)$ is harder to probe experimentally.⁴ Several groups have sought to understand zeolite flexibility at fixed-volume (*i.e.*, $\Delta d_2(T)$) by measuring and modelling infrared (IR) spectra of zeolite frameworks.^{13–15} However, we argue below that IR spectra may focus on vibrations that are not directly relevant to zeolite pore size. Because of the difficulty in fully understanding zeolite pore sizes by experiments alone, we have engaged in *ab initio* and classical simulations (informed by some experimental data) to shed light on these issues.

Because the quantities d_1 and $\Delta d_3(T)$ can be measured by XRD, we lump them together into an effective quantity $d(T) = d_1 + \Delta d_3(T)$. We expect $d(T)$ to be a decreasing function of temperature because of the well-established phenomenon of zeolite thermal contraction.⁷ For the sake of understanding zeolite/guest fit, we estimate the quantity $\Delta d_2(T)$ as the standard deviation of fluctuating ring diameters obtained during our simulations, denoted as $\sigma(T)$. This is motivated by the idea that the *outer turning point* of a ring breathing vibration provides a better estimate of effective pore size than does the equilibrium pore size given by $d(T)$. We expect $\sigma(T)$ to increase with temperature because harmonic vibrational amplitudes scale as the square root of temperature. To test these predictions, we apply simulations to compute $d(T)$ and $\sigma(T)$ to determine how these quantities vary with temperature for all-silica zeolites SOD, FER, and MFI.

Most simulations of zeolite framework flexibility have relied on classical, force field models of the potential energy. Such force fields are often fitted to select experimental data such as low-temperature XRD patterns or IR spectra. However, it is clear from the above discussion that, for the present study, we would require a force field that reproduces all of the following data: low-temperature XRD, high-temperature XRD, and vibrational spectra such as Raman or inelastic-neutron spectra

of zeolites. Few if any force fields have been fitted to such an array of data. In the absence of such a force field, we turn to *ab initio* molecular dynamics (MD) simulations such as the Car-Parrinello MD (CPMD) approach¹⁶ to provide accurate simulation data on zeolite framework fluctuations. *Ab initio* MD has been used to understand many reactions in zeolites,^{17–19} and the corresponding plane-wave density functional theory (DFT) has shed light on many structural and mechanical properties of zeolite solids.^{9,10} Below we show that *ab initio* simulation provides a powerful tool for understanding pore size fluctuations in SOD, FER, and even in the larger MFI structure.

Despite the importance of *ab initio* MD, force fields will likely be the method of choice for simulating zeolites and zeolite framework fluctuations for the foreseeable future. As such, we do seek a force field that can capture as much of the physics behind eqn (1) and (2) as possible. For example, Smirnov *et al.*^{20,21} reported a computational study of ring fluctuations with a force field that reproduces zeolite structure (d_1) and vibrational frequencies (related to $\Delta d_2(T)$), but they did not demonstrate the capability of this force field for modelling thermal expansion/contraction ($\Delta d_3(T)$). On the other hand, the force field used by Yamahara²² reproduces the thermal contraction of MFI, but the predicted vibrational spectrum in the low-frequency region which may be important for pore breathing vibrations was not shown. Below we report a slightly modified version of the force field developed by van Beest, Kramer and van Santen²³ that simultaneously reproduces key aspects of zeolite structure (especially for MFI), ring-breathing amplitudes predicted by CPMD, and negative thermal expansion coefficients measured experimentally.

The findings described below can facilitate the design and optimization of zeolite-based separations and zeolite-catalyzed reactions. For example, sustainable production of *para*-xylene, a key precursor for making plastics and fibers, through cycloaddition of substituted furan and olefins has recently been demonstrated in the large-pore zeolite HY.²⁴ Our findings below may suggest whether running the process in a medium-pore zeolite such as HZSM-5 may enhance the *para*-xylene yield. Other green-chemistry processes such as zeolite-catalyzed fast pyrolysis of biomass to biofuels²⁵ and microwave-heated, catalytic conversion of cellulose to intermediate chemicals in zeolites²⁶ may also be optimized with proper estimates of zeolite pore size.

The remainder of this paper is organized as follows: in section 2 we describe the *ab initio* and classical simulation methods, and also the physical properties calculated; in section 3 we report and discuss the *ab initio* simulation results, and then the classical simulation data including those from the modified force field; and in section 4 we offer concluding remarks.

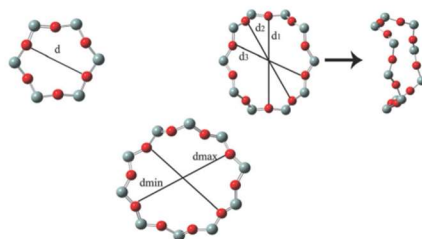
2. Methodology

A. Zeolite systems

X-ray crystallographic data for all-silica zeolites SOD,²⁷ FER,²⁷ and MFI²⁸ provided initial atomic coordinates for

Table 1 Unit cell parameters and repetitions in the simulation boxes

Zeolite type	Unit cell parameters			Simulation box	
	<i>a</i> (Å)	<i>b</i> (Å)	<i>c</i> (Å)	CPMD	Classical
SOD	8.96	8.96	8.96	1 × 1 × 1	2 × 2 × 2
FER	19.01	14.30	7.54	1 × 1 × 1	1 × 1 × 2
MFI	20.02	19.89	13.38	1 × 1 × 1	1 × 1 × 2

**Fig. 1** Rings in SOD (top left), FER (top right), and MFI (bottom).

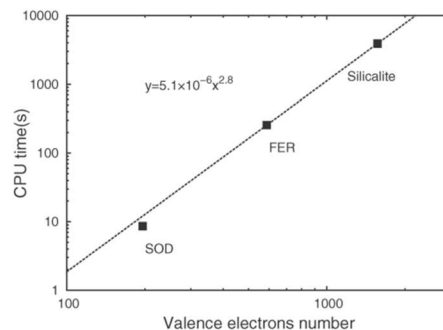
optimizations and molecular dynamics simulations (MD). The orthorhombic MFI structure of van Koningsveld *et al.*,²⁸ stable at temperatures above ~350 K, was studied because of our primary interest in high-temperature framework dynamics. The lattice parameters and system sizes for *ab initio* and classical simulations are listed in Table 1, which shows the larger systems sizes considered by our classical simulations.

Periodic boundary conditions were applied to all simulation cells, effectively surrounding the system with infinite mirror images to approximate macroscopic crystals.

Tight-fitting guest diffusion in zeolites is typically controlled by the largest rings that form connected windows and channels in a given zeolite structure. Thus in this work we considered ring sizes for rings with the largest diameters. The relevant rings of SOD, FER, and MFI are shown in Fig. 1. Ring diameters always refer herein to the distances between opposing oxygen atoms. Ring sizes are labeled by the number of alternating Si–O moieties; *e.g.*, a ring with 6 alternating Si–O linkages is called a “6-ring.” The three possible diameters of the 6-rings of SOD are equal by symmetry (Fig. 1); small thermal fluctuations that deviate from such SOD symmetry are ignored below. The 10-ring window in all-silica FER zeolite deviates strongly from planarity. Due to symmetry, three distinct diameters are observed in a single 10-ring of FER. The 10-ring in MFI is elliptical; we focus on the maximum and minimum diameters.

B. *Ab initio* simulations

Ab initio optimizations and molecular dynamics simulations were performed using the Car-Parrinello MD (CPMD) software package, which has been successfully applied to investigate the structural and electronic properties of zeolites.²⁹ In this

**Fig. 2** CPU time (per processor per dynamic step) scaling with system size expressed as the number of valence electrons.

work, the local density approximation (LDA) has been used for the exchange-correlation potential; we have shown in earlier work that LDA does a surprisingly good job of reproducing zeolite unit cell volumes and mechanical properties, in many cases better than gradient-corrected functionals.⁹ Filippov²⁹ has also shown that in strongly bonded systems such as zeolites, LDA performs well in describing the structures. To solve the uniform homogeneous electron gas problem, we used the Teter–Pade parameterization. Vanderbilt ultrasoft pseudopotentials were used to represent core-valence electronic interactions for both silicon and oxygen atoms. Valence electrons were represented explicitly using plane waves with a 30 Ry cutoff for all the systems studied below. Because of system size constraints, the Brillouin zone was sampled with Γ -point sampling in all cases.⁹

Single-point wave function calculations were used to begin both geometry optimizations and MD simulations. The electron fictitious mass in dynamics was set to 400 au to ensure good adiabatic behavior of electronic dynamics.³⁰ In constant temperature dynamics, both ions and electrons were thermostatted by Nosé–Hoover chains.^{31–33} Target temperatures for electron kinetic energies were obtained by running short (~1 ps) simulations in which only ion temperatures were thermostatted; the resulting average fictitious electron kinetic energies were taken as the targets for subsequent electron temperature control. The time step for moving atoms was set to 4 au and trajectories were written to disk every 33 steps.

Fig. 2 shows that the CPU time required for each CPMD step scales with the number of electrons to the power 2.8 for the three zeolites studied herein. More details on the system sizes and CPU times can be found in the ESI.† *Ab initio* dynamics for SOD and FER were performed for 30 ps. Because of the great expense of CPMD applied to the MFI zeolite structure, dynamics were run only at the 300 K case for 2 ps.

C. Classical modeling

Classical molecular simulations compute interparticle interactions through empirical force fields parameterized by either

experimental properties and/or first principle calculations. Since there is no need to calculate electronic distributions, CPU times are significantly reduced and larger system sizes can be treated. However, classical simulation results depend largely on the force field parameters used. The transferability and accuracy of force fields are limited because most force fields are generated by reproducing a limited set of properties. Despite these limitations, we seek below a single force field that can reasonably reproduce zeolite structures, vibrations, and thermal expansion properties for the SOD, FER, and MFI frameworks.

We mainly compared three different types of force field. The force field developed by Auerbach *et al.*³⁴ contains Buckingham potentials (eqn (3)), Coulombic potentials, and three-body potentials. The three body term accounts for the relative rigidity of SiO₄ tetrahedra. For simplicity this force field will be referred to as "Three Body Force Field" (TBFF). Three body potentials in DL_POLY have a different form (eqn (4)), requiring us to refit the TBFF to this form.

$$V_{\text{Buckingham}}^{\text{short}} = A \exp\left(\frac{-r}{\rho}\right) - \frac{C}{r^6}, \quad (3)$$

$$V_{\text{Harmonic}}^{\text{tbp}} = \frac{k}{2} (\theta - \theta_0)^2 \exp\left(\frac{-r_{ij}^8 - r_{jk}^8}{\rho^8}\right), \quad (4)$$

We also considered the Beest, Kramer, and van Santen force field³⁵ (BKSFF), fitted to *ab initio* data and containing the same potential terms as TBFF except that BKSFF lacks three-body potential terms. BKSFF has been shown to reproduce elastic constants and negative thermal expansion for CHA and SAS zeolites.

We also considered the force field developed by Pedone, Malavasi, Menziani, Cormack, and Segre³⁶ (PMMFF), which includes the Morse potential for the short-range interaction. Like the BKSFF, the PMMFF lacks three body potential terms. PMMFF is able to reproduce structural parameters and mechanical properties of a wide range of crystalline silicates. The force field developed by Yamahara *et al.*²² (YOKFF), and a modified version of the BKSFF (MBKSFF) were also considered. All force field parameters used in this study are given in the ESI.†

For our classical simulations, we used the parallel DL_POLY-2 package which was developed at Daresbury Laboratory.³⁷ We have performed constant volume (NVT) classical molecular dynamics with target temperature of 300 K, 600 K and 900 K. The data collected during these simulations were used to compute equilibrium structure, infrared spectrum and ring distributions. At each temperature, the experimental volume^{12,38,39} was used, thus the effect of thermal contraction was included. The temperature was controlled during the simulation by Nose-hover thermostat^{31–33} with relaxation time of 0.1 ps. To calculate the equilibrium volume and thermal expansion coefficients, constant pressure (NPT) simulations were performed. Pressure and temperature were controlled by Berendsen thermostat with relaxation time of 0.1 ps. The initial configurations for all dynamics at higher temperatures

were obtained by isotropic decrease of that in 300 K. Initial velocities were randomly assigned by Maxwell Boltzmann distribution. We used the leap frog algorithm⁴⁰ to integrate Newton's equation with a time step of 1 fs. For electrostatic interactions, we used Ewald summations with a cutoff smaller than the half of the minimum cell vector length. Trajectories were stored for 100 ps and written to disk every 4 steps.

D. Structure optimization

Structure is a primary property in PES evaluation. We optimized the structures of SOD, FER and MFI by both an *initio* and classical simulations. In *ab initio* simulations the minimum energy configurations were searched using the conjugate gradient method with a max force threshold value of 10^{−3} au. In addition the geometries were also optimized with DL_POLY, implemented by a combination of conjugate gradient and low temperature dynamics, using a threshold value of 10^{−5} au.

The atom positions in the relaxed structure are recorded and the average standard deviations, R^{opt} , from the experimental structures are calculated according to:

$$R^{\text{opt}} = \sqrt{\frac{1}{N} \sum_i^N (r_i^{\text{opt}} - r_i^{\text{exp}})^2}, \quad (5)$$

where r is the atom coordinates and N is the total number of particles in the simulation systems.

E. Equilibrium structure

The experimental structures that we used for comparison were extracted from the X-ray crystallographic data. The measured atomic coordinates correspond to the equilibrium geometry on the PES. Thus a more accurate comparison would be provided if dynamics were used to determine the equilibrium structure through averaging of the atom positions.

In CPMD simulations for SOD, a center of mass shift was observed. In order to compare the SOD structures the resultant movement of the center of mass was deducted. The structural deviation, R^{eq} , at 300 K was calculated according to

$$R^{\text{eq}} = \sqrt{\frac{1}{N} \sum_i^N (\langle r_i^{\text{eq}} \rangle - r_i^{\text{exp}})^2}, \quad (6)$$

where r_i^{eq} is the ensemble average of i th atom's coordinates.

F. Infrared spectrum

Vibrational frequencies are usually measured by infrared (IR) spectroscopy and are dependent on the second derivatives of the PES. The simulation method would be more reliable if the calculated computed IR peaks are in close agreement with experimental results.

Typically the IR spectrum calculation utilizes linear response theory through a Fourier transform of the total dipole moment auto correlation function as follows:^{41,42}

$$I(\omega)_{\text{cl}} = \frac{1}{2\pi} \int_{-\infty}^{+\infty} dt e^{-i\omega t} \{ \langle \vec{M}(t) \cdot \vec{M}(0) \rangle - \langle \vec{M} \rangle^2 \}, \quad (7)$$

where $I(\omega)_{cl}$ is the spectral density or the classical absorption lineshape, and ω is the angular frequency. In classical modeling, the dipole moment at each step is calculated according to:

$$\mathbf{M}(t) = \sum_i^N q_i \mathbf{r}_i(t), \quad (8)$$

where q and \mathbf{r} represent the charge and the coordinates associated with i th atom. The IR spectrum can be obtained using atomic velocities and charges.⁴² This approach avoids discontinuities in atomic positions that arise when employing periodic boundary conditions.⁴³ The intensities obtained by this method are qualitative because the quantum corrections needed to give completely accurate intensities are impractical for such a large system.⁴⁴ Previous MD trajectories were used to calculate IR intensities.

G. Thermal expansion coefficient

Thermal expansion coefficients were calculated for the total volume at 200 K–900 K. In CPMD NPT simulations, the volume exhibited a physically meaningless periodic oscillation. As such the algorithm in CPMD NPT is not applicable to thermal expansion coefficients and classical NPT simulation was used to determine this property.

Linear regression analysis was performed and the slopes were used to calculate thermal expansion coefficients according to:

$$\alpha_V = \frac{1}{V(300\text{ K})} \frac{dV}{dT}, \quad (9)$$

H. Ring distribution

Average ring diameters and standard deviations were calculated at 300 K, 600 K, and 900 K. To obtain better statistics, the ring diameters were averaged over time and the simulation box through:

$$d = \frac{\sum_{k=1}^{N_{\text{ring}}} \sum_{j=1}^{N_{\text{sym}}} \sum_{i=1}^{N_{\text{step}}} d_{ijk}}{N_{\text{ring}} \times N_{\text{sym}} \times N_{\text{step}}}, \quad (10)$$

where N_{step} represents the number of dynamic simulation steps, N_{sym} is the number of symmetric diameters in the same ring. N_{sym} is 3 for SOD and 2 for d_2 in FER (Fig. 1). N_{ring} is the number of similar rings in the simulation box. For example, we used four 10-rings to sample d_{min} and d_{max} .

Standard deviation of each distance σ_{jk} was first calculated over time using eqn (11) and then σ was calculated by average over the simulation box.

$$\sigma_{jk} = \sqrt{\frac{\sum_{i=1}^{N_{\text{step}}} (d_i - \langle d \rangle)^2}{N_{\text{step}}}}, \quad (11)$$

where $\langle \rangle$ is the ensemble average.

3. Results and discussion

Here we report our *ab initio* simulation results for the equilibrium structures, IR spectra, and ring breathing vibrations in SOD, FER and MFI-type zeolites. We will then use the CPMD results, partnered with experimental data, to evaluate the applicability of different force fields for describing such properties.

A. Structures

Table 2 shows the simulated structural deviations, R^{opt} and R^{eq} , determined using both CPMD and classical dynamics. The structures of SOD and FER obtained from *ab initio* simulations agree reasonably well with experimental data with a standard deviation, R^{eq} , of <0.1 Å. In the case of MFI, the R^{eq} is greater than 0.1 Å but still relatively small at 0.18 Å. Longer simulation times may be necessary to decrease the R^{eq} of MFI but at this time are not computationally tractable. In general the small deviations between the *ab initio* simulation and the experimental structure prove that *ab initio* simulation is both a reliable and accurate tool for modeling zeolite structure.

We have also used classical simulation and employed different force fields to determine the deviations in all three zeolites (see Table 2). Although BKSFF and PMMFF are slightly better than TBFF at modeling the structure of SOD and FER, the deviations in MFI by these two Force fields are much greater due to large distortions in the framework. These results confirm that force field simulations are highly dependent on the potential forms and parameters used in their development and as such lack the universal applicability and transferability of *ab initio* simulations. Without further refinement, BKSFF and PMMFF are not good candidates for describing the structural properties of MFI, such as ring distribution. Based on BKSFF, we increased the point charges of Si and O in MFI and obtained a modified BKSFF (MBKSFF, see Table S2†), which reproduces an equilibrium MFI structure closest to experiments among all the force fields used in this study.

B. Infrared spectrum at 300 K

The infrared spectra for SOD and FER at 300 K are shown in ESI (Fig. S1†). Several studies^{21,45,46} have suggested peak assignments in the lower wavenumber region (400–750 cm^{-1}) to ring vibrations. Analysis for isolated rings⁴⁷ of silico-oxygen tetrahedra has shown that a single band located in the region

Table 2 Deviation of optimized structure R^{opt} and equilibrium structure R^{eq} from experiment

Potential	SOD		FER		MFI	
	R^{opt} (Å)	R^{eq} (Å)	R^{opt} (Å)	R^{eq} (Å)	R^{opt} (Å)	R^{eq} (Å)
CPMD	0.08	0.04	0.02	0.05	0.03	0.18
TBFF	0.07	0.08	0.10	0.07	0.13	0.14
BKSFF	0.02	0.07	0.07	0.05	0.57	0.60
PMMFF	0.02	0.06	0.05	0.06	0.57	0.59
YOKFF	0.06	0.12	0.04	0.12	0.43	0.35
MBKSFF	0.07	0.04	0.08	0.08	0.20	0.12

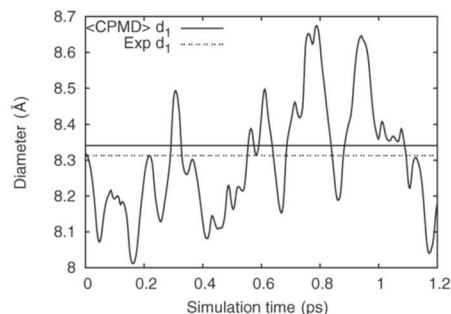


Fig. 3 Ring diameter d_1 evolves with time for FER by CPMD at 300 K. Experimental d_1 is from XRD measurement.²⁷

of the so-called pseudolattice vibrations ($400\text{--}800\text{ cm}^{-1}$) corresponds to the ring vibration. Increasing the size of the ring results in the shift of characteristic band positions toward lower wavenumbers.⁴⁸ This suggests that vibrational frequencies for even larger rings such as 10-rings may fall below the typical infrared wavenumber window for zeolites ($400\text{--}1200\text{ cm}^{-1}$).⁴⁸ Fig. 3 shows the ring diameter oscillation for FER obtained from CPMD simulation. The frequency of the ring diameter vibration can be roughly estimated by counting the number of waves per picosecond and was determined to be around 200 cm^{-1} . Another method to calculate the frequency is to perform a Fourier transform of the ring diameter auto correlation function over a short time-scale (0.2 ps). This method produced a broad frequency distribution ranging from $0\text{--}400\text{ cm}^{-1}$ with a notable peak at 120 cm^{-1} . Therefore the peak in IR spectrum for FER at approximately 400 cm^{-1} should not be assigned to ring vibration. The infrared spectrum is thus not an effective property to evaluate the applicability of force fields for modeling ring vibrations in medium to large pore zeolites. As such we conclude that CPMD is a better suited method for studying the direct ring vibrations in zeolites.

C. Thermal contraction at standard pressure

Negative thermal expansion (NTE) in zeolites has been observed experimentally in many zeolites such as siliceous Sodalite,⁴⁹ LTA,⁵⁰ MFI,¹² ITQ-7 and ITQ-9.⁵¹ In order to reproduce NTE behavior accurately, the force field used should include the anharmonic contributions of the PES, as close to that of the true PES.¹⁰ In NPT dynamic simulations using TBFF, the unit cell tends to quickly shrink followed by subsequent collapse. This suggests that either the TBFF calculation is not stable with respect to this algorithm or that the TBFF constructed PES deviates too much from the true PES at large displacements. Fig. 4 shows the volume change with respect to temperature for 200 K–900 K. The experimental data used for comparing, SOD, FER and MFI were taken from Zheng,³⁸ Bull³⁹ and Bhande¹² respectively. The thermal

expansion coefficients determined by all force fields agree reasonably well with experimental results (Table 3). However, PMMFF and BKSFF tends to overestimate the volume which agrees with the results of previous simulations by Combariza²³ regarding Si-CHA and Si-SAS. Unit cell volume calculated by modified BKSFF is very close to the experiment value for all three zeolites in a wide range of temperature. In Fig. 4, a maximum point for FER was observed in the experimental data at 400 K. We have not been able to simulate this phenomenon with any of the force fields studied, however since our simulations focus on higher temperature regimes it is not necessary to reproduce.

D. Ring distribution at 300, 600 and 900 K

As shown above, CPMD provides a practical way to obtain ring size distributions. Fig. 5 shows fluctuations of d_1 in two different 10-rings in the FER simulation box. A timescale of 30 ps was sufficient to minimize statistical error in the fluctuation calculation. However simulating the fluctuations in MFI on such a time-scale is not computationally tractable due to a significant increase in system size compared to FER. Fig. 5 also suggests that at 2 ps, the fluctuations in FER fall into the region where statistical error is 10%.

Thus we assume that a 2 ps time-scale for simulation of MFI is sufficient to model ring fluctuation within 10% uncertainty. Although there is more error associated with a shorter time-scale, understanding the dynamics in MFI will provide some information for the vibration.

Average ring diameters and fluctuations for SOD and FER are plotted in Fig. 6. Simulations for the two zeolites show similar trends with respect to temperature dependent ring distributions. We conclude the following from Fig. 6:

1. In SOD the contribution of σ to d^{eff} is $\sim 0.4\text{ Å}$, almost 15% of the 'static' ring size (2.6 Å using standard atomic radii). This suggests that ring vibration needs to be considered in catalysis design, especially for tight-fitting guest molecules.
2. The average ring size d decreases when the temperature increases, indicating that the bridging oxygen atoms tend to explore the space inside the pores, which might responsible for the NTE phenomenon.
3. The ring fluctuation amplitude σ is much bigger than the average ring size change from one temperature to the next [$\Delta d = d(T_2) - d(T_1)$]. This suggests that it may be more important to model the ring vibrations than the contraction properties.
4. The effective ring diameter $d + \sigma$ appears roughly independent of temperature.

Fig. 7 and 8 show the FFs calculation for ring size distribution of SOD and FER. All FFs show good agreement with *ab initio* simulations in structure calculation in a wide temperature range; however, the fluctuations of SOD rings predicted by YOKFF is closer with *ab initio* results. For FER, PMMFF shows excellent agreement with *ab initio* simulations results in ring fluctuation calculations.

We find from Fig. S1† that the IR spectra predicted by all the force fields overestimate the frequencies in the lower

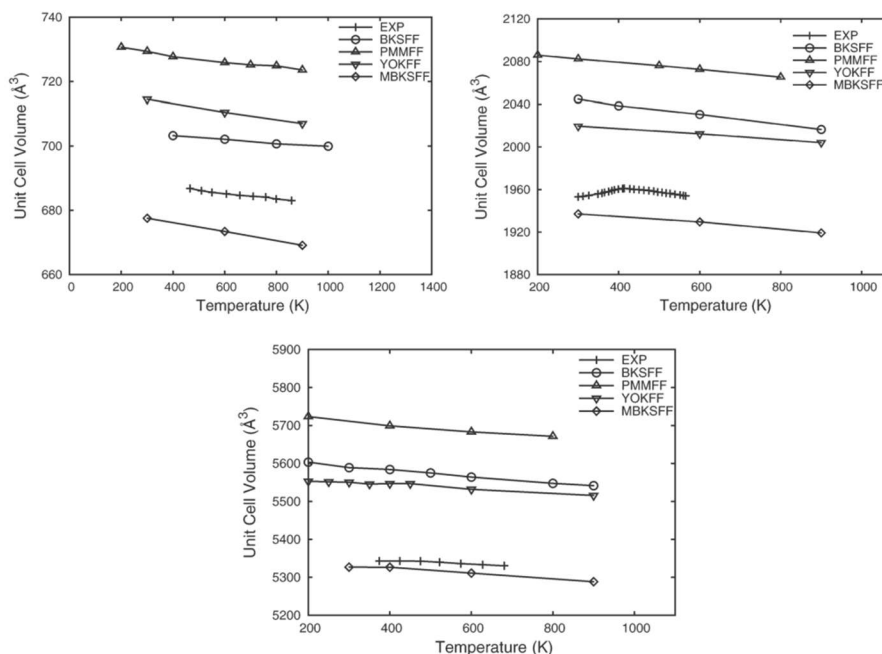


Fig. 4 Unit cell volume calculated by FFs for SOD (top left), FER (top right) and MFI (bottom). Experimental data are from ref. 38, 39 and 12.

Table 3 Thermal expansion coefficient

	$\alpha_v \times 10^6 \text{ (K}^{-1}\text{)}$		
	SOD	FER	MFI
EXP	-13.0 ^a	-24.2 ³⁹	-7.6 ¹²
BKSFF	-8.0	-22.5	-16.6
PMMFF	-13.3	-16.3	-15.6
YOK	-17.5	-12.7	-10.0
MBKSFF	-20.7	-12.5	-12.7

^a Calculated based on volume data³⁸ by eqn (9).

wavenumber region. According to eqn (S4),[†] ring vibration amplitudes should be underestimated using all three force fields if lower frequency region accounts for ring vibrations, which however is not the case. On the other hand, PMMFF shows highest discrepancy in all frequency regions simulation for FER, but closest to *ab initio* simulation results in ring fluctuation calculations. These results again suggest that the peaks at approximately 400 cm⁻¹ should not be assigned to ring vibration and infrared spectrum is not an effective property to evaluate the applicability of force fields for modeling ring vibration.

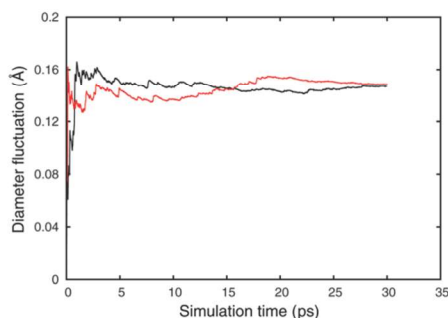


Fig. 5 Ring diameter fluctuations evolve with time for FER by *ab initio* dynamics; two lines represent the diameter of same type (d_1) but in different rings of in simulation box.

Due to the limitation of current computer capability, it is unlikely to get accurate ring distribution for MFI using *ab initio* dynamics. The only information we may extract from previous 2 ps NVT dynamics for MFI is an estimation of 10-rings vibration amplitude (Table 4) with 10% error. Using ionic radius of 1.35 Å¹¹, $d_{\text{max}}^{\text{eff}}$ of MFI becomes 5.92 ± 0.2 Å, still

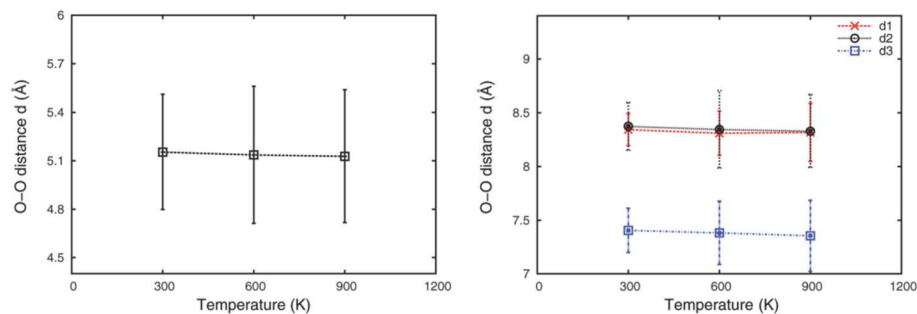


Fig. 6 SOD and FER ring distributions by CPMD at 300 K, 600 K and 900 K; error bar represents standard deviation σ .

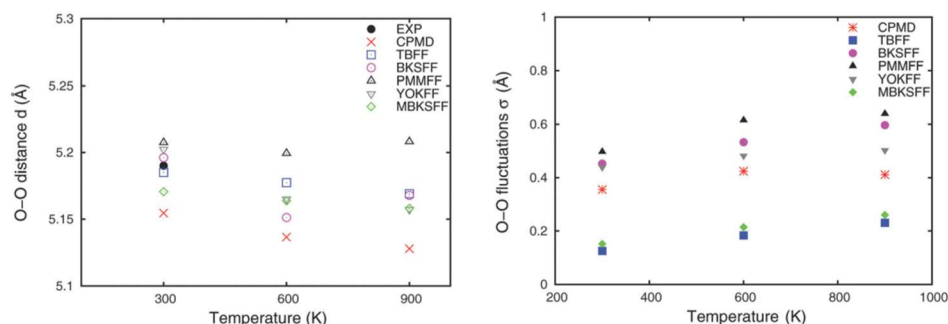


Fig. 7 Comparison of FFs dynamics with CPMD in SOD ring distributions at 300 K, 600 K and 900 K.

smaller than naphthalene kinetic diameter. Thus, in addition to the flexibility of the ring size, a proper choice for the atomic size should be considered to explain the anomalous host-guest fitting phenomenon.⁵²

To evaluate the force fields ability to accurately model zeolite structure we compare ring sizes. Table 4 shows the maximum and minimum equilibrium ring sizes in MFI 10-rings. *Ab initio* dynamics again shows high accuracy in structure calculation. The ring shape determined by BKSFF and PMMFF is much more elliptical than that reported experimentally, which explains the high simulation deviation for structures in Table 2. MBKSFF shows best performance in the static ring modeling.

Ab initio calculation suggests that MFI has a larger ring than SOD and FER but a smaller fluctuation. The framework environment where the ring is located should highly affect the ring motions. The fluctuations of the maximum and minimum rings are also shown. All FFs shows similar capability in modeling the fluctuation amplitude for MFI.

Among the force fields, MBKSFF shows best performance in structure, ring size, ring fluctuation and thermal

contraction calculation for MFI at 300 K, thus a good candidate for classical modeling of MFI.

NVT dynamics with MBKSFF was carried out for 100 ps at 300 K, 600 K, and 900 K; average and fluctuation of d_{\min} and d_{\max} were then calculated and shown in Fig. 9. The opposite change of d_{\min} and d_{\max} indicates a less elliptical ring at higher temperature. d_{\max}^{eff} is almost independent with the temperature, which indicates that molecules which cannot go into MFI channel at 300 K would also be rejected at 900 K.

4. Conclusions

We performed *ab initio* calculation for SOD, FER and MFI using geometry optimization and dynamics techniques. LDA functional shows high accuracy in calculating structure properties and were found better than BLYP functional for in IR computations. Ring distributions study for SOD and FER by *ab initio* dynamics shows that at elevated temperature the ring size d decreases, ring vibration amplitude σ increases and the

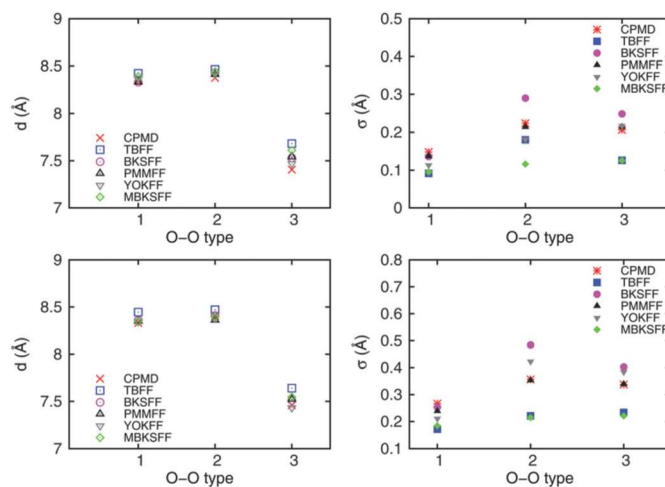


Fig. 8 Comparison of FFs dynamics with CPMD in FER Ring distributions at 300 K (top) and 900 K (bottom).

Table 4 Ring size data for MFI at 300 K

	d_{\min} (Å)	d_{\max} (Å)	σ (Å)
EXP ^a	7.92	8.45	N/A
CPMD	8.03	8.48	0.17
TBFF	8.32	8.39	0.2
BKSFF	7.13	9.53	0.19
PMMFF	7.11	9.56	0.17
YOKFF	7.41	9.26	0.2
MBKSFF	7.99	8.66	0.19

^a From van Koningsveld.²⁸

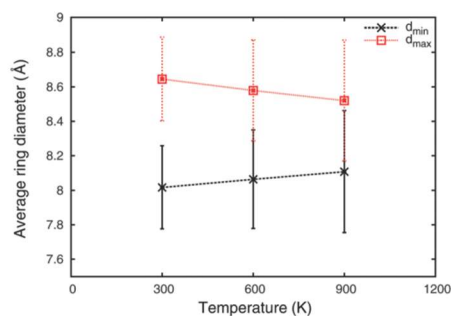


Fig. 9 MFI ring distributions at 300 K, 600 K, and 900 K by MBKSFF; error bar represents standard deviation σ .

effective ring diameters d^{eff} are approximately unchanged. We conclude that ring vibration should be considered in pore size calculation, especially for 6-ring in SOD.

Classical modelling was also performed using several force fields. Structure, vibration frequencies, thermal contraction and ring distributions was studied and the results were used for FFs evaluation. We find IR frequencies not important in ring motion simulations. YOKFF, PMMFF and MBKSFF are more accurate for modelling the structure and flexibility of SOD, FER and MFI respectively.

Classical modelling using the MBKSFF indicates that similar with SOD and FER, the effective value of the maximum ring diameter of the 10-rings in MFI the fluctuations of SOD rings MFI also shows no temperature dependence. In the future we will focus on framework-guest molecules interactions in tight-fitting host guest systems.

Acknowledgements

We thank Dr S. Vaitheeswaran and Jacob Harvey for simulation suggestions. We also thank Dr Andrew Teixeira for helpful discussions. This work was supported by the National Science Foundation (CBET 0932777).

References

- 1 S. M. Auerbach, K. A. Carrado and P. K. Dutta, *Handbook of Zeolite Science and Technology*, Marcel Dekker, New York, 2003.
- 2 A. Corma, *Chem. Rev.*, 1995, **95**, 559–614.
- 3 T. R. Carlson, J. Jae, Y. C. Lin, G. A. Tompsett and G. W. Huber, *J. Catal.*, 2010, **270**, 110–124.

- 4 M. W. Deem, J. M. Newsam and J. A. Creighton, *J. Am. Chem. Soc.*, 1992, **114**, 7198–7207.
- 5 J. Jae, G. A. Tompsett, A. J. Foster, K. D. Hammond, S. M. Auerbach, R. F. Lobo and G. W. Huber, *J. Catal.*, 2011, **279**, 257–268.
- 6 H. van Koningsveld, *Acta Crystallogr., Sect. B: Struct. Sci.*, 1990, **46**, 731–735.
- 7 D. S. Bhange and V. Ramaswamy, *Microporous Mesoporous Mater.*, 2007, **103**, 235–242.
- 8 S. C. Turaga and S. M. Auerbach, *J. Chem. Phys.*, 2003, **118**, 6512–6517.
- 9 R. Astala, S. M. Auerbach and P. A. Monson, *J. Phys. Chem. B*, 2004, **108**, 9208–9215.
- 10 R. Astala, S. M. Auerbach and P. A. Monson, *Phys. Rev. B: Condens. Matter*, 2005, **71**, 014112.
- 11 W. M. Meier, D. H. Olson and C. Baerlocher, *Zeolites*, 1996, **17**, 1–229.
- 12 D. S. Bhange and V. Ramaswamy, *Mater. Res. Bull.*, 2006, **41**, 1392–1402.
- 13 R. Bueno-Perez, S. Calero, D. Dubbeldam, C. O. Ania, J. B. Parra, A. P. Zaderenko and P. J. Merkling, *J. Phys. Chem. C*, 2012, **116**, 25797–25805.
- 14 K. S. Smirnov and D. Bougeard, *Catal. Today*, 2001, **70**, 243–253.
- 15 P. Bornhauser and D. Bougeard, *J. Phys. Chem. B*, 2001, **105**, 36–41.
- 16 R. Car and M. Parrinello, *Phys. Rev. Lett.*, 1985, **55**, 2471–2474.
- 17 C. Lo, C. A. Giurumescu, R. Radhakrishnan and B. L. Trout, *Mol. Phys.*, 2004, **102**, 281–288.
- 18 C. A. Giurumescu and B. L. Trout, *AIChE Symp. Ser.*, 2001, **97**, 313–316.
- 19 K. Schwarz, E. Nusterer and P. Margl, *Int. J. Quantum Chem.*, 1997, **61**, 369–380.
- 20 K. S. Smirnov and D. Bougeard, *J. Phys. Chem.-Us*, 1993, **97**, 9434–9440.
- 21 K. S. Smirnov and D. Bougeard, *J. Mol. Struct.*, 1995, **348**, 155–158.
- 22 K. Yamahara, K. Okazaki and K. Kawamura, *Catal. Today*, 1995, **23**, 397–402.
- 23 A. F. Combariza, G. Sastre and A. Corma, *J. Phys. Chem. C*, 2009, **113**, 11246–11253.
- 24 C. L. Williams, C. C. Chang, P. Do, N. Nikbin, S. Caratzoulas, D. G. Vlachos, R. F. Lobo, W. Fan and P. J. Dauenhauer, *ACS Catal.*, 2012, **2**, 935–939.
- 25 S. Vaitheeswaran, S. K. Green, P. Dauenhauer and S. M. Auerbach, *ACS Catal.*, 2013, **3**(9), 2012–2019.
- 26 J. González-Rivera, I. R. Galindo-Esquivel, M. Onor, E. Bramanti, I. Longo and C. Ferrari, *Green Chem.*, 2013, DOI: 10.1039/C3GC42207K.
- 27 C. Baerlocher and L. B. McCusker, Database of Zeolite Structures, <http://www.iza-structure.org/databases/>
- 28 H. van Koningsveld, H. van Bekkum and J. C. Jansen, *Acta Crystallogr., Sect. B: Struct. Sci.*, 1987, **43**, 127–132.
- 29 F. Filippone, F. Buda, S. Iarlori, G. Moretti and P. Porta, *J. Phys. Chem.-Us*, 1995, **99**, 12883–12891.
- 30 G. Pastore, E. Smargiassi and F. Buda, *Phys. Rev. A*, 1991, **44**, 6334.
- 31 S. Nosé, *Mol. Phys.*, 1984, **52**, 255.
- 32 W. Hoover, *Phys. Rev. A*, 1985, **31**, 1695.
- 33 P. H. Hünenberger, *Adv. Polym. Sci.*, 2005, **173**, 105.
- 34 S. M. Auerbach, N. J. Henson, A. K. Cheetham and H. I. Metiu, *J. Phys. Chem.-Us*, 1995, **99**, 10600–10608.
- 35 B. W. van Beest, G. J. Kramer and R. A. van Santen, *Phys. Rev. Lett.*, 1990, **64**, 1955–1958.
- 36 A. Pedone, G. Malavasi, M. C. Menziani, A. N. Cormack and U. Segre, *J. Phys. Chem. B*, 2006, **110**, 11780–11795.
- 37 I. T. Todorov, W. Smith, K. Trachenko and M. T. Dove, *J. Mater. Chem.*, 2006, **16**, 1911–1918.
- 38 Z. K. Zheng, V. V. Gulians and S. Misture, *J. Porous Mater.*, 2009, **16**, 343–347.
- 39 I. Bull, P. Lightfoot, L. A. Villaescusa, L. M. Bull, R. K. B. Gover, J. S. O. Evans and R. E. Morris, *J. Am. Chem. Soc.*, 2003, **125**, 4342–4349.
- 40 D. Frenkel and B. Smit, *Understanding Molecular Simulation: From Algorithms to Applications*, 2002.
- 41 P. H. Berens and K. R. Wilson, *J. Chem. Phys.*, 1981, **74**, 4872–4882.
- 42 V. Agarwal, G. W. Huber, W. C. Conner and S. M. Auerbach, *J. Chem. Phys.*, 2011, **135**, 134506.
- 43 P. Bornhauser and D. Bougeard, *J. Raman Spectrosc.*, 2001, **32**, 279–285.
- 44 J. B. Nicholas, A. J. Hopfinger, F. R. Trouw and L. E. Iton, *J. Am. Chem. Soc.*, 1991, **113**, 4792–4800.
- 45 A. J. M. de Man and R. A. van Santen, *Zeolites*, 1992, **12**, 269–279.
- 46 W. Mozgawa, *J. Mol. Struct.*, 2001, **596**, 129–137.
- 47 M. Sitarz, W. Mozgawa and M. Handke, *J. Mol. Struct.*, 1997, **404**, 193–197.
- 48 M. Sitarz, M. Handke and W. Mozgawa, *Spectrochim. Acta, Part A*, 1999, **55**, 2831–2837.
- 49 L. Leardini, A. Martucci and G. Cruciani, *Microporous Mesoporous Mater.*, 2012, **151**, 163–171.
- 50 T. Carey, A. Corma, F. Rey, C. C. Tang, J. A. Hriljac and P. A. Anderson, *Chem. Commun.*, 2012, **48**, 5829–5831.
- 51 P. Lightfoot, D. A. Woodcock, M. J. Maple, L. A. Villaescusa and P. A. Wright, *J. Mater. Chem.*, 2001, **11**, 212–216.
- 52 M. Cook and W. C. Conner, in Proceedings of the International Zeolite Conference, 12th, Baltimore, 1998, p. 409.

BIBLIOGRAPHY

- (1). Carrette, L.; Friedrich, K. A.; Stimming, U., Fuel cells: Principles, types, fuels, and applications. *Chemphyschem.* **2000**, *1*, 162-193.
- (2). DOE Fuel Cell Technologies Program Record:
https://www.hydrogen.energy.gov/pdfs/16020_fuel_cell_system_cost_2016.pdf
 (Accessed on 17th January 2017).
- (3). Cheng, X.; Shi, Z.; Glass, N.; Zhang, L.; Zhang, J. J.; Song, D. T.; Liu, Z. S.; Wang, H. J.; Shen, J., A review of PEM hydrogen fuel cell contamination: Impacts, mechanisms, and mitigation. *Journal of Power Sources.* **2007**, *165*, 739-756.
- (4). Liu, H. S.; Song, C. J.; Zhang, L.; Zhang, J. J.; Wang, H. J.; Wilkinson, D. P., A review of anode catalysis in the direct methanol fuel cell. *Journal of Power Sources.* **2006**, *155*, 95-110.
- (5). Mehta, V.; Cooper, J. S., Review and analysis of PEM fuel cell design and manufacturing. *Journal of Power Sources.* **2003**, *114*, 32-53.
- (6). Holton, O. T.; Stevenson, J. W., The Role of Platinum in Proton Exchange Membrane Fuel Cells Evaluation of platinum's unique properties for use in both the anode and cathode of a proton exchange membrane fuel cell. *Platinum Metals Review.* **2013**, *57*, 259-271.
- (7). Jung, N.; Cho, Y. H.; Ahn, M.; Lim, J. W.; Kang, Y. S.; Chung, D. Y.; Kim, J.; Cho, Y. H.; Sung, Y. E., Methanol-tolerant cathode electrode structure composed of heterogeneous composites to overcome methanol crossover effects for direct methanol fuel cell. *International Journal of Hydrogen Energy.* **2011**, *36*, 15731-15738.
- (8). Sung, Y. E.; Chrzanowski, W.; Zolfaghari, A.; Jerkiewicz, G.; Wieckowski, A., Structure of chemisorbed sulfur on a Pt(111) electrode. *Journal of the American Chemical Society.* **1997**, *119*, 194-200.
- (9). DOE: <https://energy.gov/eere/fuelcells/hydrogen-resources> (Accessed on 17th January 2017).
- (10). Lemons, R. A., Fuel-Cells for Transportation. *Journal of Power Sources.* **1990**, *29*, 251-264.
- (11). Paffett, M. T.; Pafford, J.; Gottesfeld, S., Effects of Low-Levels of CO on the Performance of PEM Fuel-Cells. *Journal of the Electrochemical Society.* **1988**, *135*, C345-C345.
- (12). Ferrin, P.; Nilekar, A. U.; Greeley, J.; Mavrikakis, M.; Rossmeisl, J., Reactivity descriptors for direct methanol fuel cell anode catalysts. *Surface Science.* **2008**, *602*, 3424-3431.
- (13). Duriez, C.; Henry, C. R.; Chapon, C., Molecular-Beam Study of the Chemisorption of CO on Well Shaped Palladium Particles Epitaxially Oriented on MgO(100). *Surface Science.* **1991**, *253*, 190-204.

- (14). Li, L.; Larsen, A. H.; Romero, N. A.; Morozov, V. A.; Glinsvad, C.; Abild-Pedersen, F.; Greeley, J.; Jacobsen, K. W.; Norskov, J. K., Investigation of Catalytic Finite-Size-Effects of Platinum Metal Clusters. *Journal of Physical Chemistry Letters*. **2013**, *4*, 222-226.
- (15). Yudanov, I. V.; Neyman, K. M.; Rosch, N., Density functional study of Pd nanoparticles with subsurface impurities of light element atoms. *Physical Chemistry Chemical Physics*. **2004**, *6*, 116-123.
- (16). Abad, A.; Concepcion, P.; Corma, A.; Garcia, H., A collaborative effect between gold and a support induces the selective oxidation of alcohols. *Angewandte Chemie-International Edition*. **2005**, *44*, 4066-4069.
- (17). Falsig, H.; Hvolbaek, B.; Kristensen, I. S.; Jiang, T.; Bligaard, T.; Christensen, C. H.; Norskov, J. K., Trends in the catalytic CO oxidation activity of nanoparticles. *Angewandte Chemie-International Edition*. **2008**, *47*, 4835-4839.
- (18). Meyer, R.; Lemire, C.; Shaikhutdinov, S. K.; Freund, H., Surface chemistry of catalysis by gold. *Gold Bulletin*. **2004**, *37*, 72.
- (19). Shinozaki, K.; Morimoto, Y.; Pivovar, B. S.; Kocha, S. S., Re-examination of the Pt Particle Size Effect on the Oxygen Reduction Reaction for Ultrathin Uniform Pt/C Catalyst Layers without Influence from Nafion. *Electrochimica Acta*. **2016**, *213*, 783-790.
- (20). Shi, X. X.; Feng, Y. J.; Liu, J.; Yang, Q.; Ren, N. Q., The effect of carbon particle-size on N-doped carbon catalyst for oxygen reduction reaction in microbial fuel cells. *Sustainable Environment and Transportation*. **2012**, *178-181*, 495-498.
- (21). Viswanathan, V.; Wang, F. Y. F., Theoretical analysis of the effect of particle size and support on the kinetics of oxygen reduction reaction on platinum nanoparticles. *Nanoscale*. **2012**, *4*, 5110-5117.
- (22). Nesselberger, M.; Ashton, S.; Meier, J. C.; Katsounaros, I.; Mayrhofer, K. J. J.; Arenz, M., The Particle Size Effect on the Oxygen Reduction Reaction Activity of Pt Catalysts: Influence of Electrolyte and Relation to Single Crystal Models. *Journal of the American Chemical Society*. **2011**, *133*, 17428-17433.
- (23). Shao, M. H.; Peles, A.; Shoemaker, K., Electrocatalysis on Platinum Nanoparticles: Particle Size Effect on Oxygen Reduction Reaction Activity. *Nano Letters*. **2011**, *11*, 3714-3719.
- (24). Tritsarlis, G. A.; Greeley, J.; Rossmeisl, J.; Norskov, J. K., Atomic-Scale Modeling of Particle Size Effects for the Oxygen Reduction Reaction on Pt. *Catalysis Letters*. **2011**, *141*, 909-913.
- (25). Viswanathan, V.; Wang, F. Y. F.; Pitsch, H., Effect of particle size and support on the catalytic activity of Platinum nanoparticles for oxygen reduction reaction. *Abstracts of Papers of the American Chemical Society*. **2010**, 239.

- (26). Ashton, S. J.; Novo, A.; Mayrhofer, K. J. J.; Arenz, M., Influence of the electrolyte on the particle size effect of the oxygen reduction reaction on Pt nanoparticles. *Proton Exchange Membrane Fuel Cells* **9**, **2009**, 25, 455-462.
- (27). Ye, H.; Crooks, J. A.; Crooks, R. M., Effect of particle size on the kinetics of the electrocatalytic oxygen reduction reaction catalyzed by Pt dendrimer-encapsulated nanoparticles. *Langmuir*. **2007**, 23, 11901-11906.
- (28). Savadogo, O.; Essalik, A., Effect of platinum particle size on the oxygen reduction reaction on 2% Pt-1% H₂WO₄ in phosphoric acid. *Journal of the Electrochemical Society*. **1996**, 143, 1814-1821.
- (29). Imaoka, T.; Kitazawa, H.; Chun, W. J.; Omura, S.; Albrecht, K.; Yamamoto, K., Magic Number Pt-13 and Misshapen Pt-12 Clusters: Which One is the Better Catalyst? *Journal of the American Chemical Society*. **2013**, 135, 13089-13095.
- (30). Crampton, A. S.; Rotzer, M. D.; Ridge, C. J.; Schweinberger, F. F.; Heiz, U.; Yoon, B.; Landman, U., Structure sensitivity in the nonscalable regime explored via catalysed ethylene hydrogenation on supported platinum nanoclusters. *Nature Communications*. **2016**, 7, 10389.
- (31). Valden, M.; Lai, X.; Goodman, D. W., Onset of catalytic activity of gold clusters on titania with the appearance of nonmetallic properties. *Science*. **1998**, 281, 1647-1650.
- (32). Landman, U.; Yoon, B.; Zhang, C.; Heiz, U.; Arenz, M., Factors in gold nanocatalysis: oxidation of CO in the non-scalable size regime. *Topics in Catalysis*. **2007**, 44, 145-158.
- (33). Yu, X. W.; Ye, S. Y., Recent advances in activity and durability enhancement of Pt/C catalytic cathode in PEMFC - Part I. Physico-chemical and electronic interaction between Pt and carbon support, and activity enhancement of Pt/C catalyst. *Journal of Power Sources*. **2007**, 172, 133-144.
- (34). Zhang, J.; Yang, H. Z.; Fang, J. Y.; Zou, S. Z., Synthesis and Oxygen Reduction Activity of Shape-Controlled Pt₃Ni Nanopolyhedra. *Nano Letters*. **2010**, 10, 638-644.
- (35). Takasu, Y.; Kawaguchi, T.; Sugimoto, W.; Murakami, Y., Effects of the surface area of carbon support on the characteristics of highly-dispersed Pt-Ru particles as catalysts for methanol oxidation. *Electrochimica Acta*. **2003**, 48, 3861-3868.
- (36). Bessel, C. A.; Laubernds, K.; Rodriguez, N. M.; Baker, R. T. K., Graphite nanofibers as an electrode for fuel cell applications. *Journal of Physical Chemistry B*. **2001**, 105, 1115-1118.
- (37). Park, K. W.; Sung, Y. E.; Han, S.; Yun, Y.; Hyeon, T., Origin of the enhanced catalytic activity of carbon nanocoil-supported PtRu alloy electrocatalysts. *Journal of Physical Chemistry B*. **2004**, 108, 939-944.

- (38). Steigerwalt, E. S.; Deluga, G. A.; Lukehart, C. M., Pt-Ru/carbon fiber nanocomposites: Synthesis, characterization, and performance as anode catalysts of direct methanol fuel cells. A search for exceptional performance. *Journal of Physical Chemistry B*. **2002**, *106*, 760-766.
- (39). Zhang, W. H.; Shi, J. L.; Wang, L. Z.; Yan, D. S., Preparation and characterization of ZnO clusters inside mesoporous silica. *Chemistry of Materials*. **2000**, *12*, 1408-1413.
- (40). Stevens, D. A.; Dahn, J. R., Thermal degradation of the support in carbon-supported platinum electrocatalysts for PEM fuel cells. *Carbon*. **2005**, *43*, 179-188.
- (41). Stevens, D. A.; Hicks, M. T.; Haugen, G. M.; Dahn, J. R., Ex situ and in situ stability studies of PEMFC catalysts. *Journal of the Electrochemical Society*. **2005**, *152*, A2309-A2315.
- (42). Huang, H. J.; Chen, H. Q.; Sun, D. P.; Wang, X., Graphene nanoplate-Pt composite as a high performance electrocatalyst for direct methanol fuel cells. *Journal of Power Sources*. **2012**, *204*, 46-52.
- (43). Yoo, E.; Okata, T.; Akita, T.; Kohyama, M.; Nakamura, J.; Honma, I., Enhanced Electrocatalytic Activity of Pt Subnanoclusters on Graphene Nanosheet Surface. *Nano Letters*. **2009**, *9*, 2255-2259.
- (44). Li, Y. J.; Gao, W.; Ci, L. J.; Wang, C. M.; Ajayan, P. M., Catalytic performance of Pt nanoparticles on reduced graphene oxide for methanol electro-oxidation. *Carbon*. **2010**, *48*, 1124-1130.
- (45). Kou, R.; Shao, Y. Y.; Wang, D. H.; Engelhard, M. H.; Kwak, J. H.; Wang, J.; Viswanathan, V. V.; Wang, C. M.; Lin, Y. H.; Wang, Y.; Aksay, I. A.; Liu, J., Enhanced activity and stability of Pt catalysts on functionalized graphene sheets for electrocatalytic oxygen reduction. *Electrochemistry Communications*. **2009**, *11*, 954-957.
- (46). Seger, B.; Kamat, P. V., Electrocatalytically Active Graphene-Platinum Nanocomposites. Role of 2-D Carbon Support in PEM Fuel Cells. *Journal of Physical Chemistry C*. **2009**, *113*, 7990-7995.
- (47). Tang, Y. N.; Yang, Z. X.; Dai, X. Q., Trapping of metal atoms in the defects on graphene. *Journal of Chemical Physics*. **2011**, *135*, 224704.
- (48). Rodriguez-Manzo, J. A.; Cretu, O.; Banhart, F., Trapping of Metal Atoms in Vacancies of Carbon Nanotubes and Graphene. *Acs Nano*. **2010**, *4*, 3422-3428.
- (49). Gan, Y. J.; Sun, L. T.; Banhart, F., One- and two-dimensional diffusion of metal atoms in graphene. *Small*. **2008**, *4*, 587-591.
- (50). Wu, G. H.; Huang, H.; Chen, X. M.; Cai, Z. X.; Jiang, Y. Q.; Chen, X., Facile synthesis of clean Pt nanoparticles supported on reduced graphene oxide composites: Their growth mechanism and tuning of their methanol electro-catalytic oxidation property. *Electrochimica Acta*. **2013**, *111*, 779-783.

- (51). He, D. P.; Cheng, K.; Li, H. G.; Peng, T.; Xu, F.; Mu, S. C.; Pan, M., Highly Active Platinum Nanoparticles on Graphene Nanosheets with a Significant Improvement in Stability and CO Tolerance. *Langmuir*. **2012**, *28*, 3979-3986.
- (52). Tang, Y. A.; Yang, Z. X.; Dai, X. Q., A theoretical simulation on the catalytic oxidation of CO on Pt/graphene. *Physical Chemistry Chemical Physics*. **2012**, *14*, 16566-16572.
- (53). Durbin, D. J. D.; Malardier-Jugroot, C., Density Functional Theory Analysis of Metal/Graphene Systems As a Filter Membrane to Prevent CO Poisoning in Hydrogen Fuel Cells. *Journal of Physical Chemistry C*. **2011**, *115*, 808-815.
- (54). Zhou, M.; Zhang, A. H.; Dai, Z. X.; Zhang, C.; Feng, Y. P., Greatly enhanced adsorption and catalytic activity of Au and Pt clusters on defective graphene. *Journal of Chemical Physics*. **2010**, *132*, 194704.
- (55). Kim, G.; Jhi, S. H., Carbon Monoxide-Tolerant Platinum Nanoparticle Catalysts on Defect-Engineered Graphene. *Acs Nano*. **2011**, *5*, 805-810.
- (56). Lim, D. H.; Wilcox, J., Mechanisms of the Oxygen Reduction Reaction on Defective Graphene-Supported Pt Nanoparticles from First-Principles. *Journal of Physical Chemistry C*. **2012**, *116*, 3653-3660.
- (57). Lim, D. H.; Wilcox, J., DFT-Based Study on Oxygen Adsorption on Defective Graphene-Supported Pt Nanoparticles. *Journal of Physical Chemistry C*. **2011**, *115*, 22742-22747.
- (58). Fampiou, I.; Ramasubramaniam, A., Influence of Support Effects on CO Oxidation Kinetics on CO-Saturated Graphene-Supported Pt-13 Nanoclusters. *Journal of Physical Chemistry C*. **2015**, *119*, 8703-8710.
- (59). Fampiou, I.; Ramasubramaniam, A., CO Adsorption on Defective Graphene-Supported Pt-13 Nanoclusters. *Journal of Physical Chemistry C*. **2013**, *117*, 19927-19933.
- (60). Fampiou, I.; Ramasubramaniam, A., Binding of Pt Nanoclusters to Point Defects in Graphene: Adsorption, Morphology, and Electronic Structure. *Journal of Physical Chemistry C*. **2012**, *116*, 6543-6555.
- (61). Okamoto, Y., Density-functional calculations of icosahedral M-13 (M = Pt and Au) clusters on graphene sheets and flakes. *Chemical Physics Letters*. **2006**, *420*, 382-386.
- (62). Jalan, V.; Taylor, E. J., Importance of Interatomic Spacing in Catalytic Reduction of Oxygen in Phosphoric-Acid. *Journal of the Electrochemical Society*. **1983**, *130*, C125-C125.
- (63). Jia, Q. Y.; Liang, W. T.; Bates, M. K.; Mani, P.; Lee, W.; Mukerjee, S., Activity Descriptor Identification for Oxygen Reduction on Platinum-Based Bimetallic Nanoparticles: In Situ Observation of the Linear Composition-Strain-Activity Relationship. *Acs Nano*. **2015**, *9*, 387-400.

- (64). Stephens, I. E. L.; Bondarenko, A. S.; Gronbjerg, U.; Rossmeisl, J.; Chorkendorff, I., Understanding the electrocatalysis of oxygen reduction on platinum and its alloys. *Energy & Environmental Science*. **2012**, *5*, 6744-6762.
- (65). Wang, C.; Chi, M. F.; Li, D. G.; Strmcnik, D.; van der Vliet, D.; Wang, G. F.; Komanicky, V.; Chang, K. C.; Paulikas, A. P.; Tripkovic, D.; Pearson, J.; More, K. L.; Markovic, N. M.; Stamenkovic, V. R., Design and Synthesis of Bimetallic Electrocatalyst with Multilayered Pt-Skin Surfaces. *Journal of the American Chemical Society*. **2011**, *133*, 14396-14403.
- (66). Toda, T.; Igarashi, H.; Uchida, H.; Watanabe, M., Enhancement of the electroreduction of oxygen on Pt alloys with Fe, Ni, and Co. *Journal of the Electrochemical Society*. **1999**, *146*, 3750-3756.
- (67). Stamenkovic, V. R.; Mun, B. S.; Arenz, M.; Mayrhofer, K. J. J.; Lucas, C. A.; Wang, G. F.; Ross, P. N.; Markovic, N. M., Trends in electrocatalysis on extended and nanoscale Pt-bimetallic alloy surfaces. *Nature Materials*. **2007**, *6*, 241-247.
- (68). Xu, C. X.; Wang, L.; Mu, X. L.; Ding, Y., Nanoporous PtRu Alloys for Electrocatalysis. *Langmuir*. **2010**, *26*, 7437-7443.
- (69). Qi, Z. G.; He, C. Z.; Kaufman, A., Effect of CO in the anode fuel on the performance of PEM fuel cell cathode. *Journal of Power Sources*. **2002**, *111*, 239-247.
- (70). Travitsky, N.; Ripenbein, T.; Golodnitsky, D.; Rosenberg, Y.; Burshtein, L.; Peled, E., Pt-, PtNi- and PtCo-supported catalysts for oxygen reduction in PEM fuel cells. *Journal of Power Sources*. **2006**, *161*, 782-789.
- (71). Yu, Y. C.; Xin, H. L. L.; Hovden, R.; Wang, D. L.; Rus, E. D.; Mundy, J. A.; Muller, D. A.; Abruna, H. D., Three-Dimensional Tracking and Visualization of Hundreds of Pt-Co Fuel Cell Nanocatalysts During Electrochemical Aging. *Nano Letters*. **2012**, *12*, 4417-4423.
- (72). Ball, S.; Hodgkinson, A.; Hoogers, G.; Maniguet, S.; Thompsett, D.; Wong, B., The proton exchange membrane fuel cell performance of a carbon supported PtMo catalyst operating on reformat. *Electrochemical and Solid State Letters*. **2002**, *5*, A31-A34.
- (73). Mukerjee, S.; Lee, S. J.; Ticianelli, E. A.; McBreen, J.; Grgur, B. N.; Markovic, N. M.; Ross, P. N.; Giallombardo, J. R.; De Castro, E. S., Investigation of enhanced CO tolerance in proton exchange membrane fuel cells by carbon supported PtMo alloy catalyst. *Electrochemical and Solid State Letters*. **1999**, *2*, 12-15.
- (74). Do, C. L.; Pham, T. S.; Nguyen, N. P.; Tran, V. Q.; Pham, H. H., Synthesis and characterization of alloy catalyst nanoparticles PtNi/C for oxygen reduction reaction in proton exchange membrane fuel cell. *Advances in Natural Sciences-Nanoscience and Nanotechnology*. **2015**, *6*, 025009.

- (75). Baldizzone, C.; Mezzavilla, S.; Carvalho, H. W. P.; Meier, J. C.; Schuppert, A. K.; Heggen, M.; Galeano, C.; Grunwaldt, J. D.; Schuth, F.; Mayrhofer, K. J. J., Confined-Space Alloying of Nanoparticles for the Synthesis of Efficient PtNi Fuel-Cell Catalysts. *Angewandte Chemie-International Edition*. **2014**, *53*, 14250-14254.
- (76). Hyun, K.; Lee, J. H.; Yoon, C. W.; Cho, Y. H.; Kim, L. H.; Kwon, Y., Improvement in oxygen reduction activity of polypyrrole-coated PtNi alloy catalyst prepared for proton exchange membrane fuel cells. *Synthetic Metals*. **2014**, *190*, 48-55.
- (77). da Silva, F. T.; Dalmazzo, V. A.; Becker, M. R.; de Souza, M. O.; de Souza, R. F.; Martini, E. M. A., Effect of Ni proportion on the performance of proton exchange membrane fuel cells using PtNi/C electrocatalysts. *Ionics*. **2014**, *20*, 381-388.
- (78). Wu, Z. Y.; Zhang, W. W.; Sun, S. R., Mechanisms for oxygen reduction reactions on Pt-rich and Pt-poor PtFe alloys as the fuel cell cathode. *Computational Materials Science*. **2016**, *125*, 278-283.
- (79). Guerrini, E.; Grattieri, M.; Faggianelli, A.; Cristiani, P.; Trasatti, S., PTFE effect on the electrocatalysis of the oxygen reduction reaction in membraneless microbial fuel cells. *Bioelectrochemistry*. **2015**, *106*, 240-247.
- (80). Yang, D. S.; Kim, M. S.; Song, M. Y.; Yu, J. S., Highly efficient supported PtFe cathode electrocatalysts prepared by homogeneous deposition for proton exchange membrane fuel cell. *International Journal of Hydrogen Energy*. **2012**, *37*, 13681-13688.
- (81). Zhang, Z. Y.; Li, M. J.; Wu, Z. L.; Li, W. Z., Ultra-thin PtFe-nanowires as durable electrocatalysts for fuel cells. *Nanotechnology*. **2011**, *22*, 015602
- (82). Scott, K.; Yuan, W.; Cheng, H., Feasibility of using PtFe alloys as cathodes in direct methanol fuel cells. *Journal of Applied Electrochemistry*. **2007**, *37*, 21-26.
- (83). Chan, D. S.; Wan, C. C., Influence of Ptfе Dispersion in the Catalyst Layer of Porous Gas-Diffusion Electrodes for Phosphoric-Acid Fuel-Cells. *Journal of Power Sources*. **1994**, *50*, 163-176.
- (84). Esfandiari, A.; Kazemeini, M.; Bastani, D., Synthesis, characterization and performance determination of an Ag@Pt/C electrocatalyst for the ORR in a PEM fuel cell. *International Journal of Hydrogen Energy*. **2016**, *41*, 20720-20730.
- (85). Rashid, M.; Jun, T. S.; Jung, Y.; Kim, Y. S., Bimetallic core-shell Ag@Pt nanoparticle-decorated MWNT electrodes for amperometric H₂ sensors and direct methanol fuel cells. *Sensors and Actuators B-Chemical*. **2015**, *208*, 7-13.
- (86). Khan, I. A.; Qian, Y. H.; Badshah, A.; Zhao, D.; Nadeem, M. A., Fabrication of Highly Stable and Efficient PtCu Alloy Nanoparticles on Highly Porous Carbon for Direct Methanol Fuel Cells. *Acs Applied Materials & Interfaces*. **2016**, *8*, 20793-20801.

- (87). Kloke, A.; Kohler, C.; Zengerle, R.; Kerzenmacher, S., Porous Platinum Electrodes Fabricated by Cyclic Electrodeposition of PtCu Alloy: Application to Implantable Glucose Fuel Cells. *Journal of Physical Chemistry C*. **2012**, *116*, 19689-19698.
- (88). Marcu, A.; Toth, G.; Srivastava, R.; Strasser, P., Preparation, characterization and degradation mechanisms of PtCu alloy nanoparticles for automotive fuel cells. *Journal of Power Sources*. **2012**, *208*, 288-295.
- (89). Wang, A. L.; Zhang, C.; Zhou, W.; Tong, Y. X.; Li, G. R., PtCu alloy nanotube arrays supported on carbon fiber cloth as flexible anodes for direct methanol fuel cell. *AIChE Journal*. **2016**, *62*, 975-983.
- (90). Ye, S. H.; He, X. J.; Ding, L. X.; Pan, Z. W.; Tong, Y. X.; Wu, M. M.; Li, G. R., Cu₂O template synthesis of high-performance PtCu alloy yolk-shell cube catalysts for direct methanol fuel cells. *Chemical Communications*. **2014**, *50*, 12337-12340.
- (91). Zhou, Y. M.; Zhang, D. M., Nano PtCu binary and PtCuAg ternary alloy catalysts for oxygen reduction reaction in proton exchange membrane fuel cells. *Journal of Power Sources*. **2015**, *278*, 396-403.
- (92). Choi, J. H.; Jeong, K. J.; Dong, Y.; Han, J.; Lim, T. H.; Lee, J. S.; Sung, Y. E., Electro-oxidation of methanol and formic acid on PtRu and PtAu for direct liquid fuel cells. *Journal of Power Sources*. **2006**, *163*, 71-75.
- (93). Choi, J. H.; Park, K. W.; Park, I. S.; Kim, K.; Lee, J. S.; Sung, Y. E., A PtAu nanoparticle electrocatalyst for methanol electrooxidation in direct methanol fuel cells. *Journal of the Electrochemical Society*. **2006**, *153*, A1812-A1817.
- (94). da Silva, S. G.; Silva, J. C. M.; Buzzo, G. S.; De Souza, R. F. B.; Spinace, E. V.; Neto, A. O.; Assumpcao, M. H. M. T., Electrochemical and fuel cell evaluation of PtAu/C electrocatalysts for ethanol electro-oxidation in alkaline media. *International Journal of Hydrogen Energy*. **2014**, *39*, 10121-10127.
- (95). da Silva, S. G.; Silva, J. C. M.; Buzzo, G. S.; Neto, A. O.; Assumpcao, M. H. M. T., Use of PtAu/C electrocatalysts toward formate oxidation: electrochemical and fuel cell considerations. *Materials for Renewable and Sustainable Energy*. **2016**, *5*.
- (96). Giorgi, L.; Salernitano, E.; Makris, T. D.; Gagliardi, S.; Contini, V.; De Francesco, M., Innovative electrodes for direct methanol fuel cells based on carbon nanofibers and bimetallic PtAu nanocatalysts. *International Journal of Hydrogen Energy*. **2014**, *39*, 21601-21612.
- (97). Hu, X. L.; Lin, C. L.; Wei, L.; Hong, C. H.; Zhang, Y. F.; Zhuang, N. F., High electrocatalytic performance of graphene nanoribbon supported PtAu nanoalloy for direct ethanol fuel cell and theoretical analysis of anti-CO poisoning. *Electrochimica Acta*. **2016**, *187*, 560-566.

- (98). Silva, J. C. M.; da Silva, S. G.; De Souza, R. F. B.; Buzzo, G. S.; Spinace, E. V.; Neto, A. O.; Assumpcao, M. H. M. T., PtAu/C electrocatalysts as anodes for direct ammonia fuel cell. *Applied Catalysis a-General*. **2015**, *490*, 133-138.
- (99). Zhang, S. S.; Yuan, X. Z.; Hin, J. N. C.; Wang, H. J.; Friedrich, K. A.; Schulze, M., A review of platinum-based catalyst layer degradation in proton exchange membrane fuel cells. *Journal of Power Sources*. **2009**, *194*, 588-600.
- (100). Krausa, M.; Vielstich, W., Study of the Electrocatalytic Influence of Pt/Ru and Ru on the Oxidation of Residues of Small Organic-Molecules. *Journal of Electroanalytical Chemistry*. **1994**, *379*, 307-314.
- (101). Tong, Y. Y.; Kim, H. S.; Babu, P. K.; Waszczuk, P.; Wieckowski, A.; Oldfield, E., An NMR investigation of CO tolerance in a Pt/Ru fuel cell catalyst. *Journal of the American Chemical Society*. **2002**, *124*, 468-473.
- (102). Gasteiger, H. A.; Markovic, N.; Ross, P. N.; Cairns, E. J., Methanol Electrooxidation on Well-Characterized platinum-ruthenium bulk Alloys. *Journal of Physical Chemistry*. **1993**, *97*, 12020-12029.
- (103). Calle-Vallejo, F.; Martinez, J. I.; Garcia-Lastra, J. M.; Sautet, P.; Loffreda, D., Fast Prediction of Adsorption Properties for Platinum Nanocatalysts with Generalized Coordination Numbers. *Angewandte Chemie-International Edition*. **2014**, *53*, 8316-8319.
- (104). Han, B. C.; Miranda, C. R.; Ceder, G., Effect of particle size and surface structure on adsorption of O and OH on platinum nanoparticles: A first-principles study. *Physical Review B*. **2008**, *77*, 075410.
- (105). Toyoda, E.; Jinnouchi, R.; Hatanaka, T.; Morimoto, Y.; Mitsuhashi, K.; Visikovskiy, A.; Kido, Y., The d-Band Structure of Pt Nanoclusters Correlated with the Catalytic Activity for an Oxygen Reduction Reaction. *Journal of Physical Chemistry C*. **2011**, *115*, 21236-21240.
- (106). Gantassi, O.; Menakbi, C.; Derbel, N.; Guesmi, H.; Mineva, T., Density Functional Study of Pd-13 Magnetic Isomers in Gas-Phase and on (100)-TiO₂ Anatase. *Journal of Physical Chemistry C*. **2015**, *119*, 3153-3162.
- (107). Priest, C.; Tang, Q.; Jiang, D. E., Structural Evolution of Tc-n (n=4-20) Clusters from First-Principles Global Minimization. *Journal of Physical Chemistry A*. **2015**, *119*, 8892-8897.
- (108). Xing, X. D.; Hermann, A.; Kuang, X. Y.; Ju, M.; Lu, C.; Jin, Y. Y.; Xia, X. X.; Maroulis, G., Insights into the geometries, electronic and magnetic properties of neutral and charged palladium clusters. *Scientific Reports*. **2016**, *6*, 19656.
- (109). Shi, H. B.; Auerbach, S. M.; Ramasubramaniam, A., First-Principles Predictions of Structure Function Relationships of Graphene-Supported Platinum Nanoclusters. *Journal of Physical Chemistry C*. **2016**, *120*, 11899-11909.

- (110). Friedman, J. H., Stochastic gradient boosting. *Computational Statistics & Data Analysis*. **2002**, 38, 367-378.
- (111). Pedregosa, F.; Varoquaux, G.; Gramfort, A.; Michel, V.; Thirion, B.; Grisel, O.; Blondel, M.; Prettenhofer, P.; Weiss, R.; Dubourg, V.; Vanderplas, J.; Passos, A.; Cournapeau, D.; Brucher, M.; Perrot, M.; Duchesnay, E., Scikit-learn: Machine Learning in Python. *Journal of Machine Learning Research*. **2011**, 12, 2825-2830.
- (112). Le, T.; Epa, V. C.; Burden, F. R.; Winkler, D. A., Quantitative Structure-Property Relationship Modeling of Diverse Materials Properties. *Chemical Reviews*. **2012**, 112, 2889-2919.
- (113). Norskov, J. K.; Bligaard, T.; Rossmeisl, J.; Christensen, C. H., Towards the computational design of solid catalysts. *Nature Chemistry*. **2009**, 1, 37-46.
- (114). Li, Z.; Ma, X. F.; Xin, H. L., Feature engineering of machine-learning chemisorption models for catalyst design. *Catalysis Today*. **2017**, 280, 232-238.
- (115). Ma, X. F.; Li, Z.; Achenie, L. E. K.; Xin, H. L., Machine-Learning-Augmented Chemisorption Model for CO₂ Electroreduction Catalyst Screening. *Journal of Physical Chemistry Letters*. **2015**, 6, 3528-3533.
- (116). Takigawa, I.; Shimizu, K. I.; Tsuda, K.; Takakusagi, S., Machine-learning prediction of the d-band center for metals and bimetals. **2016**, 6, 52587-52595.
- (117). Arslan, H., Structures and energetic of Palladium-Cobalt binary clusters. *International Journal of Modern Physics C*. **2008**, 19, 1243-1255.
- (118). Gould, A. L.; Heard, C. J.; Logsdail, A. J.; Catlow, C. R. A., Segregation effects on the properties of (AuAg)₁₄₇. *Physical Chemistry Chemical Physics*. **2014**, 16, 21049-21061.
- (119). Ouyang, R. H.; Xie, Y.; Jiang, D. E., Global minimization of gold clusters by combining neural network potentials and the basin-hopping method. *Nanoscale*. **2015**, 7, 14817-14821.
- (120). Hamad, S.; Catlow, C. R. A.; Woodley, S. M.; Lago, S.; Mejias, J. A., Structure and stability of small TiO₂ nanoparticles. *Journal of Physical Chemistry B*. **2005**, 109, 15741-15748.
- (121). Lv, J.; Wang, Y. C.; Zhu, L.; Ma, Y. M., Particle-swarm structure prediction on clusters. *Journal of Chemical Physics*. **2012**, 137, 084104.
- (122). Zhang, Y. X.; Yang, Z. X., Tuning the catalytic activity of Ag-Pd alloy cluster for hydrogen dissociation by controlling the Pd ratio. *Computational and Theoretical Chemistry*. **2015**, 1071, 39-45.
- (123). Zhao, J. J.; Xie, R. H., Genetic Algorithms for the Geometry Optimization of Atomic and Molecular Clusters. *Journal of Computational and Theoretical Nanoscience*. **2004**, 1, 117-131.

- (124). Lloyd, L. D.; Johnston, R. L.; Roberts, C.; Mortimer-Jones, T. V., Geometry optimisation of aluminium clusters using a genetic algorithm. *Chemphyschem.* **2002**, *3*, 408-415.
- (125). Johnston, R. L., Evolving better nanoparticles: Genetic algorithms for optimising cluster geometries. *Dalton Transactions.* **2003**, 4193-4207.
- (126). Plimpton, S., Fast Parallel Algorithms for Short-Range Molecular-Dynamics. *Journal of Computational Physics.* **1995**, *117*, 1-19.
- (127). Chuang, F. C.; Liu, B.; Wang, C. Z.; Chan, T. L.; Ho, K. M., Global structural optimization of Si magic clusters on the Si(111) 7 x 7 surface. *Surface Science.* **2005**, *598*, L339-L346.
- (128). Albe, K.; Nordlund, K.; Averback, R. S., Modeling the metal-semiconductor interaction: Analytical bond-order potential for platinum-carbon. *Physical Review B.* **2002**, *65*, 195124.
- (129). Tersoff, J., Empirical Interatomic Potential for Carbon, with Applications to Amorphous Carbon. *Physical Review Letters.* **1988**, *61*, 2879-2882.
- (130). Kresse, G.; Furthmuller, J., Efficiency of ab-initio total energy calculations for metals and semiconductors using a plane-wave basis set. *Computational Materials Science.* **1996**, *6*, 15-50.
- (131). Kresse, G.; Furthmuller, J., Efficient iterative schemes for ab initio total-energy calculations using a plane-wave basis set. *Physical Review B.* **1996**, *54*, 11169-11186.
- (132). Blochl, P. E., Projector Augmented-Wave Method. *Physical Review B.* **1994**, *50*, 17953-17979.
- (133). Kresse, G.; Joubert, D., From ultrasoft pseudopotentials to the projector augmented-wave method. *Physical Review B.* **1999**, *59*, 1758-1775.
- (134). Perdew, J. P.; Burke, K.; Wang, Y., Generalized gradient approximation for the exchange-correlation hole of a many-electron system. *Physical Review B.* **1996**, *54*, 16533-16539.
- (135). Perdew, J. P.; Burke, K.; Ernzerhof, M., Generalized gradient approximation made simple. *Physical Review Letters.* **1996**, *77*, 3865-3868.
- (136). Perdew, J. P.; Yue, W., Accurate and Simple Density Functional for the Electronic Exchange Energy-Generalized Gradient Approximation. *Physical Review B.* **1986**, *33*, 8800-8802.
- (137). Kumar, V.; Kawazoe, Y., Evolution of atomic and electronic structure of Pt clusters: Planar, layered, pyramidal, cage, cubic, and octahedral growth. *Physical Review B.* **2008**, *77*, 205418.
- (138). Longo, R. C.; Gallego, L. J., Structures of 13-atom clusters of fcc transition metals by ab initio and semiempirical calculations. *Physical Review B.* **2006**, *74*, 193409.

- (139). Chang, C. M.; Chou, M. Y., Alternative low-symmetry structure for 13-atom metal clusters. *Physical Review Letters*. **2004**, *93*, 133401.
- (140). Wang, L. L.; Johnson, D. D., Density functional study of structural trends for late-transition-metal 13-atom clusters. *Physical Review B*. **2007**, *75*, 235405.
- (141). Xiao, L.; Wang, L. C., Structures of platinum clusters: Planar or spherical? *Journal of Physical Chemistry A*. **2004**, *108*, 8605-8614.
- (142). Gasper, R. J.; Ramasubramaniam, A., Density Functional Theory Studies of the Methanol Decomposition Reaction on Graphene-Supported Pt-13 Nanoclusters. *Journal of Physical Chemistry C*. **2016**, *120*, 17408-17417.
- (143). Gasper, R.; Shi, H.; Ramasubramaniam, A., Adsorption of CO on Low-Energy, Low-Symmetry Pt Nanoparticles: Energy Decomposition Analysis and Prediction via Machine-Learning Models. *Journal of Physical Chemistry C*. **2017**, *in press*
- (144). Song, W. Y.; Chen, Z. X.; Yang, C.; Yang, Z. P.; Tai, J. P.; Nan, Y. L.; Lu, H. B., Carbon-coated, methanol-tolerant platinum/graphene catalysts for oxygen reduction reaction with excellent long-term performance. *Journal of Materials Chemistry A*. **2015**, *3*, 1049-1057.
- (145). Wen, Z. H.; Liu, J.; Li, J. H., Core/shell Pt/C nanoparticles embedded in mesoporous carbon as a methanol-tolerant cathode catalyst in direct methanol fuel cells. *Advanced Materials*. **2008**, *20*, 743-747.
- (146). Shao, Y. Y.; Wang, J.; Kou, R.; Engelhard, M.; Liu, J.; Wang, Y.; Lin, Y. H., The corrosion of PEM fuel cell catalyst supports and its implications for developing durable catalysts. *Electrochimica Acta*. **2009**, *54*, 3109-3114.
- (147). Yu, X. W.; Ye, S. Y., Recent advances in activity and durability enhancement of Pt/C catalytic cathode in PEMFC - Part II: Degradation mechanism and durability enhancement of carbon supported platinum catalyst. *Journal of Power Sources*. **2007**, *172*, 145-154.
- (148). Park, S.; Ruoff, R. S., Chemical methods for the production of graphenes. *Nature Nanotechnology*. **2009**, *4*, 217-224.
- (149). Yang, J.; Zang, C. L.; Sun, L.; Zhao, N.; Cheng, X. N., Synthesis of graphene/Ag nanocomposite with good dispersibility and electroconductibility via solvothermal method. *Materials Chemistry and Physics*. **2011**, *129*, 270-274.
- (150). Wang, C. M.; Ma, L.; Liao, L. W.; Bai, S.; Long, R.; Zuo, M.; Xiong, Y. J., A unique platinum-graphene hybrid structure for high activity and durability in oxygen reduction reaction. *Scientific Reports*. **2013**, *3*, 2580.
- (151). Zhang, L.; Anderson, R. M.; Crooks, R. M.; Henkelman, G., Correlating Structure and Function of Metal Nanoparticles for Catalysis. *Surface Science*. **2015**, *640*, 65-72.

- (152). Smith, G. V.; Tjandra, S.; Musoiu, M.; Wiltowski, T.; Notheisz, F.; Bartok, M.; Hannus, I.; Ostgard, D.; Malhotra, V., Modified activities and selectivities of silated-oxidized-reduced Pd and Pt catalysts. *Journal of Catalysis*. **1996**, *161*, 441-450.
- (153). Hartke, B., Global cluster geometry optimization by a phenotype algorithm with niches: Location of elusive minima, and low-order scaling with cluster size. *Journal of Computational Chemistry*. **1999**, *20*, 1752-1759.
- (154). Airola, M. B.; Morse, M. D., Rotationally resolved spectroscopy of Pt-2. *Journal of Chemical Physics*. **2002**, *116*, 1313-1317.
- (155). Fabbi, J. C.; Langenberg, J. D.; Costello, Q. D.; Morse, M. D.; Karlsson, L., Dispersed fluorescence spectroscopy of jet-cooled AgAu and Pt-2. *Journal of Chemical Physics*. **2001**, *115*, 7543-7549.
- (156). Wang, X. L.; Tian, D. X., Structures and structural evolution of Pt-n (n=15-24) clusters with combined density functional and genetic algorithm methods. *Computational Materials Science*. **2009**, *46*, 239-244.
- (157). Sebetci, A.; Guvenc, Z. B., Global minima of Al(N), Au(N) and Pt(N), N ≤ 80, clusters described by the Voter-Chen version of embedded-atom potentials. *Modelling and Simulation in Materials Science and Engineering*. **2005**, *13*, 683-698.
- (158). Sebetci, A.; Guvenc, Z. B., Global minima for free Pt-N clusters (N=22-56): a comparison between the searches with a molecular dynamics approach and a basin-hopping algorithm. *European Physical Journal D*. **2004**, *30*, 71-79.
- (159). Sebetci, A.; Guvenc, Z. B., Energetics and structures of small clusters: Pt(N), N=2-21. *Surface Science*. **2003**, *525*, 66-84.
- (160). Tian, W. Q.; Ge, M. F.; Sahu, B. R.; Wang, D. X.; Yamada, T.; Mashiko, S., Geometrical and electronic structure of the Pt-7 cluster: A density functional study. *Journal of Physical Chemistry A*. **2004**, *108*, 3806-3812.
- (161). Pittaway, F.; Paz-Borbon, L. O.; Johnston, R. L.; Arslan, H.; Ferrando, R.; Mottet, C.; Barcaro, G.; Fortunelli, A., Theoretical Studies of Palladium-Gold Nanoclusters: Pd-Au Clusters with up to 50 Atoms. *Journal of Physical Chemistry C*. **2009**, *113*, 9141-9152.
- (162). Borbon-Gonzalez, D. J.; Pacheco-Contreras, R.; Posada-Amarillas, A.; Schon, J. C.; Johnston, R. L.; Montejano-Carrizales, J. M., Structural Insights into 19-Atom Pd/Pt Nanoparticles: A Computational Perspective. *Journal of Physical Chemistry C*. **2009**, *113*, 15904-15908.
- (163). Chen, F. Y.; Johnston, R. L., Structure and spectral characteristics of the nanoalloy Ag₃Au₁₀. *Applied Physics Letters*. **2007**, *90*, 153123.
- (164). Liu, X.; Sui, Y. H.; Duan, T.; Meng, C. G.; Han, Y., CO oxidation catalyzed by Pt-embedded graphene: a first-principles investigation. *Physical Chemistry Chemical Physics*. **2014**, *16*, 23584-23593.

- (165). Li, Y. F.; Zhou, Z.; Yu, G. T.; Chen, W.; Chen, Z. F., CO Catalytic Oxidation on Iron-Embedded Graphene: Computational Quest for Low-Cost Nanocatalysts. *Journal of Physical Chemistry C*. **2010**, *114*, 6250-6254.
- (166). Ramos-Sanchez, G.; Balbuena, P. B., Interactions of platinum clusters with a graphite substrate. *Physical Chemistry Chemical Physics*. **2013**, *15*, 11950-11959.
- (167). Kim, G.; Kawazoe, Y.; Lee, K. R., Controlled Catalytic Properties of Platinum Clusters on Strained Graphene. *Journal of Physical Chemistry Letters*. **2012**, *3*, 1989-1996.
- (168). Bader, R. F. W., A Quantum-Theory of Molecular-Structure and Its Applications. *Chemical Reviews*. **1991**, *91*, 893-928.
- (169). Henkelman, G.; Arnaldsson, A.; Jonsson, H., A fast and robust algorithm for Bader decomposition of charge density. *Computational Materials Science*. **2006**, *36*, 354-360.
- (170). Glendening, E. D.; Landis, C. R.; Weinhold, F., Natural bond orbital methods. *Wiley Interdisciplinary Reviews-Computational Molecular Science*. **2012**, *2*, 1-42.
- (171). Dunnington, B. D.; Schmidt, J. R., Generalization of Natural Bond Orbital Analysis to Periodic Systems: Applications to Solids and Surfaces via Plane-Wave Density Functional Theory. *Journal of Chemical Theory and Computation*. **2012**, *8*, 1902-1911.
- (172). Antolini, E.; Salgado, J. R. C.; Gonzalez, E. R., The stability of Pt-M (M = first row transition metal) alloy catalysts and its effect on the activity in low temperature fuel cells - A literature review and tests on a Pt-Co catalyst. *Journal of Power Sources*. **2006**, *160*, 957-968.
- (173). Davis, J. B. A.; Horswell, S. L.; Johnston, R. L., Global Optimization of 8-10 Atom Palladium-Iridium Nanoalloys at the DFT Level. *Journal of Physical Chemistry A*. **2014**, *118*, 208-214.
- (174). Tekin, A.; Hartke, B., Global geometry optimization of small silicon clusters with empirical potentials and at the DFT level. *Physical Chemistry Chemical Physics*. **2004**, *6*, 503-509.
- (175). Porezag, D.; Pederson, M. R.; Frauenheim, T.; Kohler, T., Structure, Stability, and Vibrational Properties of Polymerized C-60. *Physical Review B*. **1995**, *52*, 14963-14970.
- (176). Porezag, D.; Frauenheim, T.; Kohler, T.; Seifert, G.; Kaschner, R., Construction of Tight-Binding-Like Potentials on the Basis of Density-Functional Theory-Application to Carbon. *Physical Review B*. **1995**, *51*, 12947-12957.
- (177). Koskinen, P.; Makinen, V., Density-functional tight-binding for beginners. *Computational Materials Science*. **2009**, *47*, 237-253.
- (178). Koskinen, P.; Hakkinen, H.; Seifert, G.; Sanna, S.; Frauenheim, T.; Moseler, M., Density-functional based tight-binding study of small gold clusters. *New Journal of Physics*. **2006**, *8*.

- (179). Makinen, V.; Koskinen, P.; Hakkinen, H., Modeling thiolate-protected gold clusters with density-functional tight-binding. *European Physical Journal D*. **2013**, *67*.
- (180). Elstner, M.; Frauenheim, T.; Kaxiras, E.; Seifert, G.; Suhai, S., A self-consistent charge density-functional based tight-binding scheme for large biomolecules. *Physica Status Solidi B*. **2000**, *217*, 357-376.
- (181). Elstner, M.; Porezag, D.; Jungnickel, G.; Elsner, J.; Haugk, M.; Frauenheim, T.; Suhai, S.; Seifert, G., Self-consistent-charge density-functional tight-binding method for simulations of complex materials properties. *Physical Review B*. **1998**, *58*, 7260-7268.
- (182). Aradi, B.; Hourahine, B.; Frauenheim, T., DFTB+, a sparse matrix-based implementation of the DFTB method. *Journal of Physical Chemistry A*. **2007**, *111*, 5678-5684.
- (183). Perdew, J. P.; Wang, Y., Accurate and Simple Analytic Representation of the Electron-Gas Correlation-Energy. *Physical Review B*. **1992**, *45*, 13244-13249.
- (184). Frauenheim, T.; Porezag, D.; Elstner, M.; Jungnickel, G.; Elsner, J.; Haugk, M.; Sieck, A., An ab initio two-center tight-binding approach to simulations of complex materials properties. *Tight-Binding Approach to Computational Materials Science*. **1998**, *491*, 91-104.
- (185). Gasteiger, H. A.; Ross, P. N.; Cairns, E. J., LEIS and AES on Sputtered and Annealed Polycrystalline Pt-Ru Bulk Alloys. *Surface Science*. **1993**, *293*, 67-80.
- (186). Wang, L. L.; Khare, S. V.; Chirita, V.; Johnson, D. D.; Rockett, A. A.; Frenkel, A. I.; Mack, N. H.; Nuzzo, R. G., Origin of bulklike structure and bond length disorder of Pt₃₇ and Pt₆Ru₃₁ clusters on carbon: Comparison of theory and experiment. *Journal of the American Chemical Society*. **2006**, *128*, 131-142.
- (187). Kim, J.; Noh, M. C.; Doh, W. H.; Park, J. Y., Thermal Evolution and Instability of CO-Induced Platinum Clusters on the Pt(557) Surface at Ambient Pressure. *Journal of the American Chemical Society*. **2016**, *138*, 1110-1113.
- (188). Lei, Y.; Zhao, H. Y.; Rivas, R. D.; Lee, S.; Liu, B.; Lu, J. L.; Stach, E.; Winans, R. E.; Chapman, K. W.; Greeley, J. P.; Miller, J. T.; Chupas, P. J.; Elam, J. W., Adsorbate-Induced Structural Changes in 1-3 nm Platinum Nanoparticles. *Journal of the American Chemical Society*. **2014**, *136*, 9320-9326.
- (189). Rasko, J., CO-induced surface structural changes of Pt on oxide-supported Pt catalysts studied by DRIFTS. *Journal of Catalysis*. **2003**, *217*, 478-486.
- (190). Thostrup, P.; Vestergaard, E. K.; An, T.; Laegsgaard, E.; Besenbacher, F., CO-induced restructuring of Pt(110)-(1x2): Bridging the pressure gap with high-pressure scanning tunneling microscopy. *Journal of Chemical Physics*. **2003**, *118*, 3724-3730.